RESEARCH PERFORMANCE FINAL REPORT

DOE – NEUP

Project Title:	Investigation of Thermal Aging Effects on the Evolution of Microstructure and Mechanical Properties of Cast Duplex Stainless Steels
DOE Award Number:	DE-NE0000724
DOE Project Number:	NU-13-MD-UMD-0401-01; 13-4765
Principal Investigator:	Dr. Sreeramamurthy Ankem
Recipient Institution[1]:	University of Maryland, College Park
National Laboratory Collaborator:	Dr. Daniel Perea
Collaborating Institution[2]:	Pacific Northwest National Laboratory
Grant Period:	January 13, 2014 – September 30, 2017
Submission Date:	December 11, 2017

Notes

Work acknowledgement: In addition to the P.I. Dr. S. Ankem and primary collaborator Dr. Daniel Perea, work on this project was performed by research scientist Dr. R. Prakash Kolli[1], post-doctoral researcher Dr. Jia Liu[2], and doctoral candidates Sarah Mburu[1] and Samuel Schwarm[1].

Proprietary Data Statement: Data collected and analyzed in this course of this project should be considered proprietary pending publication in relevant technical journals and proceedings.

Table of Contents

I. Executive Summary

This report details the research activities carried out under DOE-NEUP award number DE-NE0000724 concerning the evolution of structural and mechanical properties during thermal aging of CF–3 and CF–8 cast duplex stainless steels (CDSS). The overall objective of this project was to use state-of-the-art characterization techniques to elucidate trends and phenomena in the mechanical and structural evolution of cast duplex stainless steels (CDSS) during thermal aging. These steels are commonly used as structural materials in commercial light water nuclear power plants, undergoing aging for decades in operation as cooling water pipes, pump casings, valve bodies, etc. During extended exposure to these conditions, CDSS are known to undergo a change in mechanical properties resulting in a loss of ductility, i.e. embrittlement. While it is generally accepted that structural changes within the ferrite phase, such as decomposition into iron (Fe)-rich and chromium (Cr)-rich domains, lead to the bulk embrittlement of the steels, many questions remain as to the mechanisms of embrittlement at multiple length scales. This work is intended to shed insight into the atomic level composition changes, associated kinetic mechanisms, and effects of changing phase structure on micro- and nano-scale deformation that lead to loss of impact toughness and tensile ductility in these steels. In general, this project provides a route to answer some of these major questions using techniques such as 3-dimensional (3-D) atom probe tomography (APT) and real-microstructure finite element method (FEM) modeling, which were not readily available when these steels were originally selected for service in light water reactors.

Mechanical properties evaluated by Charpy V-notch impact testing (CVN), tensile testing, and microhardness and nanohardness measurements were obtained for each condition and compared with the initial baseline properties to view trends in deformation behavior during aging. Concurrent analysis of the microstructure and nanostructure by atom probe tomography (APT) and

transmission electron microscopy (TEM) provide mechanistic insight into the kinetic and mechanical behavior occurring on the nano-scale. The presence and morphology of the ferrite, austenite, and carbide phases have been characterized, and formation of new phases during aging, including spinodal decomposition products (α- and α′-ferrite) and G-phase, have been observed. The mechanical and structural characterization have been used to create accurate FEM models based on the real micro- and nano-structures of the systems. These models provide new insight into the local deformation behavior of these steels and the effects of each individual phase (including ferrite, austenite, carbides, and spinodal decomposition products) on the evolving bulk mechanical behavior of the system.

The project was divided into three major tasks:

1. Initial Microstructure and Mechanical Property Survey and Initiate Heat Treatment;
2. Microstructural Characterization and Mechanical Property Testing During Aging; and
3. Microstructure-based Finite Element Modeling.

Each of these tasks was successfully executed, resulting in reliable data and analysis that add to the overall body of work on the CDSS materials. Baseline properties and aging trends in mechanical data confirm prior observations and add new insights into the mechanical behavior of the steels. Structural characterization on multiple length scales provides new information on phase changes occurring during aging and sheds light on the kinetic processes occurring at the atomic scale. Furthermore, a combination of mechanical testing and microstructural characterization techniques was utilized to design FEM models of local deformation behavior of the ferrite and austenite phases, providing valuable new information regarding the effects of each of the microstructural components on the hardening and embrittlement processes. The data and analysis presented in this report and the publication associated with this project (§V) increase the

understanding of aging and deformation in CF–3 and CF–8 steels. These results provide valuable information that can be utilized to aid in making informed decisions regarding the ongoing use of these steels in commercial nuclear infrastructure.

II. Goals and Accomplishments

The objectives of this research, as originally proposed, were to (1) develop a detailed understanding of relationships between microstructure and mechanical response in the CF–3 and CF–8 stainless steels during thermal aging, (2) investigate the role of the intermetallic G-phase on the kinetics of spinodal decomposition, (3) study the effect of the G-phase and $M_{23}C_6$ carbides on embrittlement mechanisms, and (4) validate the use of 360 °C and 400 °C accelerated aging temperatures to simulate operational aging temperatures during extended service life.

(1) Successful completion of the three tasks outlined in **§I** resulted in thorough characterization of the evolution of mechanical properties corresponding to the evolution of the microstructure and nanostructure of the CDSS. Changes in CVN impact energy, tensile strength, and microhardness are shown to have a strong correspondence with the process of spinodal decomposition of the ferrite. Single-phase nanoindentation testing was implemented and demonstrated that the aging of the ferrite is the primary factor in the bulk property changes. The development of FEM models of the microstructure and nanostructure also provide new insight into the effects of aging on the local stress and strain distributions, and their effects on the deformation of the ferrite phase and bulk steels during different stages of aging.

(2) APT data collection and 3-D atomic reconstructions were carried out to determine the progression of spinodal decomposition and the formation of the nickel-silicide (Ni-Si) G-phase within the ferrite phase near the ferrite/austenite phase interfaces. The results allow for analysis of

the kinetics of spinodal decomposition and G-phase formation, and indicate that the G-phase kinetics are closely related to the development of the decomposed ferrite α- and α′-phases.

(3) Analyses of the APT and TEM results were performed regarding the presence of $M_{23}C_6$ carbides (in CF–8) and the development of G-phase precipitates (at accelerated temperatures up to 17,200 h). Comparison of these results with mechanical data indicates that the effect of the carbides on bulk strength is most pronounced in the unaged condition. Furthermore, thorough analysis indicates that the presence of carbides has a pronounced effect on G-phase formation during aging. The cumulative effects indicate that embrittlement is more significant in CF–3 steels where carbides (and their effect on the ferrite kinetics) are not present.

(4) Significant comparison of the results of both raw data and detailed analysis between the operational and accelerated temperatures was performed. The results suggest that for thermal aging up to two years, the accelerated temperatures can be reliable predictors of microstructural evolution and mechanical embrittlement in these steels, but consideration must be given to both time and temperature factors concerning the possibility of different mechanistic contributions to diffusion. Further investigation is recommended and longer aging studies should be performed to expand on this result.

III. Project Activities

a. Methodology

The methodologies presented in this section represent most accurately the work performed during this project and do not depart from the planned methodology unless otherwise noted. All testing was performed at the University of Maryland, College Park unless otherwise noted.

Two stainless steels, ASTM designated CF–3 and CF–8, were purchased from Monett Metals, Inc. in the as-cast and solution treated (1065 °C, 2 h) condition. The material specimens were machined into blanks on site at the University of Maryland and thermally aged in laboratory benchtop furnaces at intervals of 4300 h (~ 6 months) up to 17,200 h (~ 2 years) at four different temperatures: 280 °C, 320 °C, 360 °C, and 400 °C. The lower two aging temperatures fall within the operation range of these materials when serving as cooling water pipes and other structural components of these CDSS in commercial nuclear power plants. The higher two temperatures are accelerated temperatures, intended to speed the kinetic processes (i.e. diffusion) within the steels while maintaining the same stable phases as expected at operational temperatures (i.e. same thermodynamics). Following aging at each time step, specimens were removed from the laboratory furnaces and machined for tensile testing and Charpy V-notch impact testing (CVN) while additional material was set aside for preparation for various other analysis techniques. Prior to aging, specimens were prepared in the same way to test the baseline properties of the unaged steels.

Mechanical testing of the steels was performed by multiple methods: CVN, quasi-static tensile testing, Vickers microhardness, and instrumented nanoindentation. Reported error for all mechanical tests is twice the standard error of the mean.

CVN Specimen dimensions of $55 \times 10 \times 10$ mm ($2.17 \times 0.39 \times 0.39$ in.) with a 45° v-notch were created and tested at room temperature following the standard ASTM E23-16c and using a Tinius Olsen IT406 test frame.

Tensile testing followed standard ASTM E8-13a for 6.35 mm (0.25 in.) gauge diameter and a 25.4 mm (1.0 in.) gauge length cylindrical specimens. Samples were deformed in uniaxial tension using an Instron® model 8502 test frame and model 8800 controller. A 400 N preload was applied prior to initiation of each strain-rate controlled test. Real-time strain measurements were utilized

to apply a strain-rate control rate of 0.00025 s^{-1} using an Instron® 1-in. gauge extensometer. The strain gauge was removed at the strain limit of the extensometer (50%) and testing was continued to fracture using a crosshead speed control rate of 0.006125 mm s^{-1}.

Microhardness testing encompassing the aggregate effects of each of the constituent phases was performed by standard Vickers microhardness testing (ASTM E92-16). Mounted specimens were polished to 0.3 μm surface finish and indented with an Instron Tukon 2100 microhardness tester with a Vickers probe tip. An indentation load of 500 g was applied for a dwell time of 15 s in accordance with the ASTM E384-11 standard procedures. The average of ten measurements was reported for specimens in each aging condition.

The local elastic modulus and nanohardness of the ferrite and austenite constituent phases at each aging condition were measured by instrumented nanoindentation using a diamond Berkovich tip. Indents were made using a Hysitron 900 Triboindenter. A standard quartz specimen was used to calibrate the elastic modulus measurements, which were calculated by the Oliver-Pharr method and following the standard (ASTM 2547-07). The testing procedure consisted of a 15 s loading time to 4000 μN, 10 s holding time, and 15 s unloading to 0 μN (40 s total load time). Single indents were initiated in 12 different locations in each phase. Locations were selected randomly (within a particular phase) to account for local anisotropy due to crystal orientation.

Microstructural characterization of the steels was performed by optical and electron microscopy, including scanning electron microscopy (SEM) and transmission electron microscopy (TEM). Atomic-level compositional reconstructions that were a primary focus of this work was performed by atom probe tomography (APT). Numerous sample preparation techniques were utilized, including metallography, focused ion beam (FIB) including site-specific liftout, and jet electropolishing.

Scanning electron microscopy (SEM) was performed to examine fracture surfaces of CVN fracture surface and to map elemental compositions by Energy Dispersive Spectroscopy (EDS). SEM was performed on the fracture surfaces of CF–3 and CF–8 steels of selected aging conditions following failure by CVN testing. A Tescan XEIA Plasma FIB/SEM was used to image the fracture surfaces. Fractographs were collected in field mode at 10 kV. EDS mapping was performed using a Hitachi S-3400 Variable Pressure SEM instrument with a Bruker QUANTAX XFLASH 4010 EDS. Elemental maps at select δ–ferrite/γ–austenite interfaces were acquired for 1200 s at 15 kV. Overlapping peaks were de-convoluted using the Bruker software.

Transmission electron microscope (TEM) specimens for unaged CF–3 and CF–8 steels were prepared by mechanical thinning to a thickness of approximately 200 μm before punch-out of 3 mm diameter disks. The thin disks were single-jet electropolished in 10 vol.% perchloric acid ($HClO_4$) solution in acetic acid (CH_3COOH) at 0 °C and 20 V for approximately 10 minutes. The disks were subsequently ion-beam milled at a 10° milling angle, 5 kV, and 3 mA to perforation in a Fischione Model 1010 milling system. Select aged specimens were prepared similarly, except a South Bay mechanical dimpling system was used in place of the electropolishing step, due to the difference in etch rates between the ferrite and austenite phases following aging. The phase structure and interfaces were observed at 200 kV by a JEOL 2100 LaB_6 TEM and a JEOL 2100 field emission gun (FEG) TEM equipped with an Oxford INCA 250 X-ray energy dispersive spectrometer (EDS). The selected area electron diffraction (SAED) technique was used to identify the δ–ferrite, γ–austenite, $M_{23}C_6$ carbide, and G-phases in the foils. Conventional TEM images and SAED patterns were analyzed using Gatan's Digital Micrograph Microscopy Suite software.

Specimens for atom probe tomography (APT) analysis were first fabricated using an FEI Helios Nanolab 600 dual beam FIB/SEM instrument following standard lift-out and sharpening

procedures. Atom probe tomography was performed using a CAMECA Local-Electrode Atom Probe (LEAP®) 4000 instrument at the Environmental Molecular Sciences Laboratory (EMSL) at Pacific Northwest National Laboratory (PNNL). APT data were collected along the ferrite-austenite phase interfaces for each aging condition using a specimen tip base temperature of 40 K, DC voltage pulse ratio of 15%-20%, evaporation rate of 0.015 ions per pulse, and background pressure of 10^{-11} Torr (10^{-8} Pa). Data analysis of the ferrite included analysis of spinodally decomposed α and α' domains to determine the mean wavelength (domain size) and mean amplitude (degree of concentration fluctuation) following procedures developed by Mburu, et al (2017), and the full details of the methodology are presented in those texts [1], [2].

Finite element method (FEM) models were designed in 2-dimensions (2-D) to investigate the micromechanical behavior of the ferrite-austenite structure (for CF–3 and CF–8), ferrite-austenite grain boundaries including carbides (for CF–8), decomposed ferrite containing only α and α', and decomposed ferrite containing α, α′, and G-phase. Each of these models was created using experimental images of the real micro- and nanostructures by optical microscopy, TEM, or APT in order to capture the most accurate effects of applied strain on local deformation behavior in the steels. Likewise, properties obtained by experiment were applied to the model wherever possible to ensure accuracy of input property for these specific CDSS systems. Use of primarily 2-D models is a minor deviation from some planned 3-D methodology, where elimination of an arbitrary model thickness allowed for significantly more complex geometries to be implemented with significantly less computation time.

Elastic moduli of the ferrite and austenite phases were obtained from the nanoindentation tests and yielding behavior was approximated by a combination of bulk tensile data and nanohardness results. However, in cases where the phases are sub-micron in size ($M_{23}C_6$, G-phase, spinodal

domains), the most applicable literature values were obtained and applied. Model geometries were created using Rastervect v.21.5 and AutoCAD (2014) software and subsequently imported into ANSYS Finite Element software v.15-18 (updated yearly) with an academic research license through the University of Maryland. Following geometry import, models were meshed and boundary conditions applied to mimic uniaxial tensile loading, where small strain increments were applied and the resulting stress and strain distributions calculated. Further details are available in **§V** of this report, and in the relevant publications listed in **§IV**.

b. Results and Discussion

i. Mechanical Testing

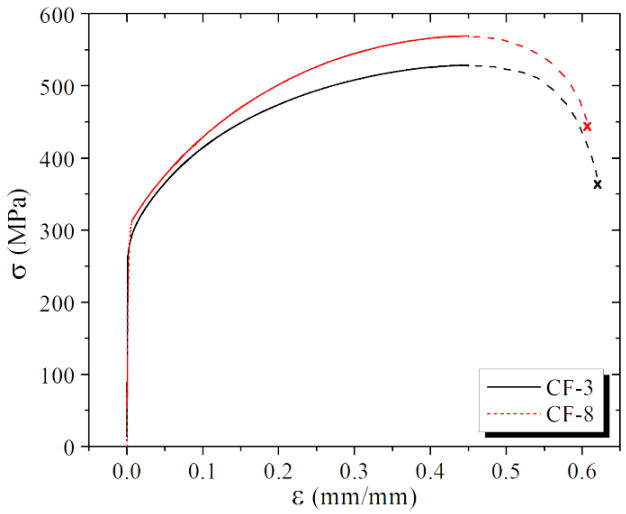

Figure 1. Measured tensile curves for unaged CF–3 and CF–8 specimens [3].

Tensile testing was performed at room temperature (20 °C) on specimens aged at each temperature and time. The baseline tensile curves, Fig. 1, show that the bulk 0.2% offset yield strength (YS) and elastic modulus (E) of the two steels are very similar, while the unaged ultimate tensile strength (UTS) of the CF–8 is higher than that of the CF–3. For the CF–3, the unaged values are measured as YS = 280 MPa, UTS = 530 MPa, and E = 189.1 GPa. For the CF–8, the unaged

values are YS = 286 MPa, UTS = 570 MPa, and E = 169.9 GPa. Results of the testing following aging, Fig. 2, show that the YS of both steels remains approximately constant throughout aging, but that the UTS of both steels increases with time and temperature. This is not uniform, however, and it can clearly be seen that the UTS increases more significantly in the CF–3 steel than in the CF–8 steel. Simultaneously, the ductility (as measured by percent elongation, %el.), decreases in both steels. Similar to the UTS increase, the most significant tensile ductility decrease occurred in

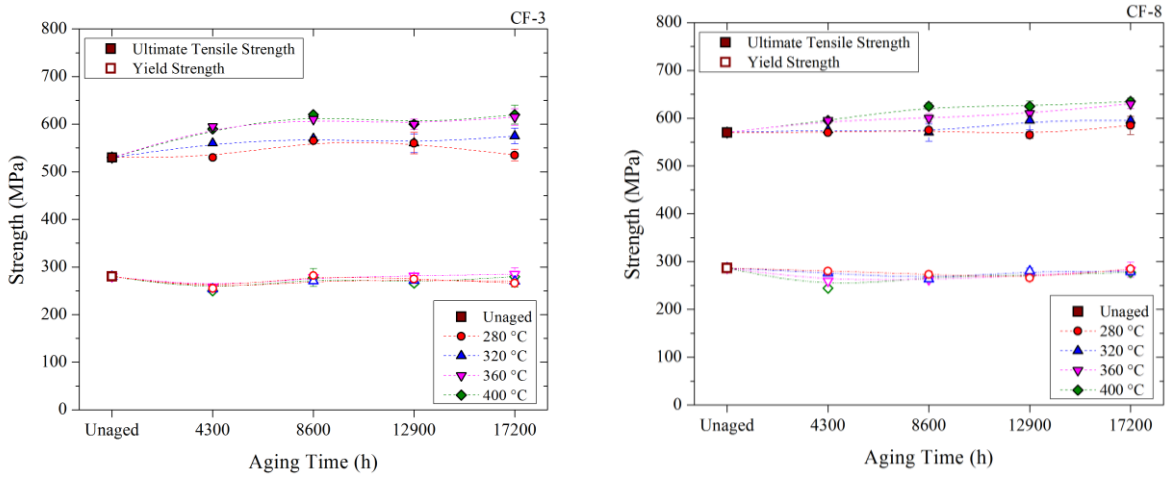

Figure 2. Measured tensile results for YS and UTS for **(a)** CF–3 and **(b)** CF–8 steels aged at different temperatures as a function of aging time [4].

the CF–3 aged at 400 °C for 17,200 h, showing an elongation drop from 61% to 42% (60% to 50% for CF–8 under the same conditions). This constitutes a ~30% reduction in tensile ductility in the CF–3, compared to ~17% in the CF–8 after the same degree of thermal aging.

Tensile testing was also performed at approximately operational temperature (300 °C). At this testing temperature, the unaged specimens show a measured decrease in YS and UTS versus room temperature testing to 174 MPa and 383 MPa, respectively for CF–3, and to 173 MPa and 397 MPa, respectively for CF–8. Similar strength decreases were recorded for all aging conditions.

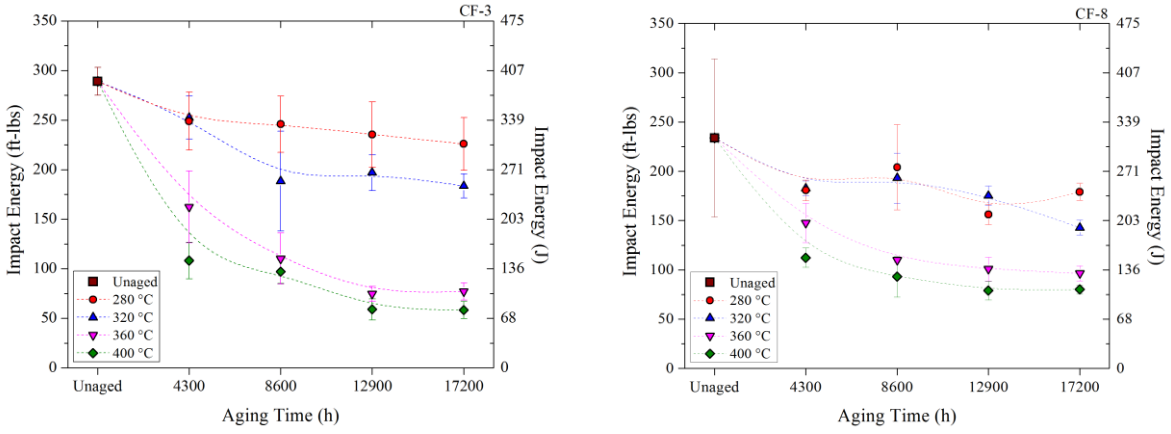

(a) **(b)**

Figure 3. Measured CVN results for **(a)** CF–3 and **(b)** CF–8 steels aged at different temperatures as a function of aging time [4].

Charpy V-notch impact testing was performed at room temperature for all aging conditions in order to characterize embrittlement, Fig. 3. Similarly to the UTS, the unaged specimens show a difference in initial impact energy between CF–3 and CF–8, which have initial mean values of 392 J and 317 J, respectively. However, following the longest aging time (17,200 h) at the highest aging temperature (400 °C), the values drop to 79 J and 109 J, for CF–3 and CF–8, respectively. Again, this shows that the embrittlement of CF–3 occurs faster than in the CF–8. As is discussed later on, this phenomenon is most likely a result of the presence of $M_{23}C_6$ carbides in the CF–8 steel, which alters the composition and kinetics of spinodal decomposition and G-phase formation in the ferrite.

Micro-scale indents created by Vickers microhardness testing are large enough to measure the bulk effects of phase evolution consisting of austenite, ferrite, and carbides. The results indicate that in the unaged condition, the CF–3 has a lower mean Vickers microhardness value of 151.8 $\pm$ 4.6 HV_{500g} then the unaged CF–8, which has a Vickers microhardness value of 165.8 $\pm$ 5.8 HV_{500g}. Similarly to the effects observed by tensile and CVN testing, the difference in properties is most

likely caused by the presence of the $M_{23}C_6$ carbide phase only in the CF–8 steel. Additionally, since C is established to cause interstitial solid-solution hardening, the higher nominal C concentration in the CF–8 steel would also contribute to the higher hardness. The mean Vickers microhardness increases in both steels after aging. Furthermore and again similar to the UTS data, the Vickers microhardness values of the two steels after aging are comparable at all four temperatures – hence, the CF–3 is hardening at a different rate than the CF–8 steel. The microhardness values are also dependent on both time and temperature, showing greater hardening after aging at accelerated temperatures.

Nanoindentation testing was performed to measure the properties in the local ferrite and austenite phases evolving concurrently with the general embrittlement of the bulk steels. Single indents were made to determine the elastic modulus and nanohardness values in each phase at each aging condition. Results prior to aging show that the elastic modulus, *E*, of the ferrite is larger than

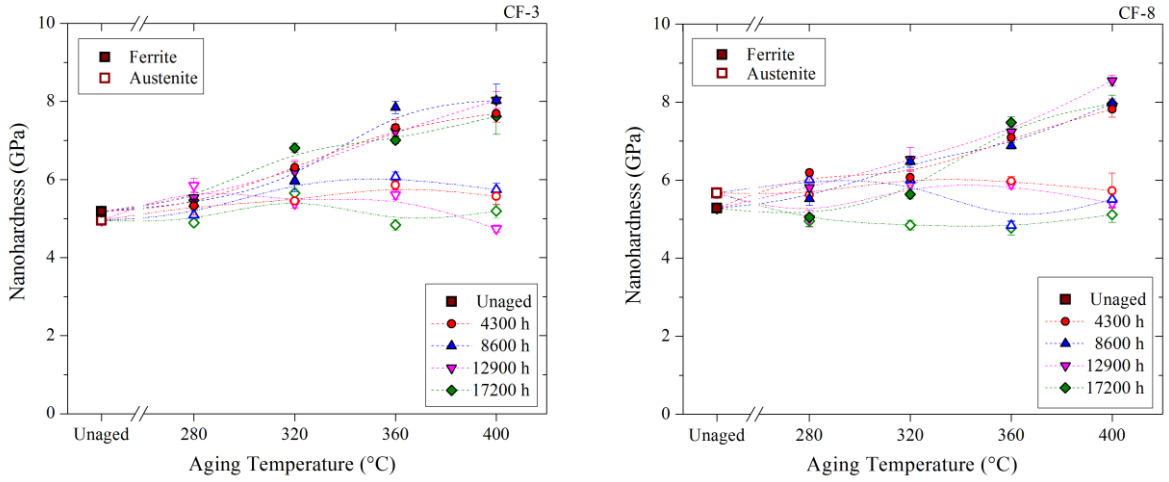

(a) **(b)**

Figure 4. Measured nanoindentation hardness results for the individual ferrite and austenite phases of **(a)** CF–3 and **(b)** CF–8 steels aged at different times as a function of aging temperature [4].

that of the austenite in both steels. The measured values of the unaged *E* are 222 GPa and 204 GPa for ferrite and austenite, respectively, in CF–3. The corresponding mean *E* values for CF–8 are measured as 226 GPa and 211 GPa. These values are consistent with previously reported results [3] and the values for each phase show little change after aging at either operational or accelerated temperatures up to 17,200 h.

Nanohardness values, *H*, for the ferrite and austenite phases are very similar in the unaged condition: 5.18 GPa and 4.95 GPa, respectively, for CF–3; and 5.28 GPa and 5.67 GPa, respectively, for CF–8. Similar to the elastic modulus, the nanohardness of the austenite remains approximately constant during aging. However, the ferrite hardness, Fig. 4, significantly increases during aging at accelerated temperatures, again showing a dependence on aging temperature and aging time. In the CDSS aged at 400 °C, the measured ferrite nanohardness is greater than 8 GPa, an increase of ~60%. At 280 °C, the ferrite nanohardness shows little change up to 17,200 h, similar to the much smaller change in UTS and CVN values at this lower operational temperature. These ferrite trends are consistent with the trends observed by APT for spinodal decomposition, as reported below.

*More detailed analysis and discussion of the evolution of the mechanical properties due to thermal aging can be found in publications resulting from this project grant [1], [3]–[5].

ii. Structural and Compositional Characterization

Initial microstructural characterization was performed by metallographic preparation of the unaged specimens and optical microscopy. The microstructures of the CF–3 and CF–8 steels were confirmed to consist of ferrite within an austenite matrix, Fig. 5. The ferrite volume percentages were calculated by a manual point counting method (ASTM E562-11) and by a computational pixel counting method (ASTM E1245-03). The two methods were found to be in good agreement,

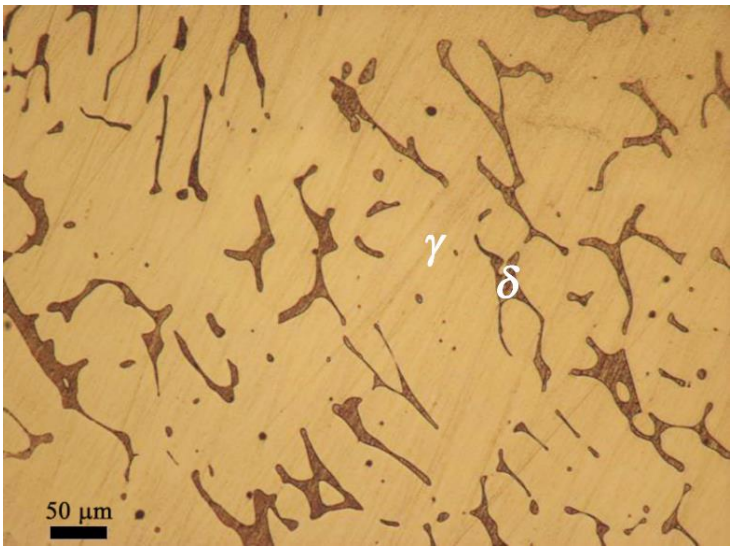

Figure 5. Optical micrograph of unaged duplex microstructure of CF–3 [3].

giving values of 11.5±1.1 vol.% and 12.1±1.0 vol.%, respectively for CF–3, and 9.1±0.9 vol.% and 10.0±0.4 vol.%, respectively for CF–8. At higher volume percentages the ferrite is expected to be more continuously networked within the matrix, which is qualitatively observed in comparison where the volume percentage of CF–3 is known to be higher than that of CF–8. Investigation of the volume percentages following aging shows no significant change in the volume percentage of ferrite at any of the temperatures up to 17,200 h.

SEM-EDS elemental maps were collected from a ferrite-austenite phase interface in the unaged CF–3 stainless steel, Fig. 6 (a)-(c). These images, which show relative elemental concentrations in higher brightness, show that there is significant partitioning of elements between the b.c.c.-ferrite and f.c.c. austenite phases. Most notably, Cr (magenta) is enriched in the ferrite phase and Ni (green) is enriched in the austenite phase. This supports the known effects of Cr as a b.c.c. ferrite stabilizer and Ni as an austenite stabilizer (ASTM A800-14). Corresponding SEM-EDS spectra were analyzed to measure the relative segregation of the alloying elements into the duplex phases. The partitioning ratio is defined by $\kappa_j^{\delta/\gamma} = C_j^{\delta}/C_j^{\gamma}$, where *C* is the elemental

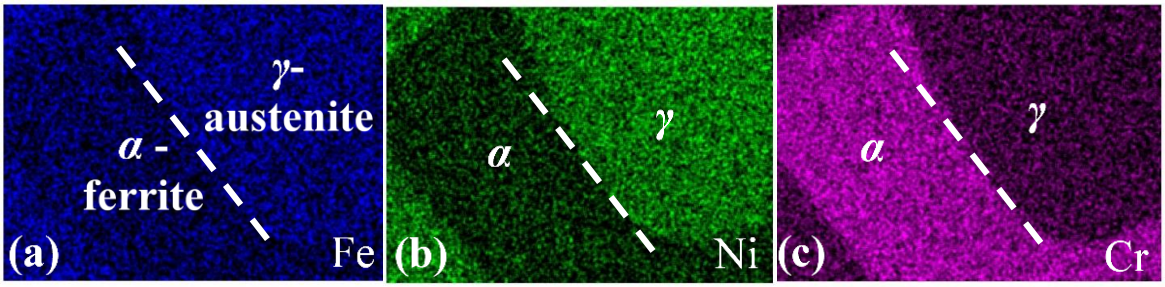

Figure 6. SEM-EDS images showing elemental segregation of (a) Fe, (b) Ni, and (c) Cr in unaged CF–3 steel.

concentration (at.%), j is the element being measured, and the superscript represents the phase. Measured partitioning ratios are 0.97 for Fe, 1.25 for Cr, and 0.57 for Ni in CF–3 and 0.93 for Fe, 1.19 for Cr, and 0.38 for Ni in the CF–8 steel [6].

The unaged CF–3 and CF–8 specimens prepared by electropolishing and ion milling were observed by conventional TEM imaging and selected area electron diffraction (SAED). Phase boundaries were identified qualitatively and diffraction patterns were recorded at zone axes on each side of the boundary. Due to both phases consisting of a cubic crystal lattice, indexing of the diffraction patterns was necessary to definitively identify each phase as bcc ferrite or fcc austenite. Calculation of the lattice parameters of each phase from multiple diffraction patterns and zone axes results in mean values of $a_{fer} = 0.289\,nm$ and $a_{aus} = 0.372\,nm$. These values match quite closely with the values reported by Redjaimia, et al of $a_{fer} = 0.287\,nm$ and $a_{aus} = 0.354\,nm$ for a duplex stainless steel of similar composition [7]. Detailed analysis of the interiors of each phase reveal no additional lattice diffraction spots within either phase or at the boundaries. Furthermore, conventional and high resolution (HR) imaging of the interior of either duplex phase in the unaged steels reveal no additional contrast or interfaces which could be indicative of

additional tertiary phases of significant volume fraction present in the unaged microstructure aside from the presence of carbides at the phase interfaces in CF–8, as discussed below.

The *δ*–ferrite/*γ*–austenite interfaces in both unaged steels were observed by conventional TEM and SAED. The interfaces of the unaged CF–3 steel were straight and uniform and did not exhibit carbide precipitates as demonstrated by the lack of superlattice reflection spots in the SAED pattern, Fig. 7(a). Carbides were also not observed in the b.c.c. *δ*–ferrite phase or the f.c.c. *γ*–austenite phase at locations away from the interfaces. The lack of carbides in the CF–3

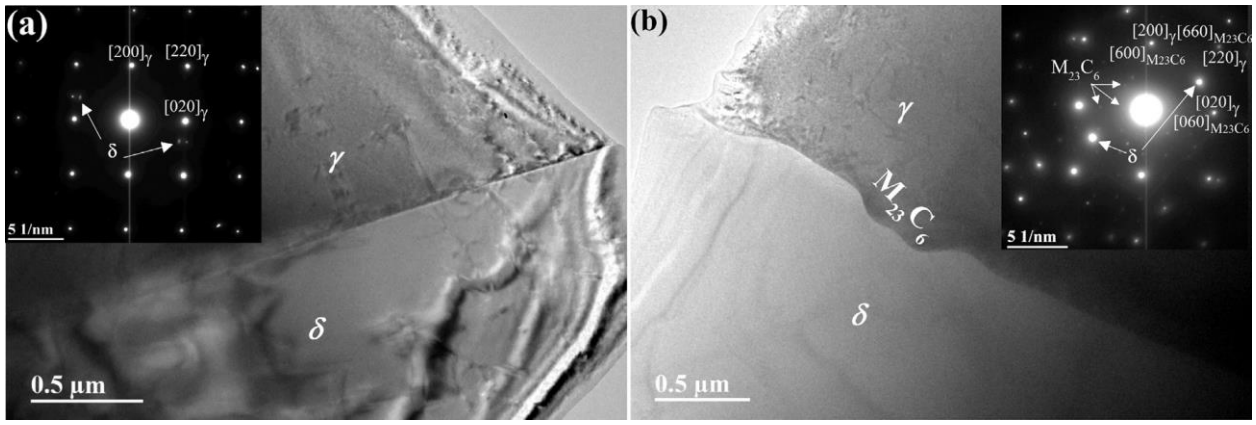

Figure 7. Conventional TEM images of the δ–ferrite/γ–austenite phase boundaries in unaged **(a)** CF–3 and **(b)** CF–8 duplex stainless steels. Insets show SAED patterns along the [001] zone axis of the γ–austenite phase [1].

microstructure is most likely due to the low nominal C concentration of 0.02 at.% (max for the alloy is 0.03 at.%). In contrast, the interfaces in the CF–8 steel demonstrate noticeable deviation from the smooth linearity observed in the CF–3 steel, Fig. 7(b), and SAED patterns taken at the interfaces along the [001] (Fig. 7(b) inset) and $[\bar{3}01]$ *γ*–austenite zone axis [1] reveal the presence of f.c.c. superlattice diffraction spots indicative of an $M_{23}C_6$ carbide phase. These spots not present in the SAED patterns of the interior of either the *δ*–ferrite or *γ*–austenite grains in either steel or along the boundaries in the CF–3 steel. Additionally, the superlattice pattern exhibits a cube–cube orientation relationship (OR) – $\{111\}_\gamma \| \{333\}_{M_{23}C_6}$, $\langle 110\rangle_\gamma \| \langle 330\rangle_{M_{23}C_6}$ – with the *γ*–austenite

phase. Hence, the $M_{23}C_6$ precipitates in the form of elongated carbide particles can be clearly seen at the interface during conventional TEM imaging when the specimen is tilted along a γ-austenite zone axis, but appear primarily as undulations in the phase boundary when observed along a ferrite zone axis.

The lattice parameter, a, of the $M_{23}C_6$ carbides was measured as 1.109 nm in this study, which is slightly greater than the accepted experimental value of $a = 1.065$ nm reported by Southwick and Honeycombe [8], and is similar to other values reported in the literature in the approximate range of $a = 1.05 - 1.10$ nm [9], [10] for an $M_{23}C_6$ carbide, where M = Cr.

Thorough analysis of the CF–3 steel specimens aged at 280 °C, 360 °C, and 400 °C reveal no evidence of carbides present at any boundaries or within either duplex phase. As in the unaged steels, the boundaries are uniformly smoothly linear and show no deviations or undulations indicative of boundary carbides as observed in the CF–8 specimens. Furthermore, SAED at the boundaries of each of the specimens reveal no diffraction spots corresponding to carbides along either austenite or ferrite zone axes.

TEM analysis of the aged CF–8 specimens, again aged at 280 °C, 360 °C, and 400 °C for 17,200 h, as well as aged at 400 °C for 8600 h show the presence of $M_{23}C_6$ carbides in all cases. A representative dark field TEM image with associated diffraction patterns for austenite and the carbide (taken from CF–8 aged at 400 °C for 17,200 h) is presented in Fig. 8, where it can be observed that the OR with the austenite phase is maintained as in the unaged condition. Calculation of the mean lattice parameter of the carbides at the highest aging temperature and longest aging time (400 °C, 17,200 h) results in a value of $a_{M_{23}C_6} = 1.09\ nm$, which is consistent with the value in the unaged CF–8.

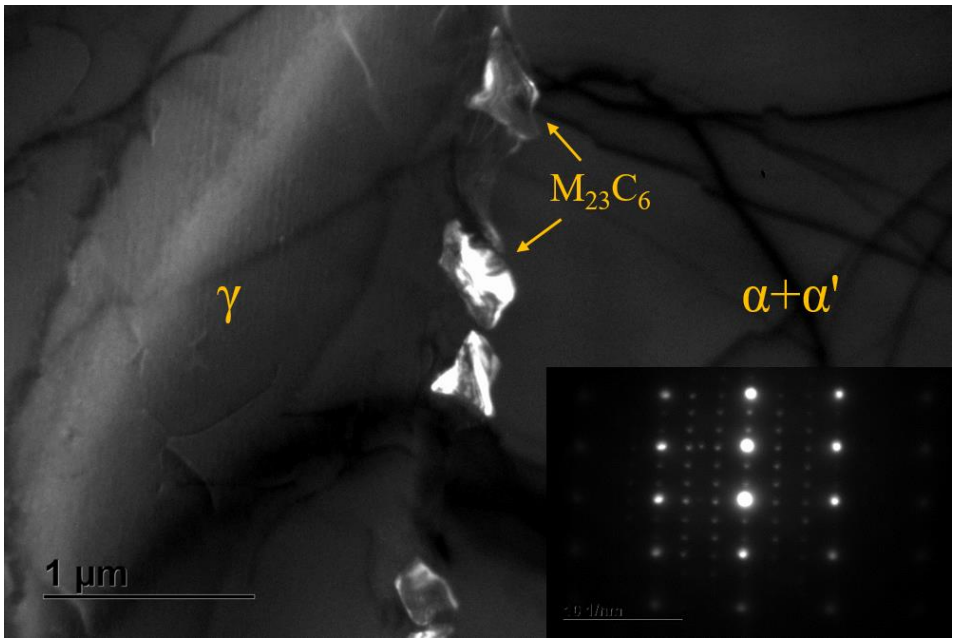

Figure 8. Dark field TEM image of the α/α'–ferrite/γ–austenite phase boundaries in CF–8 DSS aged at 400 °C for 17,200 h. Inset shows SAED patterns of the austenite and carbide phases demonstrating that the cube-on-cube orientation relationship is maintained during aging.

Qualitative analysis suggests that while formation or dissolution of the carbides does not appear to be occurring, there is a noticeable coarsening of the carbides. General quantification of the size and spacing of the carbides during different stages of aging supports this observation. However, due to the small field of view of the TEM and the limited number of boundaries and orientations that have been observed, the quantitative data is not statistically significant enough to draw definite conclusions from. Dark field images, such as those presented in Fig. 8, for different conditions seem to qualitatively confirm the early stages of coalescence of carbides indicative of traditional coarsening, where the volume fraction of the phase remains constant but diffusion of precipitate-forming elements (in this case primarily Cr and C) along the phase boundaries causes the growth of large particles at the expense of smaller, less stable particles. TEM studies present in the literature, notably by Byun, et al. and Hamaoka, et al. [11], [12] for longer aging times support the presence of coarsening mechanisms for the carbides during the aging of DSS.

The decomposition of the ferrite phase leading to bulk embrittlement is characterized by clear chemical segregation of elements on the nano-scale. This is constituted by spinodal decomposition of the ferrite into Fe-rich α and Cr-rich α′ domains ($\delta \rightarrow \alpha + \alpha'$) in both steels under all aging conditions, and by segregation of G-phase forming elements to α/α′ domain boundaries. In the TEM, the decomposition reaction is difficult to observe due to the close similarities in atomic mass and lattice parameter of Fe and Cr, and the resulting small mismatch between the α and α′ domains. Generally, evidence of the spinodal reaction in DSS is said to be indicated by a mottled contrast of slightly lighter and darker regions corresponding to each domain. Generally, mottled contrast was observed in the all aged TEM specimens (aged at 280 °C, 360 °C, and 400 °C for 17,200 h and at 360 °C for 8,600 h). However, due to the lack of structural evidence and the possibility of other phenomena causing mottled texture (i.e. surface roughness, etc.) analysis of α an α' formation was left to the APT presented below.

G-phase formation, however, is a nucleation and growth process of a different crystal structure (f.c.c.) within the ferrite matrix (b.c.c.). However, in the early stages of formation, the nucleation may not yet have occurred, resulting only in contrast between the Ni-Si-Mn-etc. rich G-phase forming zones and the ferrite matrix. Furthermore, even in the case of nucleation, the small size (~5-10 nm radius) and potentially small volume fraction can mean a very small effect on the diffraction patterns and very diffuse lattice spots. Conventional and bright field TEM imaging revealed nano-scale regions of darker contrast corresponding to the distribution and morphology of the G-phase zones determined by APT, Fig. 9. These regions were observed in TEM specimens aged at 360 °C and 400 °C for 17,200 h, and aged at 400 °C for 8,600 h, but were not observed in specimens aged at 280 °C up to the maximum time increment in this study. These results support the following APT results that G-phase formation is only evident at the accelerated

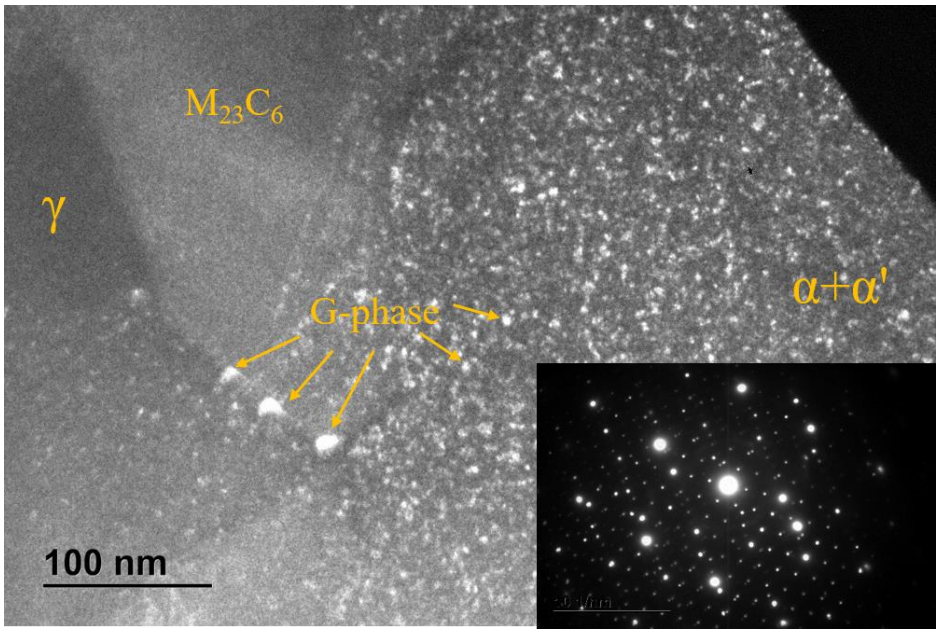

Figure 9. Dark field TEM image of the α/α'–ferrite/γ–austenite phase boundaries in CF–8 duplex stainless steel aged at 400 °C for 17,200 h revealing the complex structure present at a carbide-containing interface after spinodal decomposition and formation of G-phase. Inset shows the SAED patterns of all four phases present, confirming the known orientation relationships.

temperatures following aging up to ~2 years. Furthermore, SAED diffraction spots corresponding to G-phase precipitates were only clearly observed in the CF–8 steel aged at 400 °C for 17,200 h. This confirms the presence of structurally formed G-phase precipitates in this condition. The lack of clearly identifiable diffraction spots in the other accelerated aged specimens could either be explained by the presence of elemental segregation but lack of structural development (i.e. G-phase forming zones) or by a low volume fraction of G-phase in a high thickness TEM sample resulting in too weak of contrast to accurately discern. Furthermore, the CF–8 specimen where the G-phase spots were visible is shown to contain a high density of G-phase and the presence of larger (i.e. >10 nm diameter) G-phase particles at the carbide-ferrite interface. These larger G-phase may be more structurally developed and thus lend greater contrast to the diffraction pattern.

Detailed characterization was performed of the nanostructure by 3-D compositional reconstruction of data collected by atom probe tomography (APT). Data was collected at the ferrite/austenite phase boundaries of samples from each aging condition starting with the unaged. First and most generally, elemental partitioning between the phases was characterized from the APT data using proximity histogram (proxigram) analysis. In general, the elemental partitioning observed by APT matched that observed on a larger scale by EDS, where Cr clearly segregates to the ferrite phase and Ni segregates to the austenite matrix (Fe also is found to be slightly enriched in the austenite). Unlike the EDS, the APT results are able to clearly show elemental segregation to the phase boundaries, which indicates that C and Mo in particular of the alloying elements are isolated at these interfaces.

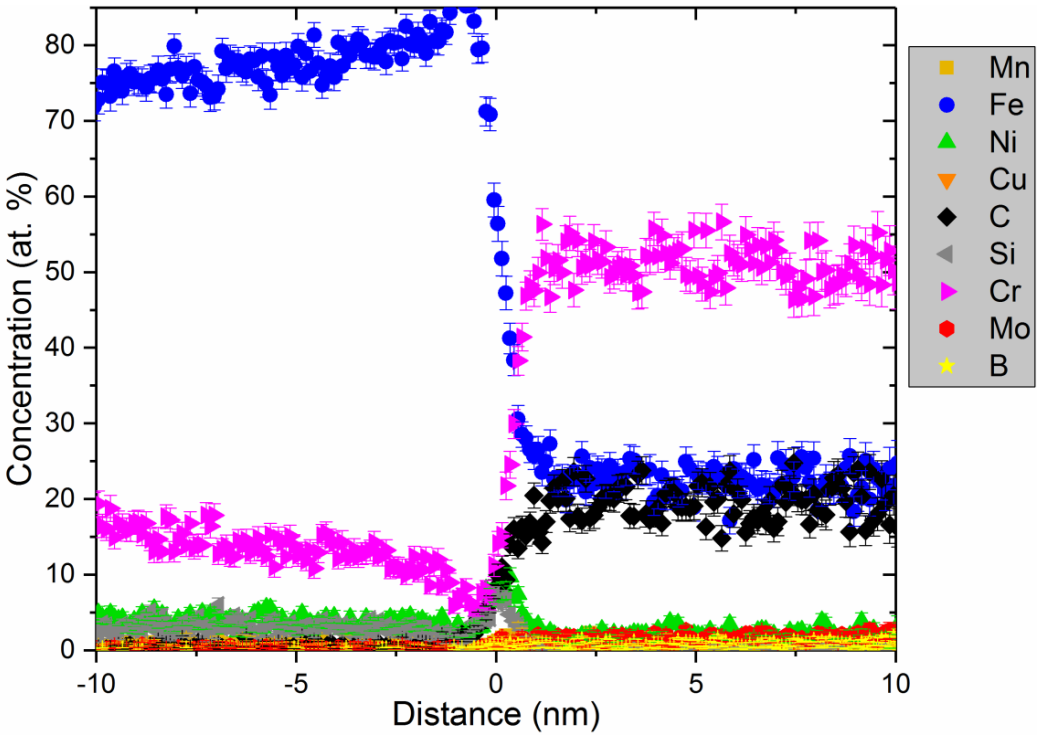

Figure 10. APT proximity histogram of the elemental compositions across a boundary of the decomposed ferrite (left of the 0 point) and an $M_{23}C_6$ carbide (right of the 0 point) showing distinct elemental partitioning between the phases and at the phase boundary.

APT analyses of the interfaces revealed high carbon elemental clusters in many of the CF–8 specimens. These clusters are found consistently throughout the aging treatments only in the CF–8 steel, and are only observed at ferrite/austenite boundaries. Further elemental analysis performed by proximity histograms indicates that these regions are high in C and Cr, and show reduced Fe concentrations, as well as significant reductions in Ni and Si atoms. This is consistent with the presence of chromium carbides. Stoichiometric analysis near the center of the particles indicates a similar composition as would be expected for $M_{23}C_6$ carbides common in DSS. A representative proxigram taken across an interface in a tip aged for 12900 h at 320 °C, Fig. 10, indicates a carbide that is enriched in Cr and B and depleted in Fe, Ni, and Si. This carbide composition is measured at 50.52 at.% Cr, 22.02 at.% Fe, 20.02 at.% C, and less than 2 at.% of any other elements (incl. Ni, Si, Mo, Mn, B, and Cu). The corresponding ferrite composition across the interface is measured as 75.21 at.% Fe, 16.21 at.% Cr, 0.40 at.% C, 0.20 at.% Mo, 4.00 at.% Ni, 0.60 at.% Mn, and 3.00.7 at.% Si. These results demonstrate that the carbide stoichiometry is most stable for Cr and C and that the ferrite is significantly depleted in Cr near the carbide/ferrite interface. Additionally, there is an observed enrichment of Ni and Si in the ferrite near this interface over their mean concentrations in the ferrite. These results confirm the presence of carbides in the CF–8, support previous reports of Cr depletion due to carbide presence, and indicates a new result that the carbides result in an enrichment of important G-phase forming elements (Ni and Si) near this boundary. This latter result will be important in the discussion of G-phase formation in the following paragraphs.

During aging, the most commonly attributed cause of embrittlement is the decomposition of the δ-ferrite phase into Fe-rich α and Cr-rich α' phases. Due to the nanometer scale of these changes, they can be very difficult to characterize by TEM or other methods, but can be captured

readily by atomic reconstruction by APT. In these CDSS, the spinodal decomposition was analyzed in traditional terms of wavelength and amplitude (corresponding to the domain size and compositional fluctuations, respectively) but by a new method to attempt to most accurately describe the evolution of the ferrite system. For specific details regarding this method, please refer to references [1], [2], and [6].

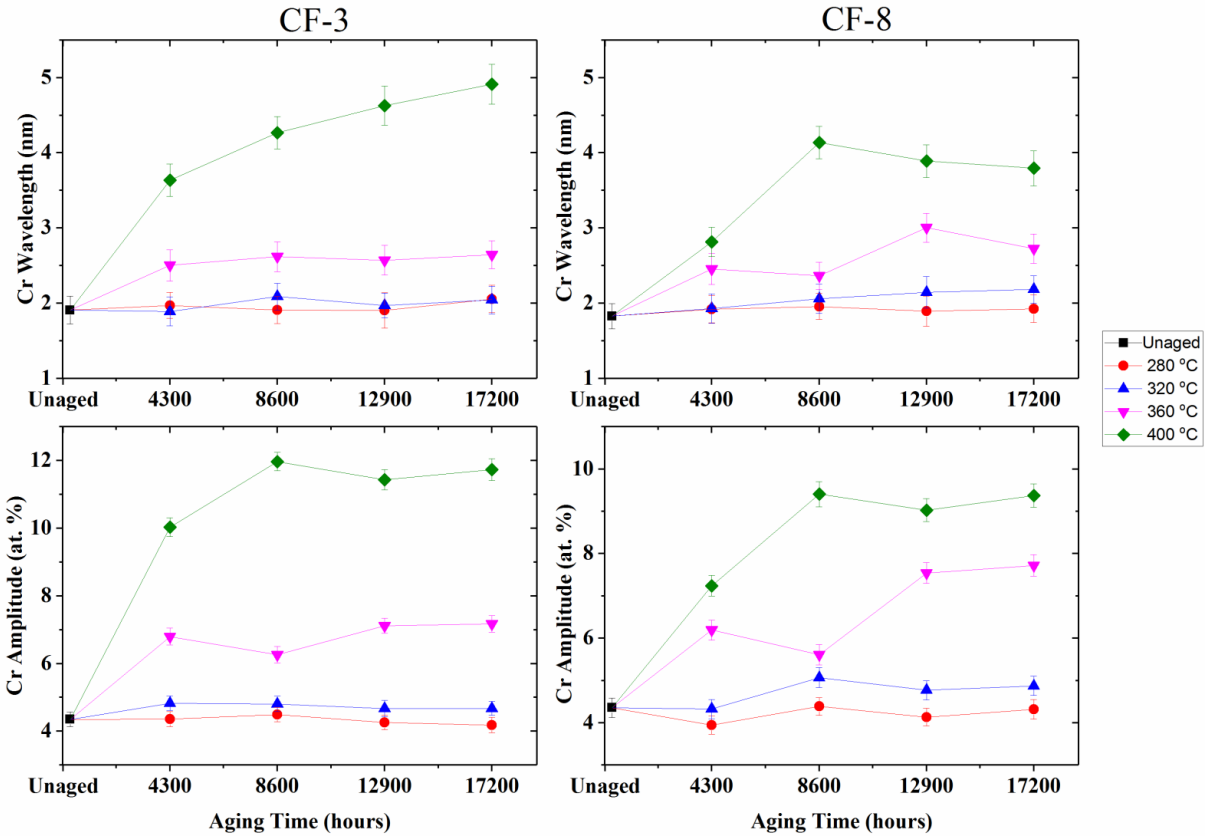

Figure 11. Measured values based on APT data for Cr amplitude and wavelength of the α' domains of the CF–3 and CF–8 steels at each thermal aging step.

Using this method, the wavelength and amplitude were calculated for the α' domains at each aging step, Fig. 11. As can be seen in the figure, the wavelength and amplitude increase with increasing aging temperature and increasing aging time. This effect is most pronounced at the accelerated aging temperatures, where the α' wavelength increases from 1.9 ± 0.2 nm to 4.9 ± 0.3 nm from the unaged state to the 400 °C, 17,200 h aged state (1.8 ± 0.2 nm to 3.8 ± 0.2 nm for CF–

8). Likewise, the amplitude increases from 4.4 ± 0.2 at.% Cr to 11.7 ± 0.3 at.% (4.4 ± 0.2 at..% to 9.4 ± 0.3 at.% for CF–8). However, the operational temperatures, notably at 280 °C, there is little observed change in the spinodal wavelength and amplitude beyond the error. This is likely due to the slow kinetics at these temperatures (since the Fe-Cr miscibility gap is still present at these temperatures) and the very small scale of the decomposition. Thus, for these quantities up to two years, the information obtained by accelerated aging temperatures must serve. Furthermore, the trends observed in spinodal wavelength and amplitude, Fig. 11, are closely mirrored by the trends observed in the local ferrite nanohardness, Fig. 4, thus strongly supporting that the decomposition of the ferrite leads to the property changes (i.e. embrittlement) of the steels. There is also a greater increase in spinodal decomposition in the CF–3 steel than observed for the same time and accelerated temperatures in the CF–8, which correlates to the similarly greater degree of bulk mechanical property changes measured in the CF–3 as compared to CF–8.

The decomposed ferrite was also analyzed for evidence of the formation of the nickel-silicide G-phase. In general, this phase is expected to form as G-phase forming elements segregate to the α/α' domain boundaries within the ferrite during aging. Thus, for the purposes of this experiment, the generic description of G-phase was assigned to any regions containing 6.5 at.% or more Ni within the ferrite (as compared to ~3.5 at.% mean Ni concentration in this phase), as defined in the reconstructions by a 6.5 at.% Ni isoconcentration surface. The results indicate that these particles (which will be referred to here as “G-phase forming zones”, as the APT is not able to distinguish between elemental segregation and nucleated particles) are present following thermal aging only at the accelerated aging temperatures up to 17,200 h of aging. G-phase forming zones were observed at all aging times following aging at 400 °C, and in all specimens aged at 360 °C at 8600 h or more, where the CF–3 aged at 400 °C for 17,200 is presented as example in Fig. 12. In general,

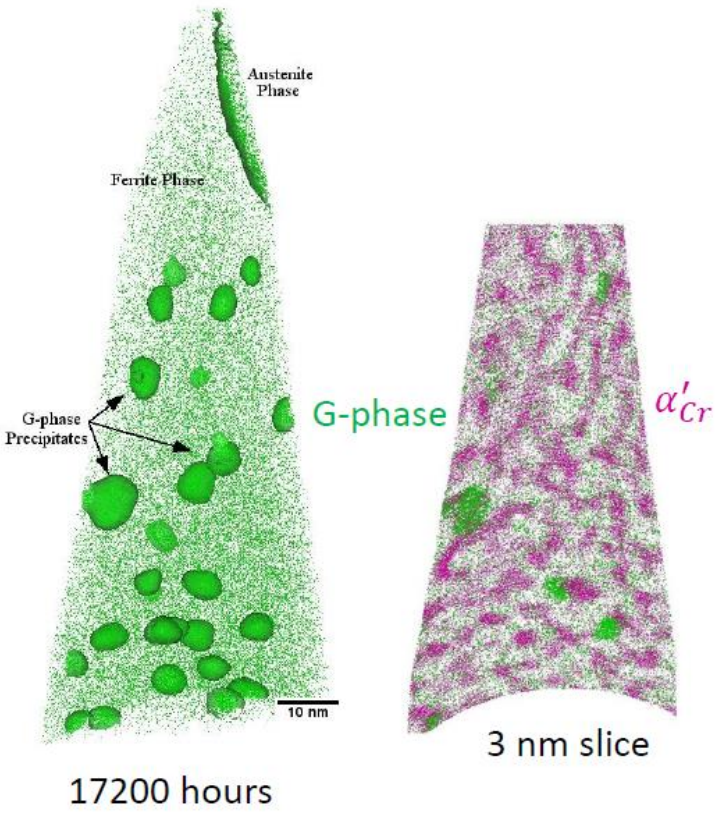

Figure 12. Reconstructions of a 3-D APT tip (left) showing G-phase precipitates as defined by 6.5 at.% Ni isoconcentration surfaces of the CF–3 steel aged at 400 °C for 17,200 h. The image on the right shows a 3 mm thick slice of the same tip highlighting the G-phase (green) locations at the α/α' (white/magenta) domain boundaries within the decomposed ferrite.

the size and number density of the G-phase is dependent on time and temperature, where the size of the particles is observed to be larger in the 400 °C specimens, but the number density is shown to be higher in the 360 °C specimens. The total volume fractions are approaching equality after 17,200 h, and it is possible that the 400 °C specimens are already coarsening by the first aging step of 4300 h and the 360 °C specimens are approaching a more stable, coarsening state by 17,200 h. Furthermore, the presence of the carbides and the associated depletion/enrichment of elements within the ferrite is shown to have an effect on the number density of the G-phase, and analysis indicates that the G-phase has the greatest number density near a carbide interface in CF–8. This is likely due to the enrichment of G-phase forming elements Ni and Si close to the boundary, as

they are unstable in the carbide and would be expelled from the boundary and within the carbide lattice.

In order to characterize the kinetics (i.e. diffusion) within the ferrite phase that leads to nanostructural changes and embrittlement, a new method was devised to incorporate the effects of both increasing domain size (wavelength) and increasing compositional amplitude. This quantity is termed Degree of Decomposition (D.o.D.), and is calculated simply by multiplying the approximate mean volume of the domains (λ^3) by the compositional amplitude (A): D.o.D.= $\lambda^3 \cdot A$. Thus, the movement of atoms corresponding to the increase in domain size and the movement of additional atoms resulting in Fe or Cr enrichment within these growing domains are simultaneously considered. This method allows more accurate determination of quantities related to diffusion during thermal aging. Using this method, time exponents for diffusion were estimated, as were activation energies corresponding to spinodal decomposition and G-phase formation. These methods are undergoing further analysis and the reader is referred to future publications for further detail.

iii. Finite Element Method Modeling

FEM models were created in 2-dimensions based on the real microstructure and nanostructure of the CDSS. Optical microscope images of the ferrite and austenite structure were converted to computational geometries and applied into ANSYS finite element software. Boundary conditions were applied and the effect of elastic loading and yielding behavior were observed under uni-directional tensile loading. Furthermore, models of the boundaries containing carbides were created using TEM images as the geometric basis and models of the nano-scale ferrite, including α and α' domains and G-phase precipitates, were created using APT reconstructions as bases. Each of these different length-scale models was analyzed and stress and strain partitioning were

observed between the phases at each scale. The FEM results show that the hardening of the ferrite phase significantly effects the deformation behavior of the bulk microstructure even in the elastic and near-yield regions. Furthermore, the presence of carbide and G-phase precipitates are shown to affect the deformation behavior at a significant level.

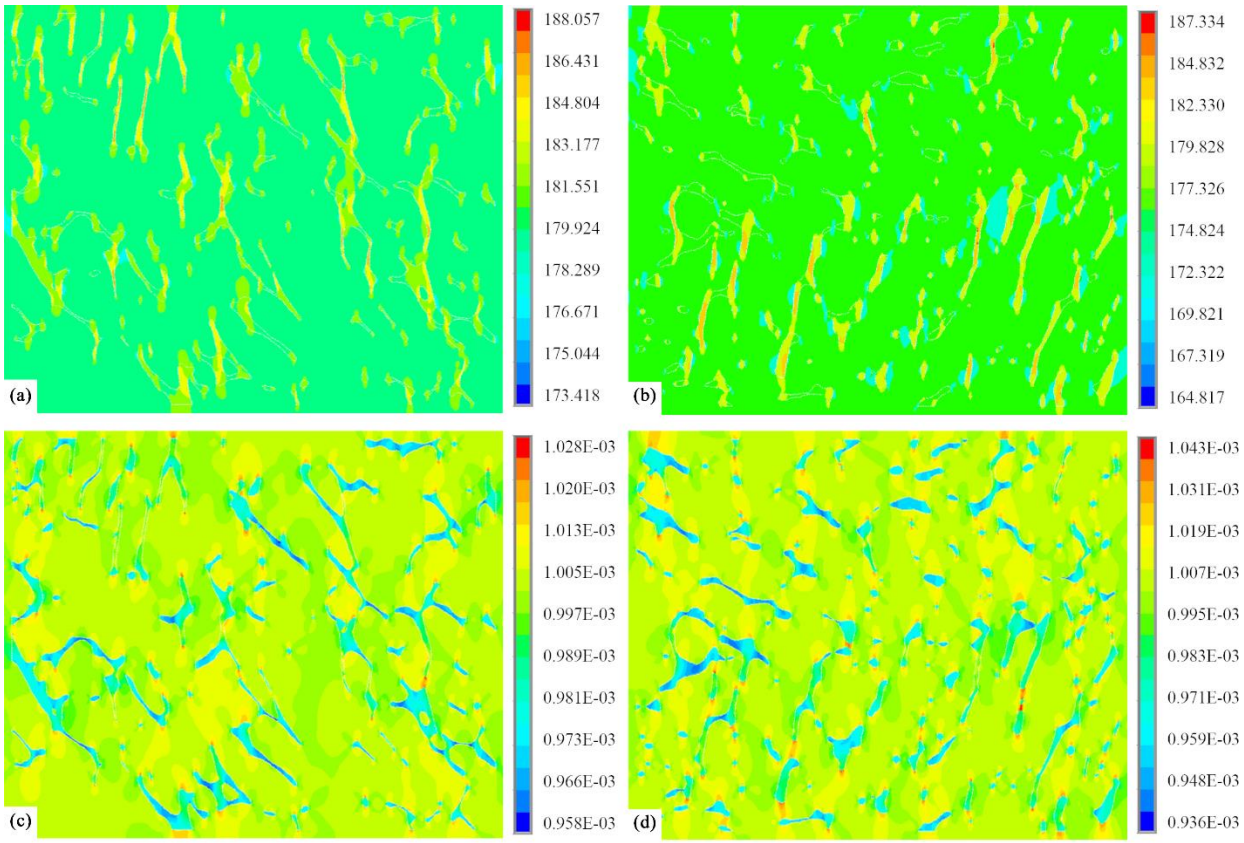

Figure 13. Contour plots of elastic FEM results for **(a)** von Mises stresses in CF–3, **(b)** von Mises stresses in CF–8, **(c)** von Mises strains in CF–3, and **(d)** von Mises strains in CF–8 [3].

The bulk, elastic FEM results for the unaged CF–3 and CF–8 microstructures in Fig. 13 illustrate the effects of an applied, uniaxial tensile displacement on the ferrite and austenite phases. Contour plots of the calculated von Mises stress distributions for the two steels, Fig. 13 (a) – (b), indicate that the δ–ferrite phase undergoes higher stresses than the γ–austenite matrix. The largest stresses occur in the narrowest regions of the ferrite phase which are aligned with the tensile direction, similar to the constant strain assumption of composite behavior [13]. The von Mises

strains, Fig. 13 (c) – (d), exhibit heterogeneity in both steels. In contrast to the stresses, the strains are larger in the austenite matrix than in the ferrite. The maximum stress due to this applied elastic deformation, calculated by FEM, is 188 MPa in the model CF–3 microstructure and 187 MPa in the model CF–8 microstructure. The maximum von Mises strains are calculated as 0.1028 % and 0.1043 % in the CF–3 and CF–8 steels, respectively. The bulk elastic modulus can be calculated from the FEM model results using the stress in the y–direction and the applied strain. These results are 179.3 GPa and 174.1 GPa for CF–3 and CF–8, respectively, which are within 6% of the experimentally measured bulk values measured by tensile testing [3].

Partitioning ratios between the ferrite and austenite phases were determined using the average stresses and strains in each phase in the form $\sigma_\gamma/\sigma_\delta$ and $\varepsilon_\gamma/\varepsilon_\delta$. This allows for direct comparison of the effects of stress and strain transfer between the matrix and the reinforcing phase. The stress (von Mises) partitioning ratios, $\sigma_\gamma/\sigma_\delta$, for CF–3 and CF–8 are 0.984 and 0.978, respectively, confirming that the stresses are transferred from the less stiff austenite matrix to the stiffer ferrite particles. The corresponding strain partitioning ratios, $\varepsilon_\gamma/\varepsilon_\delta$, are 1.022 and 1.038 for CF–3 and CF–8, respectively, and indicate that the strains are transferred to the austenite phase. In addition to the influence of the phase properties, the local stress and strain distributions are influenced by the morphology and distributions of the phases in the steels. Hence, greater stress and strain homogeneity in the matrix phase far from the interfaces is observed in CF–3 than in CF–8. Since little change was observed in the measured elastic moduli of the phases during aging, these results are expected to hold true for elastic deformation at each of the aging conditions. This particular FEM study is presented in greater detail in Schwarm, et al. (2017) [3].

The CF–3 microstructure model discussed in the previous paragraphs was expanded to investigate the yielding (and near-yield) behavior of the steels. Based on similar hardness

measurements, the ferrite and austenite yield strengths are assumed to be equal to each other in the unaged condition and assigned a value equivalent to the bulk proportional limit calculated from tensile testing. Note that for FEM purposes the term "Yield Strength" refers to the proportional limit. As expected due to the results of the elastic deformation models, yielding is found to occur first in the ferrite phase, which reaches the yield stress first as the stresses are transferred from the matrix to the particulate reinforcement phase. However, as aging progresses, the hardness of only the ferrite increases. Due to the common relationship between the hardness and yield strength, it is assumed that the yield strength of the ferrite increases proportionately. Therefore, FEM testing predicts that the phase in which yielding occurs during tensile deformation changes to the austenite phase. This can help explain the lack of change in yield strength with aging observed from bulk tensile testing, as the actual local yield strength is essentially held constant in the microstructure, despite the change in ferrite properties. Further, more detailed analysis is currently being developed for submission for publication.

Additional models were created to investigate the effects of $M_{23}C_6$ carbides at the ferrite-austenite interfaces in CF–8. Two models were created based on TEM images of the interfaces and reduced to a 1 μm x 1 μm square, one representative of the unaged CF–8 microstructure and the other representative of the CF–8 structure following aging (360 °C, 17,200 h). An additional model was created to represent the same ferrite/austenite boundary in the unaged CF–8, but where carbides are not present. Contour plots comparing the results of uniaxial tensile deformation with and without the carbides in the unaged CF–8, Fig. 14 (a) – (b), demonstrate that the minimum stress is much lower in the specimen containing carbides. Though larger maximum stresses are present in the carbide-containing specimen, these high stresses are concentrated within the carbide phase. The results show that near the phase boundary, stress transfer occurs from both the ferrite

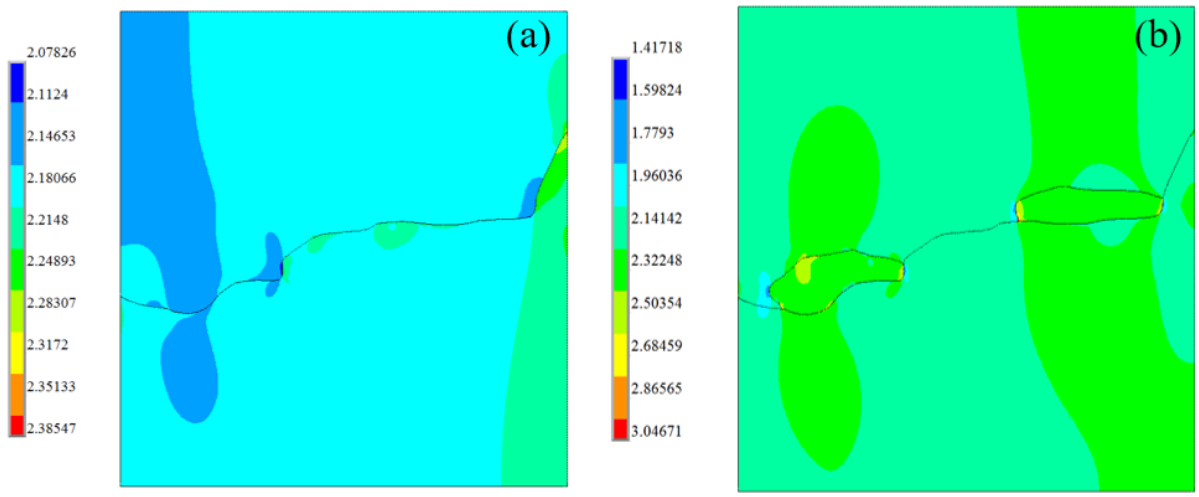

Figure 14. Von Mises stresses during elastic deformation of CF–8 stainless steel along a ferrite/austenite phase boundary **(a)** with no carbides and **(b)** containing carbides.

and austenite phases to the carbide phase, which possesses a higher elastic modulus than either of the duplex phases. Thus, this model shows that on this reduced scale near the duplex phase boundaries of the CF–8 steel, stress and strain partitioning occurs similarly to that observed in the larger scale duplex microstructure, except that the resulting change in stress state in the ferrite and austenite phases are more complex due to the addition of the carbides. Due to the much larger yield strength of the ceramic carbides than the metallic duplex phases, the stress transfer to the carbides is expected to result in an increase in the bulk yield strength near the boundaries. This is possibly borne out by the fact that the yield strength of the CF–8 is found to be slightly higher in the unaged condition than in CF–3, but the values are too similar to state this with a certainty. Additional future studies are recommended taking into account the calculated effects of the boundary results into the larger-scale microstructure models. The present results are currently being prepared in greater detail for future publication.

Finally, models of the ferrite nanostructure were designed to investigate the effects of the formation of α and α' spinodal domains without (Fig. 15(a)) and with (Fig. 15(b)) the presence of G-phase on the local deformation of the ferrite after aging. These model geometries were created

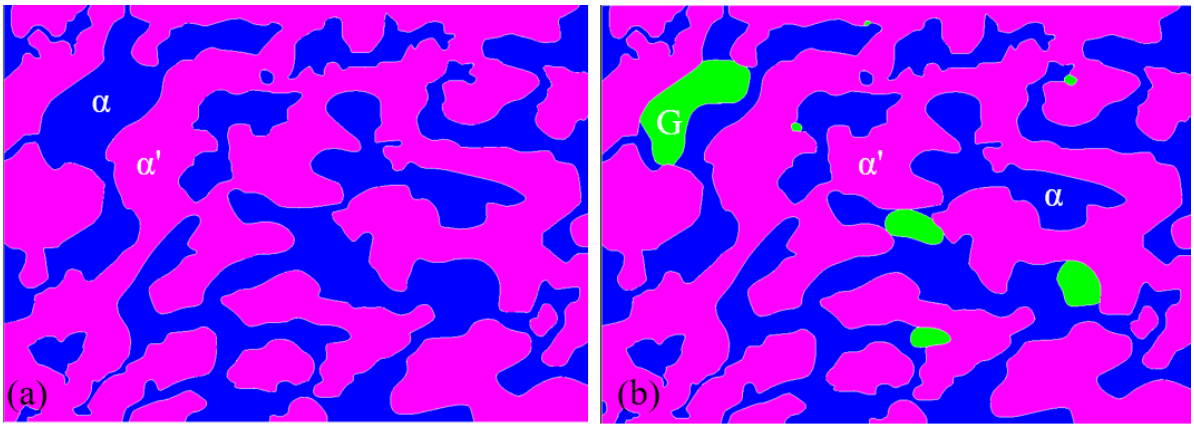

Figure 15. FEM material maps of spinodally decomposed ferrite in CF–3 DSS aged at 400 °C for 17,200 h **(a)** with no G-phase and **(b)** containing G-phase particles. Blue areas correspond to Fe-rich α, magenta areas correspond to Cr-rich α', and green areas correspond to G-phase.

using 2-D slices of APT of the ferrite (~50 nm in size) to recreate the real nanostructure. In general, the interconnected structure of the α and α' domains mimics the duplex microstructure, albeit with the α' having a higher volume fraction in the ferrite than the ferrite takes up of the bulk. Using approximations of the Fe-rich and Cr-rich domain properties obtained using literature sources for the Fe-Cr system, the nanoscale system following aging at 400 °C for 17,200 (in CF–3) is shown to undergo stress and strain portioning very analogous to that of the micro-scale structure. The FEM results suggest that stress is transferred to the Cr-rich α' domains, which likely possess a higher *E*. Furthermore, the addition of G-phase into the nanostructure at the domain boundaries, as observed at the accelerated aging temperatures, can be viewed as analogous to the presence of the carbides at the ferrite-austenite phase boundaries. However, since most reported values for Ni-based intermetallics indicate that the *E* value is very similar to that of the unaged ferrite, the FEM results suggest that there is only a small amount of elastic stress transfer between the decomposed ferrite and the G-phase. Hence, the G-phase may not have a large effect on the yielding properties of the ferrite, and it's primary role in deformation may be to serve as potential initiation sites for

cracking/brittle failure or as Orowan-type obstructions to dislocation motion in the plastic regime. The present results are currently being prepared in greater detail for future publication.

c. Primary Conclusions

The goals and objectives set out by this project were fully completed at the end of the no-cost extension period, September 30, 2017. In general, the most significant results are discussed in this report, and detailed analysis is presented here and/or in peer-reviewed publications (current and future). The principal conclusions determined from this research project are as follows:

(1) The progression of thermal aging embrittlement is dependent on both time and temperature, with specimens aged at the highest temperature (400 °C) for the longest time (17,200 h) exhibiting the largest decrease in CVN energy and tensile ductility. Increases in bulk hardness and UTS are observed concurrently with the decrease in ductility. Furthermore, the CF–3 steel, which is characterized by a lower C composition and does not contain $M_{23}C_6$ carbides, embrittles at a faster rate than the CF–8 steel.

(2) Nanoindentation tests of the individual ferrite and austenite phases demonstrate that significant hardening occurs in the ferrite phase during aging, while the austenite matrix does not undergo significant changes. This supports prior suppositions that the ferrite phase decomposition is the primary driver of bulk property changes during thermal aging of CDSS.

(3) Characterization of the CDSS by SEM and TEM confirm that $M_{23}C_6$ carbides are present in the CF–8, but not in the CF–3, in the unaged (as-solution treated) condition. This is true throughout each of the aging conditions, and no evidence of nucleation or dissolution of carbides is observed at the studied temperatures.

(4) Characterization and 3-D reconstruction of the CDSS by APT reveal that the spinodal decomposition of the ferrite phase into Fe-rich and Cr-rich domains begins prior to the 4300 h

aging step at all studied temperatures. A new method of calculating spinodal wavelength and spinodal amplitude was developed to provide a straightforward and accurate measurement for the progression of phase separation in the ferrite. Results show that the wavelength and amplitude increase with both aging time and aging temperature.

(5) A new method for characterizing the elemental segregation in the ferrite, termed Degree of Decomposition (D.o.D.) was developed in order to better quantify the kinetics of aging. This technique factors in both wavelength and amplitude increase of the spinodal domains in order to capture the total diffusion of the system, and can be applied to additional phases such as the Ni-Silicide G-phase.

(6) Quantification of the progression of formation of G-phase forming zones within the ferrite was performed and revealed that G-phase (as-defined by a 6.5 at.% Ni isoconcentration surface) is present at the accelerated temperatures (360 °C and 400 °C) up to 17,200 h. Significant differences in G-phase formation, such as volume fraction and radius, were observed between the CF–3 and CF–8, especially relative to the locations of the carbides, indicating that the carbides play a significant role in decomposition kinetics, and therefore embrittlement of CDSS.

(7) Finite element method (FEM) models were created based on the real ferritic-austenitic microstructures. The results demonstrate that elastic stress and strain partitioning occurs between the duplex phases during deformation, with stress being transferred to the ferrite particles and strains transferred to the austenite matrix. The greatest stresses are concentrated in narrow ferrite phase regions aligned with the uniaxial loading direction. Furthermore, this behavior is shown to potentially result in a change in local yielding location from the ferrite phase in the unaged steels to the austenite matrix following thermal aging.

(8) FEM studies of the ferrite-austenite phase boundaries containing carbides demonstrate that the presence of the $M_{23}C_6$ phase at the interfaces causes stress transfer from the ferrite and austenite phases.

(9) FEM modeling of the decomposed ferrite structure reveals deformation behavior of the α/α' system to be analogous to the behavior of the duplex system. Progression of spinodal decomposition results in heterogeneity of stress and strain distributions within the ferrite, and stress is transferred to the more stiff α' domains. The effect of the G-phase is likely most evident in the plastic deformation regime of deformation.

IV. Products Developed

a. Peer-Reviewed Journal Articles

1. Samuel C. Schwarm, R. Prakash Kolli, Eda Aydogan, Sarah Mburu, and Sreeramamurthy Ankem. "Characterization of phase properties and deformation in ferritic-austenitic duplex stainless steels by nanoindentation and finite element method". *Materials Science and Engineering: A*, 680, 359-367. 2017. DOI: 10.1016/j.msea.2016.10.116

2. Sarah Mburu, R. Prakash Kolli, Daniel E. Perea, Samuel C. Schwarm, Arielle Eaton, Jia Liu, Shiv Patel, Jonah Bartrand, Sreeramamurthy Ankem. "Effect of aging temperature on phase decomposition and mechanical properties in cast duplex stainless steels., *Materials Science and Engineering: A*, Volume 690, 365-377. 2017. DOI: 10.1016/j.msea.2017.03.011.

3. *(Submitted)* S. C. Schwarm, S. Mburu, R. P. Kolli, D. E. Perea, and S. Ankem, "Effects of Long-Term Thermal Aging on Bulk and Local Mechanical Behavior of Ferritic-Austenitic Duplex Stainless Steels," *Submitted to Materials Science and Engineering A*, 2017.

4. (*Unpublished*) More publication-quality articles with greater depth of discussion than presented in this report are in various stages of development, with intent to submit for publication in the coming months.

b. Conference Proceedings

1. R. Prakash Kolli, Sarah Mburu, Daniel E. Perea, Jia Liu, Samuel C. Schwarm, Arielle Eaton, Sreeramamurthy Ankem. "Characterization of Element Partitioning at the Austenite/Ferrite

Interface of as Cast CF-3 and CF-8 Duplex Stainless Steels." *Proceedings of Microscopy & Microanalysis 2015*, pp. 365-366, August, 2015.

2. Samuel C. Schwarm, Sarah Mburu, R. Prakash Kolli, Daniel E. Perea, Jia Liu and Sreeramamurthy Ankem. "Mechanical and Microstructural Effects of Thermal Aging on Cast Duplex Stainless Steels by Experiment and Finite Element Method". Proceedings of Mechanical and Creep Behavior of Advanced Materials, a SMD Symposium Honoring Professor K. Linga Murty. TMS17, San Diego, CA, 2017.

3. Sarah Mburu, R. Prakash Kolli, Daniel E. Perea, Samuel C. Schwarm, Arielle Eaton, Jia Liu, Shiv Patel, Jonah Bartrand, and Sreeramamurthy Ankem. "Atom Probe Tomography Analysis of the Local Chemical Environment at the Austenite/Ferrite Inter-faces of Cast Duplex Stainless Steels". *Proceedings of LACCEI 2016*, San Jose, Costa Rica, 2016.

c. Conference Presentations (Invited)

1. (Keynote) Sarah Mburu, R. Prakash Kolli, Daniel E. Perea, Samuel C. Schwarm, and Sreeramamurthy Ankem. "Correlating Microstructural Evolution and Embrittlement of Thermally Aged Cast Duplex Stainless Steels". Presented at ICMEST 2016, Tokyo, Japan, October 29-31, 2016.

2. (Invited) S.C. Schwarm, S. Mburu, R.P. Kolli, D.E. Perea, J. Liu, and S. Ankem, "Mechanical and Microstructural Effects of Thermal Aging on Cast Duplex Stainless Steels by Experiment and Finite Element Method", *Mechanical and Creep Behavior of Advanced Materials, a SMD Symposium Honoring Professor K. Linga Murty*, 2017 TMS Annual Meeting, February 26 – March 2, 2017, San Diego, CA.

d. Conference Presentations (Contributed)

1. Sarah Mburu, R. Prakash Kolli, Daniel Perea, and Sreeramamurthy Ankem. "Thermal Degradation of Cast Duplex Stainless Steels", 2015 TMS Annual Meeting, March, 2015, Orlando, FL.

2. R. Prakash Kolli, Sarah Mburu, Daniel E. Perea, Jia Liu, Samuel C. Schwarm, Arielle Eaton, Sreeramamurthy Ankem. "Characterization of Element Partitioning at the Austenite/Ferrite Interface of as Cast CF-3 and CF-8 Duplex Stainless Steels." Microscopy & Microanalysis 2015 Meeting, August, 2015, Portland, OR.

3. Sarah Mburu, R. Prakash Kolli, Samuel Schwarm, Daniel Perea, Jia Liu, Arielle Eaton, and Sreeramamurthy Ankem. "Microstructural Evolution and Embrittlement of Thermally Aged Cast Duplex Stainless Steels". 2016 TMS Annual Meeting, February 14-18, 2016, Nashville, TN.

4. Samuel Schwarm, R. Prakash Kolli, Sarah Mburu, Daniel Perea, and Sreeramamurthy Ankem. "Characterization of Thermal Aging Embrittlement of Cast Duplex Stainless Steels

by Mechanical Testing and FEM Modeling". 2016 TMS Annual Meeting, February 14-18, 2016, Nashville, TN.

5. Sarah Mburu, R. Prakash Kolli, Daniel E. Perea, Samuel C. Schwarm, Arielle Eaton, Jia Liu, Shiv Patel, Jonah Bartrand, and Sreeramamurthy Ankem. "Atom Probe Tomography Analysis of the Local Chemical Environment at the Austenite/Ferrite Inter-faces of Cast Duplex Stainless Steels". LACCEI 2016, July 20-22, 2016, San Jose, Costa Rica.

6. Samuel C. Schwarm, Sarah Mburu, R. Prakash Kolli, Daniel E. Perea, and Sreeramamurthy Ankem. "Effects of Carbide Precipitates and Spinodal Decomposition on Thermal Aging Embrittlement of Cast Duplex Stainless Steels". MS&T 2016, October 23-27 2016, Salt Lake City, UT.

7. S.C. Schwarm, S. Mburu, C. Cady, R.P. Kolli, D.E. Perea, S.A. Maloy, and S. Ankem, "Property Evolution Due to Thermal Aging of Cast Duplex Stainless Steels as Measured by Multi-Scale Mechanical Methods", 2017 TMS Annual Meeting, February 26 – March 2, 2017, San Diego, CA.

V. Modeling Information – Finite Element Method

Finite Element Software: ANSYS v.15.1-18.1

Geometry Software: Rastervect v.21.5, AutoCAD 2014

Element Type: Solid, Plane 186

Mesh Type: 6-node Triangular elements

Geometry Size: *Ferrite/Austenite Models*: 650 µm x 500 µm (~1.6 µm/element edge)
Carbide Models: 1 µm x 1 µm (~3.5 nm/element edge)
Spinodal Models: 50 nm x 38 nm (~0.2 nm/element edge)

Constraints/Boundary Conditions

- Constraints were applied to simulate half of a 2-D tensile specimen containing the geometry microstructure. The bottom row of nodes in each model represents the center-line of a tensile specimen gauge.
- Uniaxial tensile displacement applied in the y-direction to all nodes along the top (y) surface.
- Bottom row of nodes (perpendicular to the y-direction) were constrained to 0 displacement in the y-direction. The centermost bottom node was constrained to 0 displacement in x- and y-directions to prevent specimen motion while allowing for contraction due to Poisson's ratio.
- Geometric interfaces representing phase and domain boundaries are assumed strong.

Material Models

- Elastic testing utilized Elastic-Isotropic property models requiring input elastic moduli and Poisson's ratio.
- Yielding testing utilized the same as the elastic models plus the addition of a Mises plasticity model incorporating bi-linear plasticity. Additional inputs included YS (proportional limit) and tangent modulus corresponding to the slope of linear strain-hardening.
- Input properties were determined experimentally wherever possible. When experimental data was not feasible, assumptions were made and literature values were incorporated. Further details related to specific values are presented in publications related to the project.

VI. References

[1] S. Mburu *et al.*, "Effect of aging temperature on phase decomposition and mechanical properties in cast duplex stainless steels," *Materials Science and Engineering: A*, vol. 690, pp. 365–377, Apr. 2017.

[2] S. Mburu *et al.*, "Atom Probe Tomography Analysis of the Local Chemical Environment at the Austenite/Ferrite Interfaces of Cast Duplex Stainless Steels," presented at the 14 th LACCEI International Multi-Conference for Engineering, Education, and Technology: "Engineering Innovations for Global Sustainability," San Jose, Costa Rica, 2016.

[3] S. C. Schwarm, R. P. Kolli, E. Aydogan, S. Mburu, and S. Ankem, "Characterization of phase properties and deformation in ferritic-austenitic duplex stainless steels by nanoindentation and finite element method," *Materials Science and Engineering: A*, vol. 680, pp. 359–367, Jan. 2017.

[4] S. C. Schwarm, S. Mburu, R. P. Kolli, D. E. Perea, and S. Ankem, "Effects of Long-Term Thermal Aging on Bulk and Local Mechanical Behavior of Ferritic-Austenitic Duplex Stainless Steels," *Submitted to Materials Science and Engineering A*, 2017.

[5] S. C. Schwarm, S. Mburu, R. P. Kolli, D. E. Perea, J. Liu, and S. Ankem, "Mechanical and Microstructural Effects of Thermal Aging on Cast Duplex Stainless Steels by Experiment and Finite Element Method," *Mechanical and Creep Behavior of Advanced Materials*, pp. 253–262, 2017.

[6] S. Mburu, R. P. Kolli, D. E. Perea, J. Liu, S. C. Schwarm, and S. Ankem, "Visualizing and Quantifying Spinodal Decomposition in a Duplex Stainless Steel," *Microscopy and Microanalysis*, vol. 23, no. S1, pp. 660–661, Jul. 2017.

[7] A. Redjaimia, "Decomposition of Delta Ferrite in a Fe-22Cr-5Ni-3Mo-0.03C Duplex Stainless Steel. A Morphological and Structural Study," *Duplex Stainless Steels '91*, pp. 119–126, 1992.

[8] P. D. Southwick and R. W. K. Honeycombe, "Precipitation of M23C6 at austenite/ferrite interfaces in duplex stainless steel," *Metal Science*, vol. 16, no. 10, pp. 475–482, Oct. 1982.

[9] J.-Y. Xie, L.-D. Teng, N.-X. Chen, and S. Seetharaman, "Atomistic simulation on the structural properties and phase stability for Cr23C6 and Mn23C6," *Journal of Alloys and Compounds*, vol. 420, no. 1, pp. 269–272, Aug. 2006.

[10] J. J. Han, C. P. Wang, X. J. Liu, Y. Wang, and Z.-K. Liu, “First-principles calculation of structural, mechanical, magnetic and thermodynamic properties for γ-M 23 C 6 (M = Fe, Cr) compounds,” *J. Phys.: Condens. Matter*, vol. 24, no. 50, p. 505503, 2012.
[11] T. S. Byun, Y. Yang, N. R. Overman, and J. T. Busby, “Thermal Aging Phenomena in Cast Duplex Stainless Steels,” *JOM*, vol. 68, no. 2, pp. 507–516, 2016.
[12] T. Hamaoka, A. Nomoto, K. Nishida, K. Dohi, and N. Soneda, “Effects of aging temperature on G-phase precipitation and ferrite-phase decomposition in duplex stainless steel,” *Philosophical Magazine*, vol. 92, no. 34, pp. 4354–4375, Dec. 2012.
[13] S. Ankem, H. Margolin, C. A. Greene, B. W. Neuberger, and P. G. Oberson, “Mechanical properties of alloys consisting of two ductile phases,” *Progress in Materials Science*, vol. 51, pp. 632–709, 2006.

Appendix A. Published Journal Articles as of December 1, 2017

1. Sarah Mburu, R. Prakash Kolli, Daniel E. Perea, Samuel C. Schwarm, Arielle Eaton, Jia Liu, Shiv Patel, Jonah Bartrand, Sreeramamurthy Ankem. “Effect of aging temperature on phase decomposition and mechanical properties in cast duplex stainless steels., *Materials Science and Engineering: A*, Volume 690, 365-377. 2017. DOI: 10.1016/j.msea.2017.03.011.

2. Samuel C. Schwarm, R. Prakash Kolli, Eda Aydogan, Sarah Mburu, and Sreeramamurthy Ankem. “Characterization of phase properties and deformation in ferritic-austenitic duplex stainless steels by nanoindentation and finite element method”. *Materials Science and Engineering: A*, 680, 359-367. 2017. DOI: 10.1016/j.msea.2016.10.116

See Articles attached below.

Materials Science & Engineering A 690 (2017) 365–377

Contents lists available at ScienceDirect

Materials Science & Engineering A

journal homepage: www.elsevier.com/locate/msea

Effect of aging temperature on phase decomposition and mechanical properties in cast duplex stainless steels

Sarah Mburu[a,*], R. Prakash Kolli[a], Daniel E. Perea[b], Samuel C. Schwarm[a], Arielle Eaton[b], Jia Liu[b], Shiv Patel[a], Jonah Bartrand[b], Sreeramamurthy Ankem[a]

[a] Department of Materials Science & Engineering, University of Maryland, College Park, MD 20742, United States
[b] Environmental Molecular Sciences Laboratory, Pacific Northwest National Laboratory, Richland, WA 99352, United States

ARTICLE INFO

Keywords:
Spinodal decomposition
Duplex stainless steel
Atom probe tomography
$M_{23}C_6$ carbide
G–phase

ABSTRACT

The microstructure and mechanical properties in unaged and thermally aged (at 280 °C, 320 °C, 360 °C, and 400 °C to 4300 h) CF–3 and CF–8 cast duplex stainless steels (CDSS) are investigated. The unaged CF–8 steel has Cr-rich $M_{23}C_6$ carbides located at the δ–ferrite/γ–austenite heterophase interfaces that were not observed in the CF–3 steel and this corresponds to a difference in mechanical properties. Both unaged steels exhibit incipient spinodal decomposition into Fe-rich α–domains and Cr-rich α'–domains. During aging, spinodal decomposition progresses and the mean wavelength (MW) and mean amplitude (MA) of the compositional fluctuations increase as a function of aging temperature. Additionally, G–phase precipitates form between the spinodal decomposition domains in CF–3 at 360 °C and 400 °C and in CF–8 at 400 °C. The microstructural evolution is correlated to changes in mechanical properties.

1. Introduction

Cast duplex stainless steels (CDSS) are used in cooling water pipes, valve bodies, pump casings, and elbows of light water nuclear reactors due to their high strength, ductility, weldability, castability, and excellent resistance to corrosion [1]. The properties of CDSS are due to their dual-phase (duplex) microstructure of body-centered cubic (b.c.c.) δ–ferrite and face-centered cubic (f.c.c.) γ–austenite phases [2,3]. The ferrite phase is present in volume percentages (fractions) that are typically between 9% and 15% in grades used in light water nuclear reactors, such as CF–3 and CF–8 stainless steels [1]. Despite desirable initial properties, these steels experience degradation of mechanical properties associated with thermal aging embrittlement during extended service at operational temperatures between 280 °C and 320 °C. Previous studies have reported that long-term thermal aging at operating temperature causes hardening, loss of impact toughness, and an increase in ultimate tensile strength (UTS) in these steels [1,2,4–15].

The need to extend the service life of light water nuclear reactors to 80 years from an initial design life of 40 years requires an assessment of the extent of thermal aging embrittlement of CDSS. Continuous temporal evolution of the microstructure accompanied by mechanical property degradation may prevent these steels from reaching an 80-year service life. However, performing thermal aging experiments over an 80 year cycle is impractical. An alternative approach is to perform accelerated aging experiments at higher temperatures that are kinetically similar to the operational temperatures (280–320 °C). Many studies have been performed at temperatures greater than 400 °C to accelerate the microstructural aging process and are summarized in Ref. [1]. However, the physical mechanisms leading to embrittlement can vary depending on aging temperature, which can complicate the ability to make relevant comparisons from accelerated aging experiments. For example, while it is generally accepted that phase decomposition does not occur in the f.c.c. γ–austenite phase [12], the embrittlement process is known to involve spinodal decomposition of the b.c.c. δ–ferrite phase [16] at temperatures < 400 °C, where the phase decomposes into Fe-rich α–phase domains and Cr-rich α'–phase domains. Whereas at temperatures > 400 °C, embrittlement is caused by the formation of the brittle σ–phase [1,6,10,16]. However, the validity of using 400 °C as an accelerated aging temperature in CDSS has been questioned due to potentially different phase decomposition kinetics and embrittlement mechanisms when compared to operational aging temperatures [1,5,7,11,17,18]. Besides differences caused by aging temperature, the spinodal decomposition kinetics and amount of mechanical property degradation between steels can differ depending on their composition.

* Correspondence to: Department of Materials Science and Engineering, University of Maryland, 2144 Chemical and Nuclear Engineering Building, #090, College Park, MD 20742-2115, United States.
E-mail address: smburu@umd.edu (S. Mburu).

http://dx.doi.org/10.1016/j.msea.2017.03.011
Received 8 December 2016; Received in revised form 2 March 2017; Accepted 3 March 2017
Available online 06 March 2017

In addition to spinodal decomposition, other phases such as the G–phase and $M_{23}C_6$ carbide can form, which further complicates analysis. The G–phase, an intermetallic nickel silicide, is known to precipitate in the ferrite phase during thermal aging. A few early studies observed G–phase precipitates in CF–8 steel but examined the steel only after aging for many years [5,15,19]. Some recent studies evaluated G–phase precipitate evolution in CF–3M steel, which has high molybdenum (Mo) concentration, at temperatures greater than operational temperatures [12,20,21,22]. Since G–phase precipitation at operational temperatures between 280 °C and 320 °C is not well studied in some CDSS and there exists only limited evaluation of structure-property relationships, further investigation is required. The $M_{23}C_6$ carbide phase has been observed in some CDSS with high carbon (C) concentrations. Although the $M_{23}C_6$ carbide was observed after aging for long time periods at temperatures ≥400 °C [5,7,11], Chung and Leax [11] suggested that the carbide phase may be present in the unaged state of these steels. However there have been no conclusive studies to confirm this and further investigation is required. Additionally, a recent CALculation of PHAse Diagrams (CALPHAD) study indicated that the $M_{23}C_6$ carbide phase is a thermodynamically stable phase at operational temperatures [16]. Currently, the evolution and influence that these intermetallic and carbide phases have on the degradation of mechanical properties is poorly understood, and is thus the focus of the study here. Despite the aforementioned studies, less attention has been paid to the unaged steels and operational temperatures. Furthermore, microstructural evolution and mechanical property degradation differences between CF–3 and CF–8 at operational and accelerated temperatures are not well addressed.

In the investigation described here, we characterize the mechanical properties and microstructure of CF–3 and CF–8 CDSS in both an unaged state and thermally aged for 4300 h at operational temperatures of 280 °C and 320 °C, and accelerated aging temperatures of 360 °C and 400 °C. We characterize and discuss the Cr-rich $M_{23}C_6$ carbide phase that is present in the unaged CF–8 steel by atom probe tomography (APT) and transmission electron microscopy (TEM). In contrast, we did not observe the Cr-rich $M_{23}C_6$ carbide phase in the unaged CF–3 steel. The sub-nanometer spatial resolution and high elemental sensitivity of the APT technique permits three-dimensional (3D) visualization of internal features [23,24], while TEM permits a wider field-of-view (FOV) than APT and acquisition of crystal structure information. We also assess the influence of the local Cr concentration on phase decomposition within the ferrite phase. We evaluate differences in the early stages of spinodal decomposition between the steels using APT. We measure amplitude and wavelength of concentration fluctuations in the ferrite phase that are consistent with the Cahn–Hilliard theory of spinodal decomposition [25,26], and compare it to values of wavelength determined by the auto-correlation function (ACF) method [27] and amplitude determined by the Langer-Bar-on-Miller (LBM) method [28]. In general, we characterize the differences in phase decomposition – including spinodal domains and the G–phase in CF–3 and CF–8 when aging at different temperatures, and relate these results to mechanical property degradation of the two steels.

2. Experimental procedures

2.1. Materials

The steels investigated in this study were obtained from Monett Company, Inc. as 17.8 cm × 3. 3 cm × 2. 9 cm rectangular keel blocks that were cast to the CF–3 and CF–8 standard specification outlined by ASTM A351-12b. All blocks of each steel type were cast from the same melt followed by a solution treatment at 1065 °C (1338 K) for 2 h and quenched in water at room temperature in accordance with the ASTM standard. The nominal chemical composition of the two steels as measured by optical emission spectroscopy (OES) is provided in Table 1. The keel blocks were mechanically reduced into 1. 6 cm × 1. 6 cm × 5. 8 cm Charpy V-notch (CVN) and 1. 6 cm × 1. 6 cm × 8. 9 cm tensile specimen blanks. The blanks were thermally aged in air to 4300 h in four Thermolyne™ Benchtop Muffle Furnaces at temperatures of 280 °C, 320 °C, 360 °C, and 400 °C. Subsequently, the blanks were computer numerical control (CNC) machined into test specimens in accordance with the ASTM standard procedures, as described below.

2.2. Mechanical properties

2.2.1. Charpy V-notch (CVN) impact toughness

The CVN specimens were fabricated in accordance with the ASTM E23-12c standard from the specimen blanks. The 55 mm × 10 mm × 10 mm CVN specimens were tested employing a Tinius Olsen IT406 test frame at room temperature following the ASTM standard test procedures. The absorbed impact energy was measured and fracture morphology was observed for each specimen. The average of two or three measurements was reported for each aging condition, and the reported errors were based on the standard error of the mean.

2.2.2. Vickers microhardness

Specimen blanks were mechanically reduced and cold mounted in epoxy for metallographic specimen preparation. The mounted specimens were ground and polished to 0.3 μm surface finish employing standard procedures. The polished specimens were tested using an Instron Tukon 2100 tester with a Vickers microhardness indenter, a load of 500 g, and dwell time of 15 s in accordance with the ASTM E384-11 standard procedures. The average of ten measurements was reported and the $\pm 2\sigma$ errors were based on the standard error of the mean.

2.2.3. Tensile test

Cylindrical test specimens with a gauge diameter of 6.35 mm and a gauge length of 25.4 mm were fabricated in accordance with the ASTM E8-13a standard. Tensile tests were performed employing an Instron 8502 test frame equipped with an 8800 controller in accordance with the ASTM standard procedure. A preload of ~100 N was applied before the start of each test and a calibrated extensometer with 50% elongation capability was used for continuous measurement of strain using strain-rate control rate of 0.00025 s^{-1}. The extensometer was removed at its elongation limit and the tensile specimens were tested to failure using crosshead speed control rate of 0.006125 mm s^{-1} while measuring load and displacement. The ultimate tensile strength (UTS) was determined following the procedures outlined in the ASTM standard procedure.

2.3. Optical and electron microscopy

Optical microscopy was performed employing a Buehler® ViewMet Inverted Metallograph. The metallographic specimens were etched with Kalling's reagent No. 1 following standard procedures at room temperature to reveal the dual-phase microstructure.

Scanning electron microscope/focused ion beam (SEM/FIB) observations were performed employing a FEI Helios Nanolab 600 dual-beam instrument at 5 keV.

Transmission electron microscope (TEM) specimens for both unaged CF–3 and CF–8 steels were prepared by mechanical thinning to a thickness of approximately 200 μm before punch-out of 3 mm diameter foils. The foils were single-jet electropolished in 10 vol% perchloric acid ($HClO_4$) solution in acetic acid (CH_3COOH) at 0 °C and 20 V for 10 min. The foils were then subsequently ion-beam milled at a 10° milling angle, 5 kV, and 3 mA until perforation in a Fischione Model 1010 milling system. The δ–ferrite/γ–austenite heterophase interfaces were observed by a JEOL 2100 LaB_6 TEM instrument

Table 1
Nominal composition (wt%) of the CF–3 and CF–8 cast duplex stainless steels (CDSS) as measured by optical emission spectroscopy (OES).

Steel		Composition (wt%)						
		Fe	Cr	Ni	Si_{max}	Mn_{max}	Mo_{max}	C_{max}
CF–3	**ASTM A351**	Balance	17.0–21.0	8.0–12.0	2.00	1.50	0.50	0.03
	Unaged	69.52	19.69	8.40	0.98	1.07	0.28	0.02
CF–8	**ASTM A351**	Balance	18.0–21.0	8.0–11.0	2.00	1.50	0.50	0.08
	Unaged	69.44	19.85	8.30	0.97	0.99	0.35	0.06

operated at 200 kV and a JEOL 2100 field emission gun (FEG) TEM instrument operated at 200 kV equipped with an Oxford INCA 250 X-ray energy dispersive spectrometer (EDS). The selected area electron diffraction (SAED) technique was used to identify the δ–ferrite, γ–austenite, and $M_{23}C_6$ carbide phases in the foils. The TEM images and SAED patterns were analyzed using the Gatan Digital Micrograph Microscopy Suite software.

2.4. Atom probe tomography (APT)

2.4.1. Atom probe tomography specimen preparation

Specimens with a needle-shaped geometry necessary for APT analysis were fabricated using a FEI Helios Nanolab 600 dual-beam SEM/FIB instrument following standard lift-out and sharpening procedures [29,30]. The *in situ* site-specific specimen preparation technique was performed on the metallographic mounts to take APT specimen blanks from δ–ferrite/γ–austenite heterophase interfaces, Fig. 1(a)–(b). To create the needle-shaped morphology necessary for APT analysis, annular milling was performed employing a 30 keV gallium ion (Ga^+) beam and sequentially decreasing probe currents following standard procedures after transfer of the region of interest (ROI) to the silicon (Si) microtip post with an Omniprobe micromanipulator, Fig. 1(c)–(e) [31]. As a final step, a low keV ion beam of 2 keV was allowed to raster over the specimen tip to remove material that had been damaged by the 30 keV Ga^+ ion beam annular milling operation [30]. The final apex of the specimen tips, imaged by SEM using 5 keV, had radii of ≤~50 nm suitable for APT analysis.

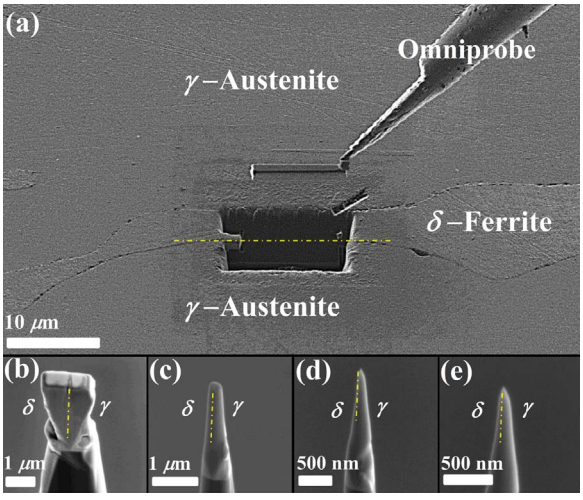

Fig. 1. (a) Site-specific lift-out of an APT specimen tip at an example δ–ferrite/γ–austenite heterophase interface (dashed yellow line) using a SEM/FIB instrument. (b)–(e) series of images illustrating the annular milling of a specimen into a needle morphology with sequentially decreasing tip diameter necessary for APT analysis. (For interpretation of the references to color in this figure legend, the reader is referred to the web version of this article.)

2.4.2. Atom probe tomography data acquisition, reconstruction, and data analysis

A CAMECA Local-Electrode Atom Probe (LEAP®) 4000X instrument in the HR configuration, equipped with a reflectron for high mass resolution, was used for APT analysis. The specimen tip base temperature during data acquisition was set at 40 K. A voltage pulsed mode was applied to the specimen tips with a pulse-to-standing DC voltage ratio of between 15% and 20% at a pulse frequency of 200 kHz to promote field evaporation. The evaporation rate was maintained at a constant 1.5% rate or 0.015 ions per pulse. The background pressure was ~1.6×10^{-11} Torr (2.1×10^{-9} Pa). In order to precisely determine the time-of-flight (TOF) of the ions and thus their mass-to-charge state (m/n) ratios, we confirmed that the aforementioned pulse fraction range resulted in a lower probability of tip fracture, low background noise signal, and low incidences of multiple hits. Data sets of greater than four million ions were collected for each specimen tip, which corresponds to analysis depths of 60–120 nm depending on the tip radius. Data reconstruction and analysis were performed using the CAMECA Integrated Visualization and Analysis Software (IVAS), version 3.6.8. The APT specimen tips were reconstructed with a radius evolution defined using the tip profile morphology from SEM micrographs taken before APT analysis. Overlapping iron (Fe) and chromium (Cr) mass peaks at an m/n ratio of 54 were deconvoluted based on isotopic abundances.

The δ–ferrite/γ–austenite heterophase interfaces were delineated by a 4.5 at% nickel (Ni) isoconcentration surface and associated proximity histogram concentration profiles [32] were used for compositional analysis [33]. The $\pm 2\sigma$ error bars were derived from counting statistics. The δ–ferrite phase and γ–austenite phase compositions were derived from the ion counts using only the plateau points [33] at a far-field distance of between 5 nm and 10 nm from the heterophase interfaces with $\pm 2\sigma \leq 0.25$ at%. An analysis was performed to isolate the $M_{23}C_6$ carbide phase in the CF–8 steel and determine its composition using a 1 nm × 1 nm × 30 nm rectangular ROI and associated one-dimensional (1D) concentration profile. A small cross-section was chosen for the ROI in order to determine the core concentration of the carbide phase.

For spinodal decomposition analysis, a rectangular ROI of dimensions 3.2 nm × 3.2 nm × 30 nm was created in the ferrite phase of each unaged steel. The ROI was positioned at a distance of at least 1 nm away from the heterophase interfaces. The Fe (blue) and Cr (magenta) concentration profiles were determined using a fixed bin width of 0.2 nm. The initial concentration profile data was smoothed using a triangular 3-point moving average defined by $T_i = \frac{1}{4}(t_{i-2}+2t_{i-1}+t_i)$ for bins $i \geq 3$, where t_i is the initial data set and T_i is the smoothed data set. The smoothed profiles were plotted with the mean of the Fe and Cr concentration profiles, which were derived from the ion counts in each bin, Fig. 2(a)–(b). The $\pm 2\sigma$ error bars of the mean Fe and Cr concentrations were derived from counting statistics. The alternating Fe and Cr concentration fluctuations were defined in the same method. A Cr concentration fluctuation was defined as when the concentration was greater than its mean value $+2\sigma$ and concomitantly the Fe concentration fluctuation was less than its mean value. Similarly, the

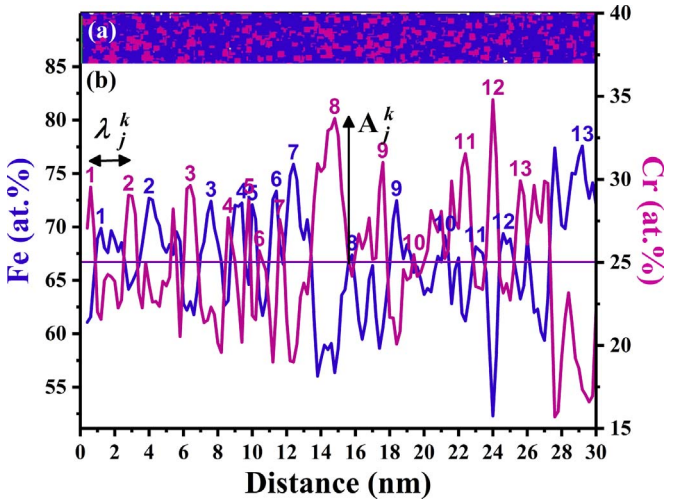

Fig. 2. (a) An example region of interest (ROI) illustrating the compositional heterogeneity of alternating Fe-rich α–domains (blue) and Cr-rich α'–domains (magenta) with (b) corresponding Fe and Cr concentration profiles. The individual fluctuation peaks in the Fe and Cr profiles are numbered and an example wavelength, λ, and amplitude, A, are depicted for the Fe profile. The mean of the Fe and Cr concentrations are superimposed in the plot as solid horizontal lines. (For interpretation of the references to color in this figure legend, the reader is referred to the web version of this article.)

Fe concentration fluctuation was defined as when its concentration was greater than its mean value $+2\sigma$ and concomitantly the Cr concentration fluctuation was less than its mean value. Thus, the periodic alternating fluctuations are defined along the ROI. We consider here that the amplitude of a concentration fluctuation, A, of Fe or Cr was defined as the highest point from the mean concentration value of that element, $A_j^k = C_j^k(max) - \overline{C}_j$, where j is the element and k is the peak number. The wavelength, λ, of Fe or Cr was defined as the distance between two adjacent amplitudes of a concentration fluctuation,$\lambda_j^k = x_j^{k+1} - x_j^k$, where x is the distance along the concentration profile, j is the element, and k is the peak number. The methodology discussed above is consistent with evaluation of wavelength and amplitude for periodic concentration fluctuations, and extant methods evaluate these quantities independently [34]. The above analysis was repeated using 20 non-overlapping rectangular ROIs in order to determine wavelength and amplitude size distributions. The wavelength (in nm) and amplitude (in at%) size distribution histograms were plotted with a bin size of 0.5 for the ferrite phase of both the CF–3 and CF–8 steels. The mean wavelength (MW) and the mean amplitude (MA) were derived from the histograms. Deviation of the ROI cross-sectional dimension within a certain range did not significantly affect the wavelength and amplitude size distributions, thereby indicating a numerically stable evaluation procedure. Binomial distribution functions, which represent the distribution of random wavelengths and amplitudes, were superimposed on the histograms for comparative analysis. The mean wavelength results were compared with those obtained using the ACF method [27] using a bin size of 0.2 nm and the same rectangular ROI's. The mean amplitude results were compared with those determined by the LBM method [28] using a bin (block) size of 100 atoms and the same rectangular ROI's.

The G–phase precipitates in the APT reconstructions were delineated by 6.5 at% Ni isoconcentration surfaces. The precipitate volume equivalent sphere radii, $< R >$ [33], number density, N_V, volume percentage (fraction), V_f, and core compositions are reported. The estimated steel density, ρ, is 8.46×10^{22}atoms cm^{-3}, which was used to

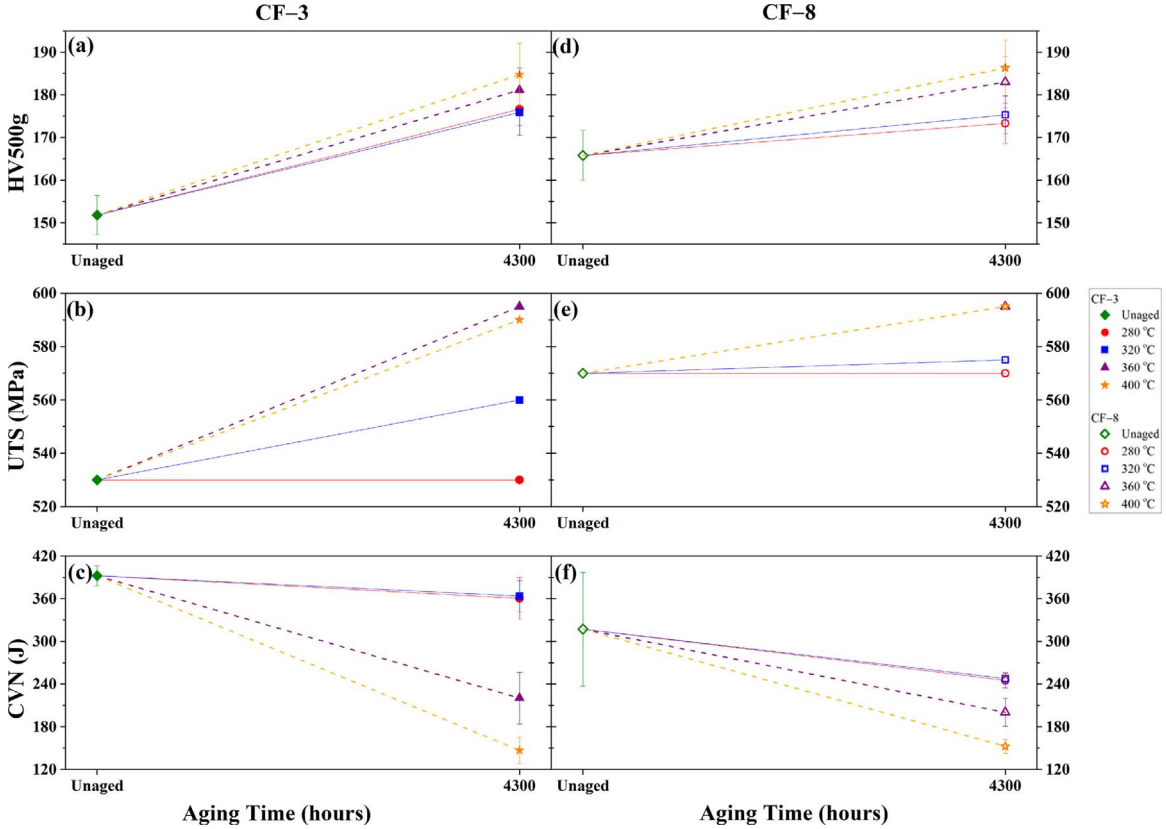

Fig. 3. Mechanical properties as a function aging time at the unaged (green diamonds) and 280 °C (red circles), 320 °C (blue squares), 360 °C (purple triangles), and 400 °C (orange stars) aging temperatures: Vickers Microhardness of (a) CF–3 and (d) CF–8, ultimate tensile strength (UTS) of (b) CF–3 and (e) CF–8, and Charpy V-notch (CVN) impact toughness of (c) CF–3 and (f) CF–8. Solid symbols indicate CF–3 while open symbols indicate CF–8. Trend lines from the unaged data to the aged data are drawn with corresponding colors. The operational temperatures (280 °C and 320 °C) are solid lines, while the accelerated temperatures (360 °C and 400 °C) are dashed lines. (For interpretation of the references to color in this figure legend, the reader is referred to the web version of this article.)

calculate the reconstructed volumes of the APT specimen tips [33] and the estimated detection efficiency, η, is 36% for this atom probe instrument. The G–phase core compositions were derived from the four data points on the right hand side of the proxigram concentration profiles. Deviations of the isoconcentration surface threshold value within a certain concentration range did not significantly change the number of detected precipitates or their proxigrams thereby indicating a numerically stable evaluation procedure.

3. Results and discussion

3.1. Mechanical properties

3.1.1. Vickers microhardness

The results in Fig. 3(a) illustrate that the unaged CF–3 has a lower mean Vickers microhardness value of 151.8 ± 4.6 HV500g, whereas the unaged CF–8 in Fig. 3(d) has a greater mean value of 165.8 ± 5.8 HV500g. As we discuss below, this difference is possibly caused by the presence of the $M_{23}C_6$ carbide phase at the heterophase interfaces in the CF–8 steel but not the CF–3 steel. Additionally, C is well known to cause interstitial solid-solution hardening and the nominal concentration of C in the CF–8 steel is greater than in the CF–3 steel. The mean Vickers microhardness increased for both steels after aging to 4300 h due to phase decomposition, as discussed below. The rates of microhardness increase, as indicated by the slopes of the trend lines in Fig. 3(a) and (d) is approximately twice as great at the accelerated temperatures than at the operational temperatures. The slopes are greater for the CF–3 steel than the CF–8 steel in general indicating that the microhardness increases faster for CF–3. However, after aging, the microhardness values of the two steels are comparable at all four temperatures. The mean microhardness values are greater after aging at accelerated temperatures than operational temperatures for both steels.

3.1.2. Tensile properties

The unaged CF–3 steel has a UTS value of 530 MPa, in Fig. 3(b), and the unaged CF–8 steel has a UTS of 570 MPa, Fig. 3(e). The higher strengths in the CF–8 steel may possibly be due to the presence of the $M_{23}C_6$ carbide phase at the heterophase interfaces. The higher Vickers microhardness and UTS values are consistent with the $M_{23}C_6$ carbide phase acting to strengthen the unaged CF–8 steel when compared to the unaged CF–3 steel. This result is similar to that of Mathew, et al. [35], who reported a UTS of ~600 MPa for a CF–8 steel. Additionally, Michaud, et al. [36] performed tensile property characterization of CF–3 and CF–8 steels and reported a UTS of ~390 MPa for CF–3 steel, while the CF–8 steel exhibited a UTS of ~525 MPa. The trend is consistent with the steels in this study, where CF–8 steel has higher UTS than the CF–3 steel. The mean UTS increased for both steels after aging to 4300 h at the accelerated temperatures and the values were similar between the steels. A difference in behavior was observed when aging at the two operational temperatures. The mean UTS increased for both steels when aging at 320 °C but it only increased for CF–8 and not CF–3 when aging at 280 °C. Furthermore, a difference in mean UTS values still existed between the two steels, unlike when aging at accelerated temperatures. The rates of UTS increase, as indicated by the slopes of the trend lines in Fig. 3(b) and (e) is more than twice as great at the accelerated temperatures than at the operational temperatures. The slopes are greater for the CF–3 steel than the CF–8 steel in general indicating that the UTS increases faster for the CF–3. However, the mean UTS values were greater after aging at accelerated temperatures than operational temperatures.

3.1.3. Charpy V-notch impact toughness (CVN)

As illustrated in Fig. 3(f), the lower CVN impact toughness value of the unaged CF–8 of 317 ± 80 J as compared to the unaged CF–3 of 392 ± 14 J in Fig. 3(c) is most likely due to the presence of $M_{23}C_6$ carbides at the heterophase interfaces. Carbides located at the heterophase interfaces may influence the failure mode by causing phase boundary separation thereby leading to low impact toughness values [13]. Previous research also demonstrated a similar trend where an as-cast CF–3 steel [8] had a higher upper shelf energy of > 300 J when compared to the unaged CF–8 steel [19], which had an upper shelf energy of 225 J. The mean CVN values decreased for both steels after aging to 4300 h at all four temperatures and the mean values were similar between the steels at the accelerated temperatures. At operational temperatures, the CF–8 steel exhibited a greater reduction in mean CVN values when compared to CF–3. Furthermore, a difference in mean CVN values still existed between the two steels unlike when aging at accelerated temperatures. The mean CVN values were lower after aging at accelerated temperatures than operational temperatures and both steels exhibited the lowest CVN value when aging at 400 °C. The unaged specimens exhibited ductile fracture with significant deformation and did not completely break. All aged specimens exhibited more brittle fracture with less deformation and more granular fracture surfaces. The rates of impact toughness decrease, as indicated by the slopes of the trend lines in Fig. 3(c) and (f) is more than twice as great at the accelerated temperatures than at the operational temperatures. The slopes are greater for the CF–3 steel than the CF–8 steel indicating that the impact toughness decreases faster in CF–3.

3.2. Microstructural characterization

3.2.1. Optical microscopy: microstructure

An optical micrograph, Fig. 4, illustrates a microstructure consisting of a network of island-shaped δ–ferrite phase (dark color) in the continuous γ–austenite phase (light color) for the unaged CF–3 steel. The microstructure of the unaged CF–8 steel has a qualitatively similar appearance to that of the CF–3 steel. The ferrite volume percentage is 11.5 ± 1.1% for the CF–3 steel while that of the CF–8 steel is 9.1 ± 0.9% as measured by the manual point counting method specified in the ASTM E562-11 standard [37,38]. The microstructure observed in this study is consistent with that reported in the literature of a steel with a composition similar to CF–8 and with a ferrite volume percentage of less than 20% [39,40]. The ferrite volume percentage remained approximately constant when aging to 4300 h at all four temperatures.

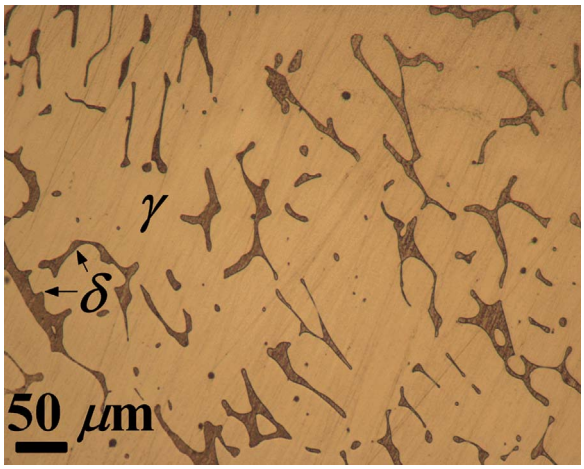

Fig. 4. Optical micrograph of the unaged CF–3 stainless steel microstructure illustrating the γ–austenite phase (light color) and islands of δ–ferrite phase (dark color). (For interpretation of the references to color in this figure legend, the reader is referred to the web version of this article.)

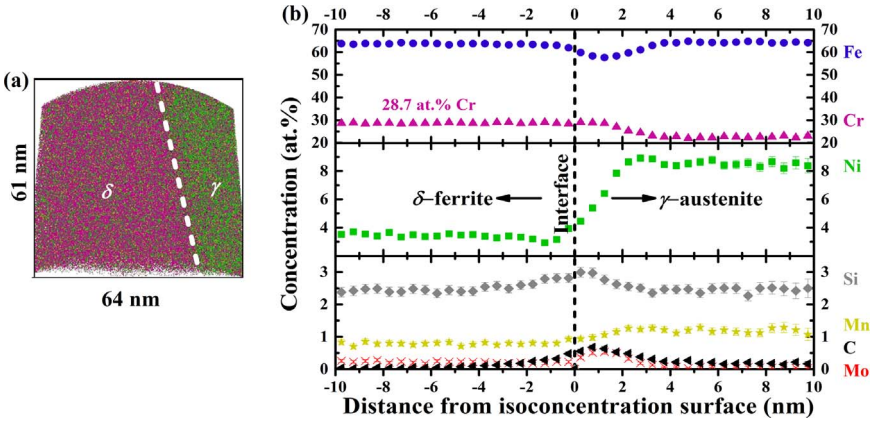

Fig. 5. (a) APT reconstruction of unaged CF–3 with 61 nm × 64 nm dimensions illustrating the δ–ferrite/γ–austenite heterophase interface. 0% of the Fe (blue) ions, 30% of the Cr ions (magenta), and 100% of Ni (green), Mn (mustard), Si (gray), Mo (red), and C (black) are depicted for clarity. (b) Proximity histogram concentration profiles for Fe (blue circles), Ni (green squares), Mn (mustard stars), Cr (magenta triangles), Si (gray diamonds), Mo (red asterisks), and C (black left–triangles) using a 4.5 at% Ni isoconcentration surface. The ± 2σ error bars are based on counting statistics. For the major elements, the error bars are smaller than the marker size. (For interpretation of the references to color in this figure legend, the reader is referred to the web version of this article.)

3.2.2. Atom probe tomography (APT) and transmission electron microscopy (TEM): $M_{23}C_6$ Carbide at the Heterophase Interfaces

The proximity histogram (proxigram) concentration profiles across the δ–ferrite/γ–austenite heterophase interfaces are qualitatively similar for the unaged CF–3 and CF–8 steels, Figs. 5(a)–(b) and 6(a)–(b), respectively. However a distinct carbide phase is observed in the CF–8 reconstruction, Fig. 6(a). The peak C concentration at the heterophase interface is ~0.8 at% for the CF–3 steel and ~1.5 at% for the CF–8 steel, which is influenced by the presence of a carbide phase. As discussed below, this carbide phase is identified as the $M_{23}C_6$ carbide. Since the CF–8 steel has a greater nominal C concentration than the CF–3 steel, the thermodynamic driving force for carbide formation at the heterophase interfaces is greater [16]. A more detailed analysis, Fig. 7(a)–(d), was performed to determine the $M_{23}C_6$ carbide phase composition. The carbides are interspersed along the δ–ferrite/γ–austenite heterophase interface of the APT specimen tip, Fig. 7(a), and an example carbide is visible in the APT reconstructions, Fig. 7(b)–(c). The Cr and C are enriched, while Fe and Ni are depleted within the carbide phase (black box) relative to the austenite phase, Fig. 7(d). The carbide composition is 32.5 ± 2.1 at% Fe, 49.2 ± 1.5 at% Cr, 11.9 ± 1.2 at% C, 2.0 ± 0.4 at% Mo, 2.1 ± 0.7 at% Ni, 1.1 ± 0.2 at% Mn, and 0.65 ± 0.14 at% Si. Recent CALPHAD calculations indicate that the most common carbide present in CF–8 steels is the f.c.c. $M_{23}C_6$ carbide, where M=Cr [16]. Since the steels were cast, solution-treated, and quenched in water at room temperature, the carbide composition in the unaged state is most likely not yet at equilibrium.

The δ–ferrite/γ–austenite heterophase interfaces in both unaged steels were also observed by conventional TEM. The interfaces of the unaged CF–3 steel were consistently straight and uniform and did not exhibit a carbide phase as demonstrated by the lack of superlattice reflection spots in the SAED pattern, Fig. 8(a) inset. Carbides were also not observed in the b.c.c. δ–ferrite phase or the f.c.c. γ–austenite phase grains at locations away from the heterophase interfaces. The lack of carbides in the microstructure is most likely due to the low nominal C concentration, Table 1. In contradistinction, the interfaces in the CF–8 steel were noticeably more undulating than in the CF–3 steel, Fig. 8(b), and SAED patterns taken at the interfaces along the [001], Fig. 8(b) inset, and [$\bar{3}$01], Fig. 9(c), γ–austenite zone axes reveal the presence of f.c.c. superlattice diffraction spots indicative of an $M_{23}C_6$ carbide phase. These spots are not, however, present in the SAED patterns at the interior of either the δ–ferrite phase or γ–austenite phase grains. Additionally, the $M_{23}C_6$ carbide and γ–austenite phase exhibit a cube–cube orientation relationship (OR) of $\{111\}_\gamma \| \{333\}_{M_{23}C_6}$, $\langle 110\rangle_\gamma \| \langle 330\rangle_{M_{23}C_6}$. The $M_{23}C_6$ carbide has an elongated morphology, Fig. 9(a)–(b), with a length of ~230 nm and width of ~90 nm. Other carbides of the same type were observed at multiple different hetero-

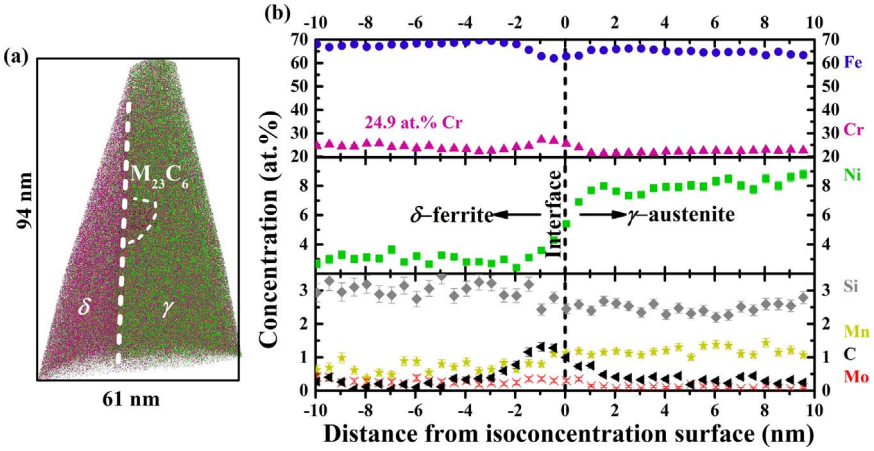

Fig. 6. (a) APT reconstruction of unaged CF–8 with 94 nm × 61 nm dimensions illustrating the δ–ferrite/γ–austenite heterophase interface. 0% of the Fe (blue) ions, 30% of the Cr ions (magenta), and 100% of Ni (green), Mn (mustard), Si (gray), Mo (red), and C (black) are depicted for clarity. (b) Proximity histogram concentration profiles for Fe (blue circles), Ni (green squares), Mn (mustard stars), Cr (magenta triangles), Si (gray diamonds), Mo (red asterisks), and C (black left–triangles) using a 4.5 at% Ni isoconcentration surface. The ± 2σ error bars are based on counting statistics. For the major elements, the error bars are smaller than the marker size. (For interpretation of the references to color in this figure legend, the reader is referred to the web version of this article.)

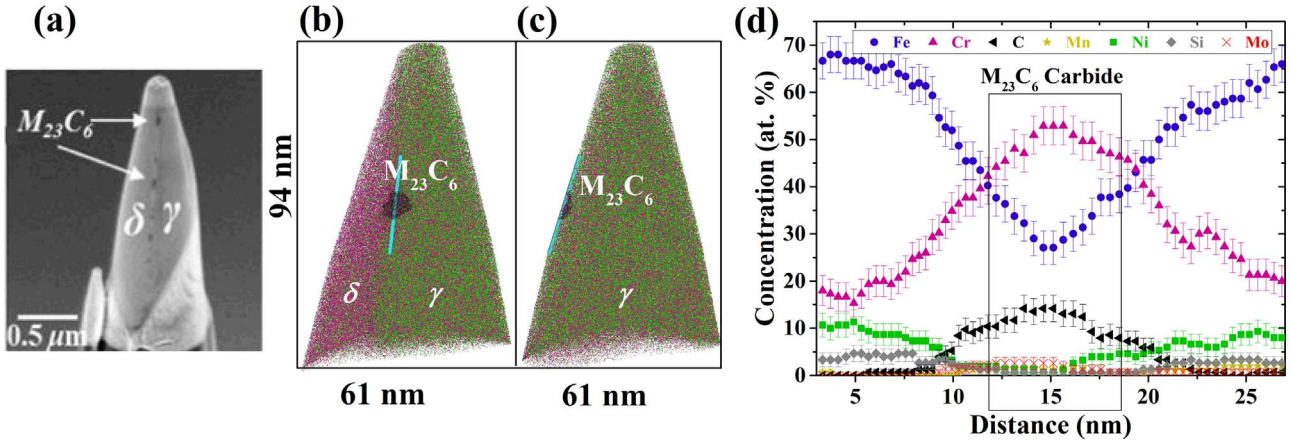

Fig. 7. (a) An SEM image of an APT specimen tip illustrating $M_{23}C_6$ carbides interspersed along the δ–ferrite/γ–austenite heterophase interface in CF–8. (b) APT reconstruction of the same unaged CF–8 data set as in Fig. 5(a), with a 2.5 at% C isoconcentration surface to better visualize the $M_{23}C_6$ carbide phase. Reconstruction dimensions: 94 nm × 61 nm. 0% of the Fe (blue) ions, 30% of the Cr ions (magenta), and 100% of Ni (green), Mn (mustard), Si (gray), Mo (red), and C (black) are depicted for clarity. (c) Rotated view of Fig. 6(b) to show that the carbide intersects the edge of the reconstruction volume. (d) One-dimensional (1D) concentration profiles using a 1 nm × 1 nm × 30 nm rectangular region of interest (ROI) seen in Fig. 6(b) for Fe (blue circles), Ni (green squares), Mn (mustard stars), Cr (magenta triangles), Si (gray diamonds), Mo (red asterisks), and C (black left–triangles) across the carbide phase. The ±2σ error bars are based on counting statistics. (For interpretation of the references to color in this figure legend, the reader is referred to the web version of this article.)

phase interfaces in CF–8, and exhibit a morphology similar to the one illustrated in Fig. 9(a)–(b). The lattice parameter, *a*, was measured as 1.109 nm in this study, which is slightly greater than the experimental value of $a = 1.065$ nm reported by Southwick and Honeycombe in a different DSS [41]. It is also similar to other values reported in the literature of approximately between 1.05 nm and 1.10 nm [42,43]. The lattice parameter is known to exhibit small variations due to differences in chemical composition [38–40].

A TEM-EDS line-scan was taken from the interior of the δ–ferrite phase grain across an $M_{23}C_6$ carbide and ending in the interior of the γ–austenite phase grain, Fig. 9(d). The results illustrate that the carbide is enriched in Cr and C, and contains smaller quantities of Mn, Ni, Mo, and Si. The carbide is depleted in Fe and Ni when compared to the adjacent ferrite and austenite phases. Furthermore, a depletion of Cr in the b.c.c. δ–ferrite phase is observed up to a distance of approximately 50 nm away from the heterophase interface, which suggests the presence of a solute depleted zone (SDZ). These observations support the APT observations that the $M_{23}C_6$ carbide contains metallic elements other than Cr. Additionally, earlier STEM-EDS observations in a different steel containing a smaller nominal concentration of 2.6 wt% Cr also indicated that $M_{23}C_6$ carbides contain metallic elements other than Cr [44]. Recent first principles calculations of a model ternary alloy also illustrate that Fe can substitute on the Cr lattice forming a $Cr_{23-x}Fe_xC_6$ carbide [42].

The occurrence of the SDZ in the ferrite phase of CF–8 and not CF–3 suggests that the Cr-rich carbides locally influence the phases' composition. Additionally, the SDZ formation in the ferrite phase and not the austenite phase suggests that differences in Cr diffusivity in each phase also influence its formation. Since Cr is the predominant metallic element in the $M_{23}C_6$ carbide [45], its nonstoichiometric composition in the unaged CF–8 suggests that Cr diffuses into the carbide during aging while Fe, Mo, Ni, Mn, and Si most likely diffuse into the surrounding matrix phases thereby permitting its composition to approach equilibrium. In addition, since the $M_{23}C_6$ carbide is located at the heterophase interface, enhanced or short circuit diffusion of Cr from the ferrite phase into the carbide phase along the interface may occur. The diffusion of solute elements at grain boundaries and heterophase interfaces can be several orders of magnitude greater than in the bulk volume [46,47], and the formation of the SDZ in the ferrite phase of the unaged CF–8 suggests that the kinetics are fastest at the heterophase interface. The influence of the $M_{23}C_6$ carbide on the local Cr concentration at the heterophase interface and formation of an SDZ in the ferrite phase of CF–8 but not CF–3 is supported by APT observations where we measure a mean Cr concentration of 24.9 at% for CF–8, Figs. 6(b), and 28.7 at% in the ferrite phase for CF–3, Fig. 5(b). The mean Cr concentration is 22.3 at% in the austenite phase of both steels. Hence, formation of the carbide locally depletes the Cr concentration in the ferrite phase of CF–8. A similar SDZ was observed at a grain boundary (GB) in a multicomponent Fe-Cu steel due to the presence of an Fe_3C carbide at the interface and was also attributed to more rapid kinetics [48].

We now consider the differences in diffusivity of Cr between the two

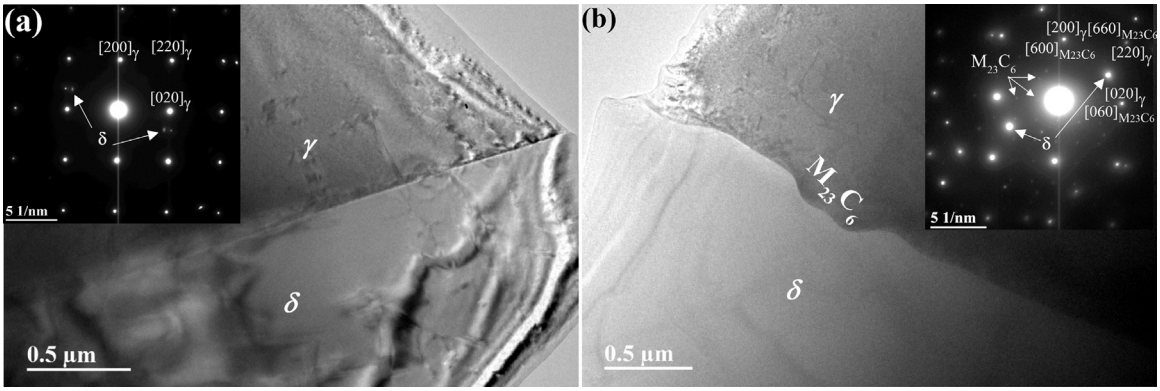

Fig. 8. Conventional TEM images of the δ–ferrite/γ–austenite heterophase interface in (a) CF–3 and (b) CF–8 duplex stainless steels with (insets) selected area electron diffraction (SAED) patterns along a f.c.c. γ–austenite [001] zone axis.

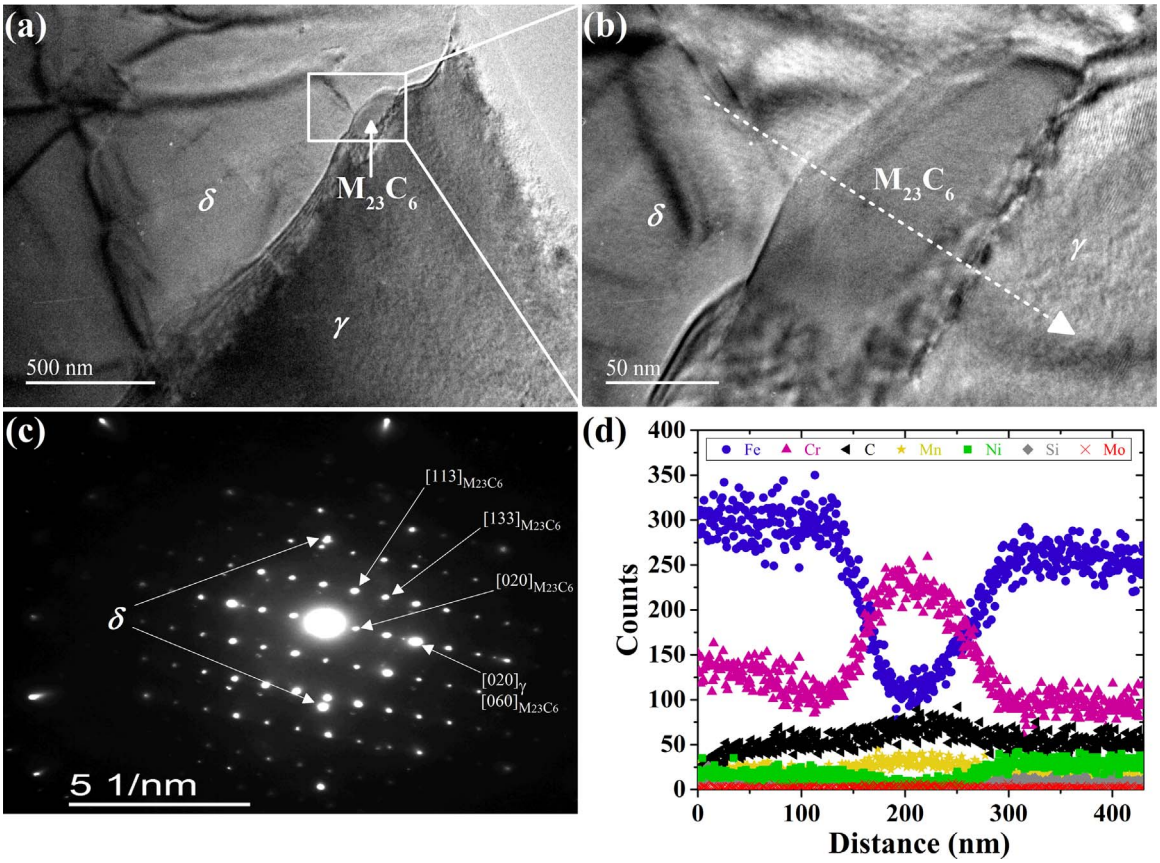

Fig. 9. (a)–(b) Conventional TEM images of an $M_{23}C_6$ carbide observed at the heterophase interface in CF–8 duplex stainless steel with (c) associated SAED pattern of the f.c.c. carbide along the γ–austenite/$M_{23}C_6$ $[\bar{3}01]$ zone axis and (d) TEM-EDS scan results of element concentrations taken along a 430 nm line across the $M_{23}C_6$ carbide from the δ–ferrite phase to the γ–austenite phase along the dashed arrow in Fig. 9(b).

phases. Williams and Faulkner studied Cr diffusion in ferritic and austenitic steels [49] and found that Cr in b.c.c. ferrite had a diffusion constant of $D_o = 0.15(^{+0.54}_{-0.12})\ \mathrm{cm^2\ s^{-1}}$ and activation energy of $Q = 210(\pm 15)\ \mathrm{kJ\ mol^{-1}}$, whereas Cr in f.c.c. austenite had a diffusion constant of $D_o = 0.27(^{+1.04}_{-0.22})\ \mathrm{cm^2\ s^{-1}}$ and $Q = 264(\pm 16)\ \mathrm{kJ\ mol^{-1}}$. The Arrhenius diffusion equation of Cr is $\overline{D}_{Cr} = D_o e^{-Q/RT}$, where R is the gas constant $8.31\ J(\mathrm{mol\ K})^{-1}$ and T is the absolute temperature. The diffusion distance during solution treatment can be determined to a first order approximation using the solution treatment temperature of 1338 K (1065 °C). The 3D root-mean-square (RMS) diffusion distance of Cr, $\langle x_{Cr} \rangle = \sqrt{6 \times \overline{D}_{Cr} \times t}$, is 64.1 μm in ferrite, and 7.6 μm in austenite where t is the solution treatment time of 7200 s. Thus, Cr has a diffusion distance in the ferrite phase an order of magnitude greater than in the austenite phase for the same time interval indicating that the Cr diffusion kinetics are more rapid in ferrite thereby promoting the formation of a Cr SDZ at the interface.

The aforementioned results demonstrate that the lower impact toughness, higher UTS, and higher Vickers microhardness observed in the unaged CF–8 steel are likely due to the presence of the carbides at the heterophase interfaces. Carbides were also observed at the heterophase interfaces of CF–8 steels aged to 4300 h. We do not, however, observe $M_{23}C_6$ carbides in CF–3 in the unaged condition or after aging to 4300 h at either operational or accelerated temperatures. These observations are in contrast to those in Refs. [5,7,11], which only observed the carbide phase in CF–8 aged at ≥400 °C. Thus, some studies have suggested that care must be taken in using 400 °C as an accelerated temperature in CF–8, as it may not be representative of aging at operational temperatures. Our observations suggest, however, that contribution to embrittlement in CF–8 by the $M_{23}C_6$ carbide can occur at both operational and accelerated aging temperatures since the carbide is present following solidification and solution treatment. It has been previously shown that the $M_{23}C_6$ carbide phase can form at the δ–ferrite/γ–austenite heterophase interfaces during the austenite-to-ferrite transformation in steels [50,51], and hence its presence can reasonably be expected in the unaged CF–8 steels, as has been observed here.

3.2.3. Atom probe tomography (APT): spinodal decomposition

Incipient spinodal decomposition as illustrated by concentration fluctuations in the ferrite phase of the unaged CF–8 stainless steel was observed, Fig. 2(a)–(b). The ferrite phase of the unaged CF–3 stainless steel also exhibited incipient spinodal decomposition that was qualitatively similar to that observed in the CF–8 steel. Spinodal decomposition in the CDSS is described as phase separation of the δ–ferrite phase into Fe-rich α–domains (blue) and Cr-rich α'–domains (magenta). Our observations are similar to those in unaged model Fe–25Cr at%, Fe–30Cr at%, and Fe–36Cr at% binary alloys where the authors suggested that small amounts of decomposition may be present in the unaged ferrite phase due to the presence of positive Cr–Cr interactions at short distances when using radial distribution function (RDF) analysis [52]. Moreover, an earlier study by Pumphrey and Akhurst on an unaged CF–3 steel suggested that a small spinodal amplitude exists in the ferrite phase, but the wavelength was not determined [9]. Phase decomposition in the ferrite phase is seen to progress and the wavelength and amplitudes of the concentration fluctuations are observed to increase during aging to 4300 h as illustrated for the CF–8 steel at 400 °C, Fig. 10(a)–(b). Additionally, a small G–phase precipitate is observed at an α–domain/α'–domain interface in Fig. 10(a) and is discussed below. The increase in wavelength and

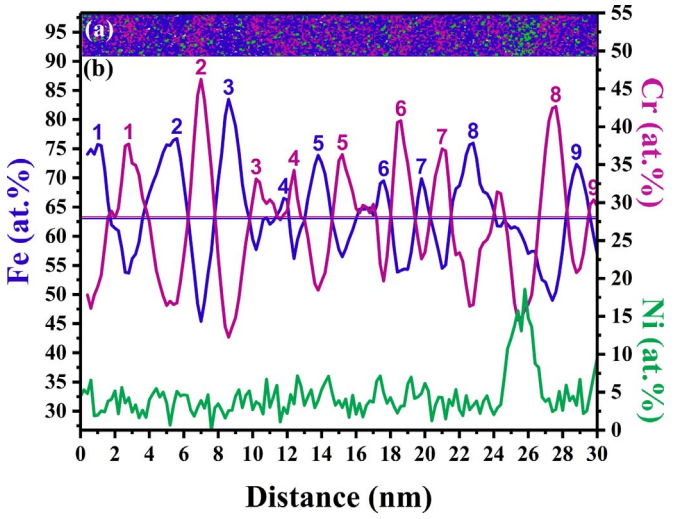

Fig. 10. (a) An example region of interest (ROI) illustrating the compositional heterogeneity of alternating Fe-rich α–domains (blue), Cr-rich α'–domains (magenta), and a Ni-rich G–phase precipitate (green) with (b) corresponding Fe, Cr, and Ni concentration profiles for CF–8 specimen aged to 4300 h at 400 °C. The Fe and Cr mean concentrations are superimposed in the plot as solid horizontal lines. (For interpretation of the references to color in this figure legend, the reader is referred to the web version of this article.)

amplitude occurs at the two operational and the two accelerated aging temperatures in both steels.

The Cr wavelength and amplitude size distributions in the unaged CF–3 and CF–8 stainless steels are illustrated in Fig. 11(a)–(b) and Fig. 11(c)–(d), respectively. The binomial distribution of random wavelengths and amplitudes are superimposed on both figures and differ from the experimentally measured distributions. The quantity MW for Cr in CF–3 is 1.9 ± 0.2 nm and 1.8 ± 0.2 nm in CF–8. The quantity MA for Cr in the CF–3 steel is 4.4 ± 0.2 nm and 4.4 ± 0.2 nm in the CF–8 steel. The MW values are slightly different than the mean wavelength determined by the ACF method, whereas the MA values exhibit greater difference with the amplitude determined by the LBM method, Fig. 12(a)–(b).

In order to account for the measured differences in local mean Cr concentration in the b.c.c. δ–ferrite phase on the Cr spinodal decomposition amplitudes between the CF–3 and CF–8 steels, a ratio of normalized spinodal decomposition amplitudes, A_j^*, was calculated for an element j, $A_j^* = |A_i^{CF-8}|/|A_i^{CF-3}| = \{(A_j^{CF-8}/\overline{C}_j^{CF-8})\}/\{A_j^{CF-3}/\overline{C}_j^{CF-3}\}$. The mean concentrations used in the equation for the quantity A_j^* are from the proxigrams in Figs. 5(b) and 6(b) for CF–3 and CF–8, respectively. The quantity A_j^* for Cr is 1.15, which indicates the normalized Cr amplitude is greater in the CF–8 steel. A decrease of the local mean Cr concentration in the ferrite phase may affect the Cr atomic mobility due to the concentration dependence of the interdiffusion coefficient [53,54] in the Cahn–Hilliard equations and thus lead to

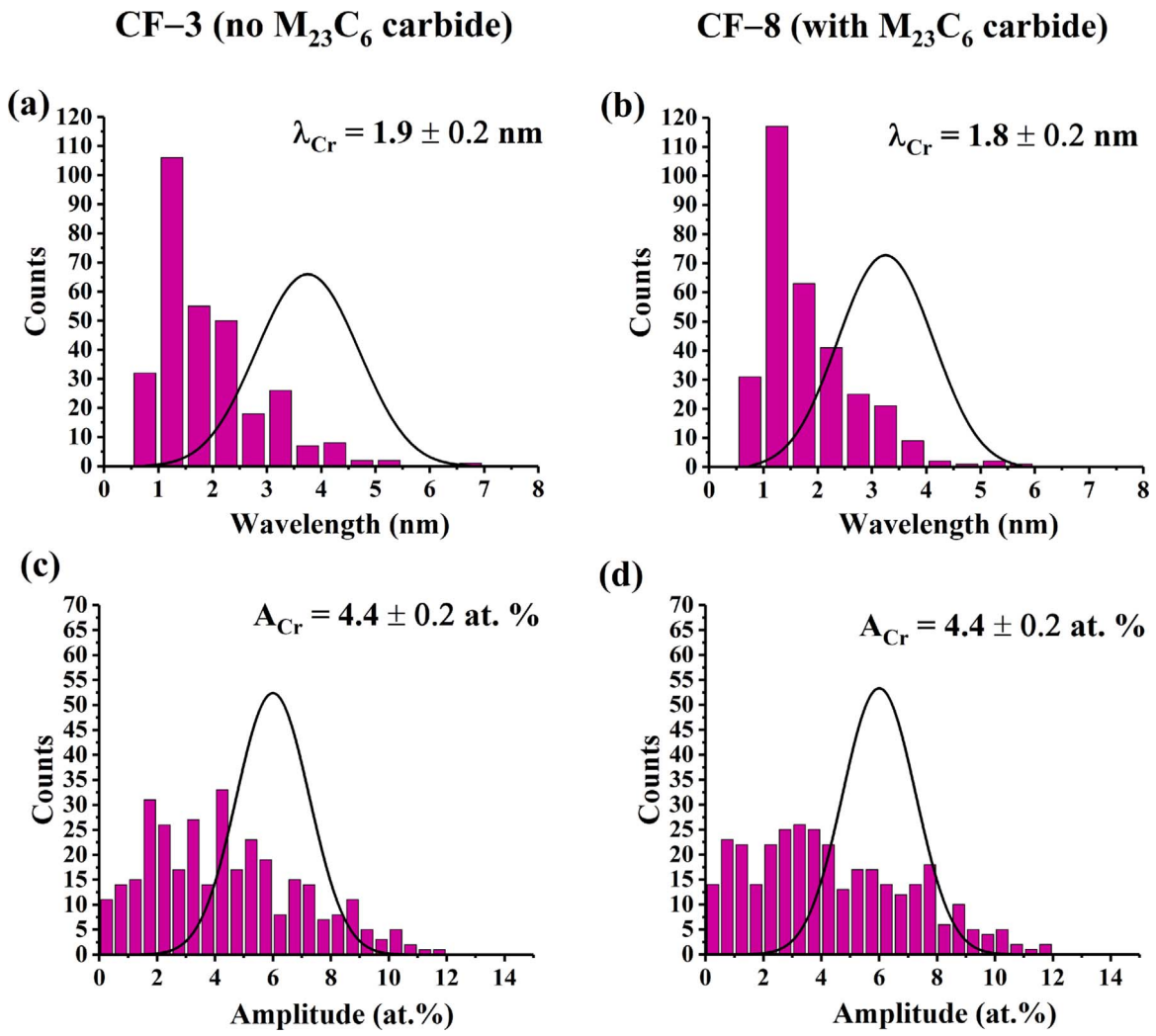

Fig. 11. Distribution histograms of Cr with superimposed random binomial distribution curves for unaged (a) CF–3 wavelength, (b) CF–8 wavelength, (c) CF–3 amplitude, and (d) CF–8 amplitude.

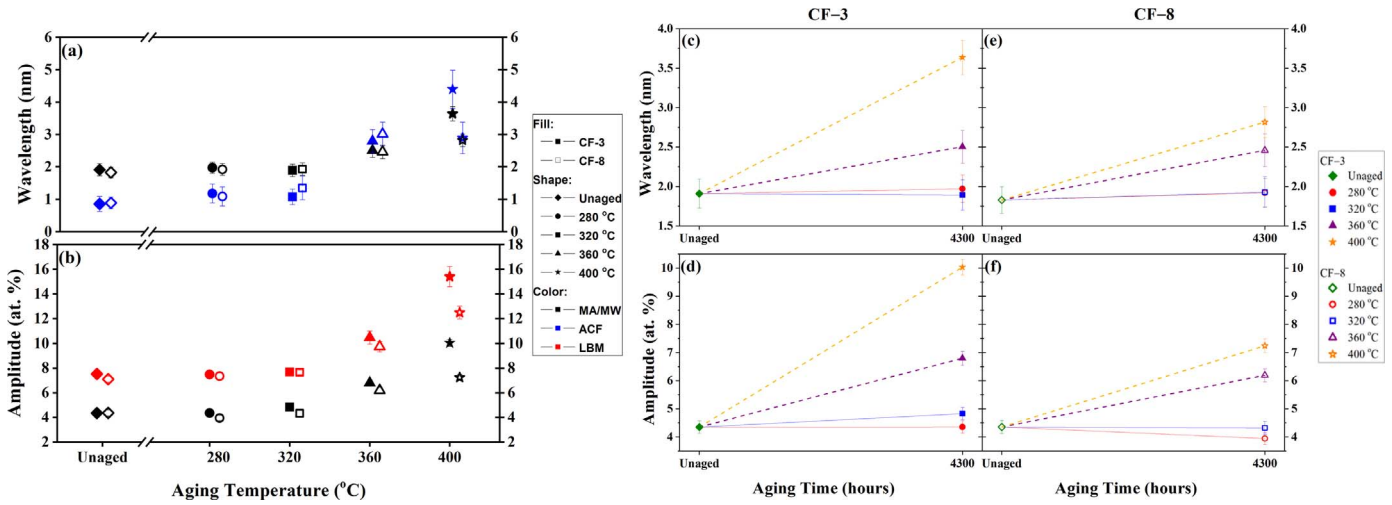

Fig. 12. (a) The mean wavelength (MW) and (b) mean amplitude (MA) values of CF–3 (solid symbols) and CF–8 (open symbols) are plotted as a function of aging temperatures: unaged (diamonds) and specimens aged to 4300 h at 280 °C (circles), 320 °C (squares), 360 °C (triangles), and 400 °C (stars). The MW values (black) are compared to the auto correlation function (ACF) method wavelengths (blue) and the MA values (black) are compared to the Langer Bar-on Miller (LBM) method amplitudes (red). The ACF and LBM method values are staggered to the right of the MW and MA values by 5 °C for clarity. The mean wavelength (MW) of (c) CF–3 and (e) CF–8 and the mean amplitude (MA) of (d) CF–3 and (f) CF–8 are plotted as a function of aging time. Solid symbols indicate CF–3 while open symbols indicate CF–8. Trend lines from the unaged data to the aged data are drawn with corresponding colors. The operational temperatures (280 °C and 320 °C) are solid lines, while the accelerated temperatures (360 °C and 400 °C) are dashed lines. (For interpretation of the references to color in this figure legend, the reader is referred to the web version of this article.)

different spinodal decomposition amplitudes in the steels. The small differences in nominal composition between the two steels suggest that incipient spinodal decomposition should be similar since the two steels would have a similar position in the miscibility gap of the phase diagram and hence the driving force for phase separation would be similar. The APT results demonstrate, however, that the normalized Cr amplitude in the unaged CF–8 steel is greater than in the CF–3 steel. This is possibly due to the presence of the Cr-rich $M_{23}C_6$ carbide phase in CF–8 and not CF–3 that locally influences the Cr concentration in the ferrite phase by formation of the SDZ, as discussed above. In addition to the direct influence of the carbide phase on the measured differences in mechanical properties of the unaged steels, it is possible that the carbide also indirectly influences thermal embrittlement by affecting the Cr concentrations and amount of spinodal decomposition in the ferrite phase. The smaller differences in mechanical properties between the steels after aging to 4300 h at accelerated temperatures when compared to operational temperatures suggest, however, that this effect may be limited to earlier stages of decomposition.

After aging to 4300 h, the quantities MW and MA for Cr derived from wavelength and amplitude size distributions increase as illustrated in Fig. 12(a)–(f). The quantities MW and MA exhibit an increasing trend with increasing aging temperature and their values are greater for both accelerated temperatures when compared to the two operational temperatures for both steels. Additionally, only small differences are exhibited in the quantities MW and MA between the two steels at operational temperatures. The difference in values of these quantities, are however, slightly greater at accelerated temperatures and this may be caused by the influence of the G–phase precipitates on spinodal decomposition, as discussed below. The quantity MW exhibits slight differences when compared to the mean wavelength determined by the ACF method but both methods illustrate similar trends. The amplitude determined by the LBM method is consistently greater than when compared to the quantity MA but both values exhibit similar trends. Earlier studies of evaluating spinodal decomposition have illustrated quantitative differences between various methods of determining amplitude although they may exhibit similar trends [28,52]. In this study, the differences observed between the LBM method and the quantity MA is due to their underlying basis. The LBM method is categorized as a peak-to-trough amplitude method, whereas the method presented in this study is a peak-to-mean composition amplitude method and thus the former will have quantitative values approximately twice as great as the latter. Furthermore, the LBM method is dependent on symmetry of the frequency distributions [52], and multicomponent alloys whose nominal or local compositions are not centered in the miscibility gap of the phase diagram, such as the CF–3 and CF–8 CDSS in this study, will exhibit asymmetry and thus the LBM method can produce greater variability in its results.

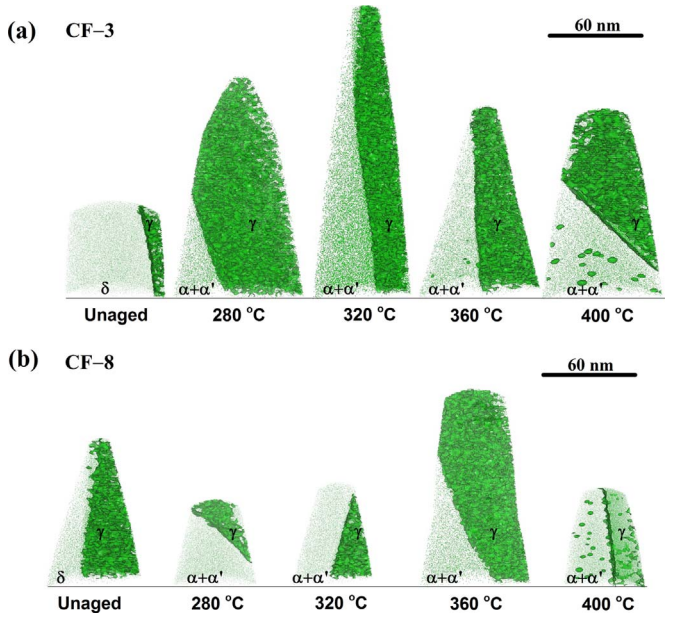

Fig. 13. (a) Series of APT reconstructions illustrating G–phase precipitates in the decomposing δ–ferrite phase delineated by 6.5 at% Ni (green) isoconcentration surfaces in unaged and 4300 h aged CF–3 specimens. (b) Series of G–phase precipitates delineated by 6.5 at% Ni (green) isoconcentration surfaces in unaged and 4300 h aged CF–8 specimens. The G–phase precipitates are only observed in CF–3 aged at 360 °C and 400 °C, and CF–8 aged at 400 °C. The γ–austenite phase has a Ni concentration greater than the 6.5 at% threshold and thus is displayed as large green isosurfaces. Only displaying 10% of the Ni (green) atoms for clarity. (For interpretation of the references to color in this figure legend, the reader is referred to the web version of this article.)

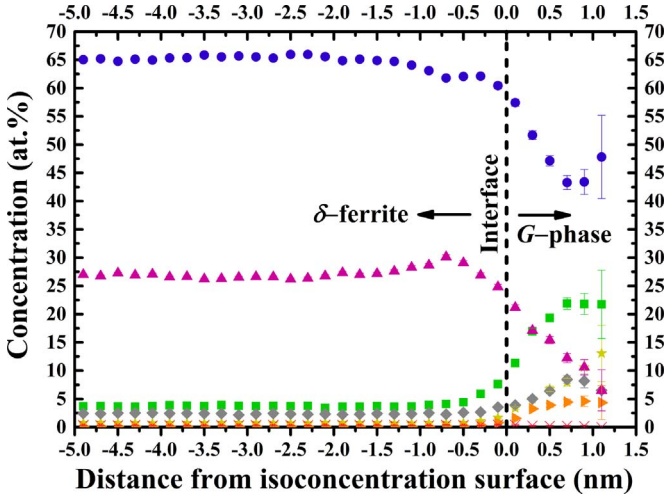

Fig. 14. Example G–phase precipitate proximity histogram concentration profiles in CF–8 aged to 4300 h at 400 °C for Fe (blue circles), Ni (green squares), Mn (mustard stars), Cr (magenta triangles), Si (gray diamonds), Mo (red asterisks), and Cu (orange right–triangles) using a 6.5 at% Ni isoconcentration surface. The ±2σ error bars are based on counting statistics. For the major elements, the error bars are smaller than the marker size. (For interpretation of the references to color in this figure legend, the reader is referred to the web version of this article.)

Table 2
Composition of G–phase precipitates in CF–3 and CF–8 after 4300 h aging as measured by atom probe tomography (APT).

		Composition (at%)						
		Fe	Cr	Ni	Si	Mn	Cu	Mo
CF–3	360 °C	54.19	19.07	17.21	3.72	4.19	0.93	0.23
	400 °C	40.14	15.05	22.23	7.44	7.18	6.83	0.61
CF–8	360 °C	ND	ND	ND	ND	ND	ND	ND
	400 °C	45.60	13.88	20.39	7.21	7.58	4.14	0.23

ND=Not detected.

3.2.4. Atom probe tomography (APT): G–phase precipitates

G–phase precipitates were not observed in the unaged specimens or the specimens aged at operational temperatures in both steels, as illustrated in Fig. 13(a)–(b). G–phase precipitates are detected inside the decomposing ferrite phase of CF–3 aged at 360 °C and 400 °C, and CF–8 aged at 400 °C. The G–phase is observed to form at the α/α' interfaces as illustrated in Fig. 10(a)–(b). The G–phase is a ternary intermetallic silicide that has a nominal stoichiometric composition of $Ni_{16}Si_7Ti_6$ [55]. However, other metallic elements such as Cr, Fe, and Mn can substitute for Ni and titanium (Ti) [6,55,56]. As depicted in the example proxigram concentration profiles of CF–8 aged at 400 °C in Fig. 14, the G–phase precipitates are enriched in Ni, Si, Mn, and Cu but are depleted in Fe, Cr, and Mo and their compositional analysis is reported in Table 2. Copper is present as a residual element in the steels. The precipitates still contain measurable concentrations of Fe and Cr after aging to 4300 h. It is possible that both elements diffuse out of the G–phase while Ni, Si, and Mn diffuse into the G–phase during further aging and the precipitates approach their equilibrium compositions. This is supported by the lower Fe and Cr concentrations and concomitantly higher Ni, Si, and Mn concentrations at 400 °C aging when compared to the slower kinetics at 360 °C aging for the CF–3 steel. Trajectory aberrations and local magnifications effects may also influence the Fe and Cr concentrations in the G–phase. However, since the quantity $< R >$ is > 1 nm, this will have limited effect on the core compositions [57]. Furthermore, recent studies of the G–phase in CF–3M illustrated that Fe and Cr concentrations decrease while Ni, Mn, Si, and Mo concentrations increase in the precipitates with increasing aging time at accelerated temperatures [12,21]. The quantities $< R >$, N_V, and V_f of the G–phase precipitates in CF–3 are greater than that of CF–8 when aging at 400 °C, Table 3, which suggests that the kinetics of G–phase formation are slower in the latter. Further, the same morphological parameters are greater when aging at 400 °C than 360 °C in CF–3 due to faster kinetics. Comparison of the precipitate radii, number density, and volume percentage results for CF–3 at 360 °C and 400 °C in this study to CF–3M at 350 °C and 400 °C in Ref. [21] suggests that the kinetics of G–phase formation is slower in CF–3. These differences can be accounted for by variations in nominal composition, solution treatment, and heterogeneous distribution of the G–phase precipitates. The CF–3M steel in Ref. [21] had a greater nominal concentration of Ni, which is known to accelerate G–phase formation, and a greater nominal concentration of Mo, which is also known to promote G–phase precipitation [7].

Table 3
Mean radius, $< R >$, number density, N_V, and volume percentage, V_f, of G–phase precipitates in CF–3 and CF–8 after 4300 h aging as measured by atom probe tomography (APT).

		Parameters		
		$\langle R \rangle$ (nm)	N_V (ppt/m^3)	V_f (%)
CF–3	360 °C	1.1 ± 0.4	$9.5 \times 10^{22} \pm 4.1 \times 10^{22}$	0.1 ± 0.02
	400 °C	2.0 ± 0.2	$1.7 \times 10^{23} \pm 4.3 \times 10^{22}$	0.8 ± 0.02
CF–8	360 °C	ND	ND	ND
	400 °C	1.6 ± 0.3	$1.3 \times 10^{23} \pm 3.3 \times 10^{22}$	0.4 ± 0.02

ND=Not detected.

3.2.5. Comparison of mechanical property and microstructural evolution

In general, the increasing Vickers microhardness, increasing UTS, and decreasing CVN impact toughness in both steels as illustrated in Fig. 3(a)–(f) corresponds to increasing values for the quantities MW and MA in both steels as illustrated in Fig. 12(a)–(f). Additionally, the greater values for MW and MA at accelerated temperatures compared to operational temperatures correspond in general to the greater degradation of the mechanical properties at the accelerated temperatures. As discussed above, the extent of spinodal decomposition increases with increasing temperature. In addition to the contribution by spinodal decomposition, G–phase precipitation at accelerated temperatures may influence embrittlement but its contribution has been debated in the literature and is not completely clear. The G–phase was reported to contribute to embrittlement in Refs. [58,59,60], whereas it was reported to have more limited contributions in Refs. [5,11,12]. We measure little difference in the degree of mechanical property degradation at 360 °C aging between CF–3 with G–phase precipitation and CF–8 without G–phase precipitation thereby suggesting that its direct contribution is limited. It is possible, however that the G–phase could indirectly influence embrittlement by locally altering the Ni concentration, which would in turn influence kinetics of spinodal decomposition in the ferrite phase as suggested in Refs. [6,11].

4. Conclusion

The effect of aging temperatures on the mechanical property degradation and phase decomposition in CF–3 and CF–8 steels was studied experimentally. The δ–ferrite/γ–austenite heterophase interface, $M_{23}C_6$ carbide, spinodal decomposition, and G–phase precipitation were analyzed in unaged and aged steels. The steels were aged at operational temperatures of 280 °C and 320 °C and accelerated temperatures of 360 °C and 400 °C for 4300 h. This investigation resulted

in the following findings:

(1) Compared to the unaged CF–3 steel, the unaged CF–8 steel has higher UTS and Vickers microhardness values, but lower CVN impact toughness values. The CF–3 steel has a UTS of 530 MPa, Vickers microhardness of 151.8 ± 4.6 HV500g, and impact toughness of 392 ± 14 J. The CF–8 steel has a UTS of 570 MPa, Vickers microhardness of 165.8 ± 5.8 HV500g, and impact toughness of 317 ± 80 J.
(2) Selected area electron diffraction (SAED) observations illustrated that a $M_{23}C_6$ carbide is present at the heterophase interphases of the unaged CF–8 steel but not the unaged CF–3 steel, and it is not present in the interior of the grains in either steel. The carbide phase is not observed in the CF–3 after aging to 4300 h. The $M_{23}C_6$ carbide has an f.c.c. crystal structure with a lattice parameter of 1.109 nm. It has a composition of 32.5 ± 2.1 at% Fe, 49.2 ± 1.5 at% Cr, 11.9 ± 1.2 at% C, 2.0 ± 0.4 at% Mo, 2.1 ± 0.7 at% Ni, 1.1 ± 0.2 at% Mn, and 0.65 ± 0.14 at% Si. A Cr solute depleted zone (SDZ) is present in the ferrite phase of the unaged CF–8 but not the unaged CF–3. In the ferrite phase, the Cr concentration was 28.7 at% in the CF–3 steel and 24.9 at% in the CF–8 steel with a carbide present at the heterophase interface.
(3) Incipient spinodal decomposition was observed in the b.c.c. δ–ferrite phase of the unaged CF–3 and CF–8 steels. The wavelength and amplitude size distributions differed from binomial distribution of random wavelengths and amplitudes. The spinodal domains in CF–3 steel have a mean wavelength (MW) of 1.8 ± 0.2 nm and a mean amplitude (MA) of 4.4 ± 0.2 at% Cr, whereas the domains in CF–8 steel have a MW of 1.9 ± 0.2 nm and a MA of 4.4 ± 0.2 at% Cr.
(4) After aging to 4300 h spinodal decomposition progresses and the quantities MW and MA increase for both steels at the two operational and two accelerated temperatures. These quantities are greater in the steels aged at accelerated temperatures than operational temperatures. Concomitantly, the Vickers microhardness and UTS increase while the CVN impact toughness values decrease for both steels. The mechanical property degradation is greater at accelerated temperatures than operational temperatures.
(5) G–phase precipitates were observed in CF–3 aged at 360 °C and both steels aged at 400 °C. The radius, number density, and volume percentage (fraction) of G–phase in CF–3 are greater than those in CF–8. The radius, number density, and volume percentage is 1.1 ± 0.4 nm, $9.5 \times 10^{22} \pm 4.1 \times 10^{22}$ ppts. /m^3, and 0.1 ± 0.02%, respectively, for the CF–3 steel aged at 360 °C; and is 2.0 ± 0.2 nm, $1.7 \times 10^{23} \pm 4.3 \times 10^{22}$ ppts. /m^3, and 0.8 ± 0.02%, respectively, for the CF–3 steel aged at 400 °C. The same parameters are 1.6 ± 0.3 nm, $1.3 \times 10^{23} \pm 3.3 \times 10^{22}$ ppts. /m^3, and 0.4 ± 0.02%, respectively, in the CF–8 steel aged at 400 °C.

Acknowledgements

This work is supported by the Department of Energy – Nuclear Energy University Program (DOE–NEUP), Contract no. DE–NE0000724; Dr. Jeremy T. Busby, Oak Ridge National Laboratory (ORNL), technical monitor. A part of this research was performed using the Environmental Molecular Sciences Laboratory (EMSL), a DOE Office of Science User Facility sponsored by the Office of Biological and Environmental Research and located at Pacific Northwest National Laboratory (PNNL). We would like to thank Mr. Michael Perna, University of Maryland (UMD), for machining all specimen blanks and mechanical property test specimens; Professor Isabel Lloyd, UMD, for use of the Vickers microhardness tester; and Dr. Robert Bonenberger, UMD, for his assistance with the equipment in the Modern Engineering Materials Instructional Laboratory (MEMIL). Ms. Sarah Mburu is partially supported by the National Science Foundation (NSF) Louis Stokes Alliances for Minority Participation (LSAMP) under Grant no. 0833018. Mr. Schwarm would like to acknowledge the Department of Energy: Office of Nuclear Energy (DOE-NE) Integrated University Program (IUP) fellowship program for support. We acknowledge the support of the Maryland NanoCenter and its AIMLab and FabLab.

References

[1] J.K. Sahu, U. Krupp, R.N. Ghosh, H.-J. Christ, Effect of 475 °C embrittlement on the mechanical properties of duplex stainless steel, Mater. Sci. Eng.: A 508 (1–2) (2009) 1–14.
[2] Y. Chen, B. Alexandreanu, K. Natesan, A.S. Rao, Environmentally assisted cracking and irradiation embrittlement of CF-8 and CF-8M cast austenitic stainless steels in high-purity water, Nucl. Energy Agency OECD (NEA) (2015).
[3] R.P. Kolli, et al., Characterization of element partitioning at the Austenite/Ferrite interface of as cast CF-3 and CF-8 duplex stainless steels, Microsc. Microanal. (Supplement S3) (2015) 365–366.
[4] Z.-X. Wang, F. Xue, W.-H. Guo, H.-J. Shi, G.-D. Zhang, G. Shu, Investigation of thermal aging damage mechanism of the cast duplex stainless steel, Nucl. Eng. Des. 240 (10) (2010) 2538–2543.
[5] M.K. Miller, J. Bentley, APFIM and AEM investigation of CF8 and CF8M primary coolant pipe steels, Mater. Sci. Technol. 6 (3) (1990) 285–292.
[6] F. Danoix, P. Auger, Atom probe studies of the Fe–Cr system and stainless steels aged at intermediate temperature: a review, Mater. Charact. 44 (1–2) (2000) 177–201.
[7] P. Auger, F. Danoix, A. Menand, S. Bonnet, J. Bourgoin, M. Guttmann, Atom probe and transmission electron microscopy study of aging of cast duplex stainless steels, Mater. Sci. Technol. 6 (3) (1990) 301–313.
[8] P. McConnell, W. Sheckherd, D. Norris, Properties of thermally embrittled cast duplex stainless steel, J. Mater. Eng. 11 (3) (1989) 227–236.
[9] P.H. Pumphrey, K.N. Akhurst, Aging kinetics of CF3 cast stainless steel in temperature range 300–400 °C, Mater. Sci. Technol. 6 (3) (1990) 211–220.
[10] H.M. Chung, Aging and life prediction of cast duplex stainless steel components, Int. J. Press. Vessels Pip. 50 (1) (1992) 179–213.
[11] H.M. Chung, T.R. Leax, Embrittlement of laboratory and reactor aged CF3,CF8, and CF8M duplex stainless steels, Mater. Sci. Technol. 6 (3) (1990) 249–262.
[12] C. Pareige, S. Novy, S. Saillet, P. Pareige, Study of phase transformation and mechanical properties evolution of duplex stainless steels after long term thermal ageing (> 20 years), J. Nucl. Mater. 411 (1–3) (2011) 90–96.
[13] O.K. Chopra, Initial assessment of the mechanisms and significance of low-temperature embrittlement of cast stainless steels in LWR systems, Div. Eng. Off. Nucl. Regul. Res. U.S. Nucl. Regul. Comm. (1990).
[14] O.K. Chopra, G. Ayrault, Aging degradation of cast stainless steel: status and program, Nucl. Eng. Des. 86 (1) (1985) 69–77.
[15] O.K. Chopra, H.M. Chung, Aging of cast duplex stainless steels in LWR systems, Nucl. Eng. Des. 89 (2–3) (1985) 305–318.
[16] T.S. Byun, Y. Yang, N.R. Overman, J.T. Busby, Thermal aging phenomena in cast duplex stainless steels, JOM 68 (2) (2015) 507–516.
[17] S. Bonnet, J. Bourgoin, J. Champredonde, D. Guttmann, M. Guttmann, Relationship between evolution of mechanical properties of various cast duplex stainless steels and metallurgical and aging parameters: outline of current EDF programmes, Mater. Sci. Technol. 6 (3) (1990) 221–229.
[18] S. Mburu, et al., Atom probe tomography analysis of the local chemical environment at the austenite/ferrite interfaces of cast duplex stainless steels, in: Engineering Innovation for Global Sustainability: Proceedings of the 14th LACCEI International Multi-Conference for Engineering, Education, and Technology, Jul, 2016.
[19] O.K. Chopra, H.M. Chung, Effect of Low-Temperature Aging on the Mechanical Properties of Cast Stainless Steels, Argonne National Lab, IL (USA), 1987.
[20] T. Hamaoka, A. Nomoto, K. Nishida, K. Dohi, N. Soneda, Accurate determination of the number density of G-phase precipitates in thermally aged duplex stainless steel, Philos. Mag. 92 (22) (2012) 2716–2732.
[21] T. Hamaoka, A. Nomoto, K. Nishida, K. Dohi, N. Soneda, Effects of aging temperature on G-phase precipitation and ferrite-phase decomposition in duplex stainless steel, Philos. Mag. 92 (34) (2012) 4354–4375.
[22] J. Emo, C. Pareige, S. Saillet, C. Domain, P. Pareige, Kinetics of secondary phase precipitation during spinodal decomposition in duplex stainless steels: a kinetic Monte Carlo model – comparison with atom probe tomography experiments, J. Nucl. Mater. 451 (1–3) (2014) 361–365.
[23] D. Isheim, R.P. Kolli, M.E. Fine, D.N. Seidman, An atom-probe tomographic study of the temporal evolution of the nanostructure of Fe–Cu based high-strength low-carbon steels, Scr. Mater. 55 (1) (2006) 35–40.
[24] A. Devaraj, et al., Three-dimensional nanoscale characterisation of materials by atom probe tomography, Int. Mater. Rev. (2017). http://dx.doi.org/10.1080/09506608.2016.1270728.
[25] J.W. Cahn, On spinodal decomposition, Acta Metall. 9 (9) (1961) 795–801.
[26] J.W. Cahn, J.E. Hilliard, Free energy of a nonuniform system. I. interfacial free energy, J. Chem. Phys. 28 (2) (1958) 258–267.
[27] M.K. Miller, J.M. Hyde, M.G. Hetherington, A. Cerezo, G.D.W. Smith, C.M. Elliott, Spinodal decomposition in Fe-Cr alloys: experimental study at the atomic level and comparison with computer models—I. Introduction and methodology, Acta Metall. Et. Mater. 43 (9) (1995) 3385–3401.
[28] M.K. Miller, A. Cerezo, M.G. Hetherington, J.M. Hyde, Estimation of composition

amplitude: Pa and LBM versus V, Surf. Sci. 266 (1) (1992) 446–452.
[29] M.K. Miller, K.F. Russell, K. Thompson, R. Alvis, D.J. Larson, Review of atom probe FIB-based specimen preparation methods, Microsc. Microanal. 13 (06) (2007) 428–436.
[30] K. Thompson, D. Lawrence, D.J. Larson, J.D. Olson, T.F. Kelly, B. Gorman, In situ site-specific specimen preparation for atom probe tomography, Ultramicroscopy 107 (2–3) (2007) 131–139.
[31] R.P. Kolli, F. Meisenkothen, A focused ion beam specimen Preparation method to minimize gallium ion concentration in copper atom-probe tomography specimen tips, Microsc. Microanal. 20 (S3) (2014) 350–351.
[32] O.C. Hellman, J.A. Vandenbroucke, J. Rüsing, D. Isheim, D.N. Seidman, Analysis of three-dimensional atom-probe data by the proximity histogram, Microsc. Microanal. 6 (05) (2000) 437–444.
[33] R.P. Kolli, D.N. Seidman, Comparison of compositional and morphological atom-probe tomography analyses for a multicomponent Fe-Cu steel, Microsc. Microanal. 13 (4) (2007) 272–284.
[34] B. Gault, M.P. Moody, J.M. Cairney, S.P. Ringer, Atom Probe Microscopy 160, Springer New York, New York, NY, 2012.
[35] M.D. Mathew, L.M. Lietzan, K.L. Murty, V.N. Shah, Low temperature aging embrittlement of CF-8 stainless steel, Mater. Sci. Eng.: A 269 (1–2) (1999) 186–196.
[36] W.F. Michaud, P.T. Toben, W.K. Soppet, O.K. Chopra, Tensile-property Characterization of Thermally Aged Cast Stainless Steels, Division of Engineering, Office of Nuclear Regulatory Research, U.S. Nuclear Regulatory Commission, Washington, D.C., 1994.
[37] S.C. Schwarm, R.P. Kolli, E. Aydogan, S. Mburu, S. Ankem, Characterization of phase properties and deformation in ferritic-austenitic duplex stainless steels by nanoindentation and finite element method, Mater. Sci. Eng.: A 680 (2017) 359–367.
[38] S.C. Schwarm, S. Mburu, R.P. Kolli, D.E. Perea, J. Liu, S. Ankem, Mechanical and microstructural effects of thermal aging on cast duplex stainless steels by experiment and finite element method, in: I. Charit, Y.T. Zhu, S.A. Maloy, P.K. Liaw (Eds.), Mechanical and Creep Behavior of Advanced Materials, Springer International Publishing, Cham, Switzerland, 2017, pp. 253–262.
[39] S.L. Li, et al., Microstructure evolution and impact fracture behaviors of Z3CN20-09M stainless steels after long-term thermal aging, J. Nucl. Mater. 433 (1–3) (2013) 41–49.
[40] Y.H. Yao, J.F. Wei, Z.P. Wang, Effect of long-term thermal aging on the mechanical properties of casting duplex stainless steels, Mater. Sci. Eng.: A 551 (2012) 116–121.
[41] P.D. Southwick, R.W.K. Honeycombe, Precipitation of M23C6 at austenite/ferrite interfaces in duplex stainless steel, Met. Sci. 16 (10) (1982) 475–482.
[42] J.Y. Xie, N.X. Chen, L.D. Teng, S. Seetharaman, Atomistic study on the site preference and thermodynamic properties for Cr23−xFexC6, Acta Mater. 53 (20) (2005) 5305–5312.
[43] J.J. Han, C.P. Wang, X.J. Liu, Y. Wang, Z.-K. Liu, First-principles calculation of structural, mechanical, magnetic and thermodynamic properties for γ-M 23 C 6 (M=Fe, Cr) compounds, J. Phys.: Condens. Matter 24 (50) (2012) 505503.
[44] J. Janovec, A. Vyrostkova, M. Svoboda, Influence of tempering temperature on stability of carbide phases in 2.6cr-0.7mo-0.3v steel with various carbon content, Metall. Mater. Trans. A 25 (2) (1994) 267–275.
[45] T.S. Byun, Y. Yang, N.R. Overman, J.T. Busby, Thermal aging phenomena in cast duplex stainless steels, JOM 68 (2) (2016) 507–516.
[46] David A. Porter, K.E. Easterling, Phase Transformations in Metals and Alloys, 3rd ed., CRC Press, Boca Raton, FL, 2009.
[47] R.W. Balluffi, S. Allen, W.C. Carter, Kinetics of Materials, John Wiley & Sons, Oxford, UK, 2005.
[48] R.P. Kolli, D.N. Seidman, Co-precipitated and collocated carbides and Cu-rich precipitates in a Fe–Cu steel characterized by atom-probe tomography, Microsc. Microanal. 20 (06) (2014) 1727–1739.
[49] P.I. Williams, R.G. Faulkner, Chemical volume diffusion coefficients for stainless steel corrosion studies, J. Mater. Sci. 22 (10) (1987) 3537–3542.
[50] R.W.K. Honeycombe, R.F. Mehl, Transformation from austenite in alloy steels, Metall. Trans. A 7 (7) (1976) 915–936.
[51] H.K.D.H. Bhadeshia, Diffusional formation of ferrite in iron and its alloys, Prog. Mater. Sci. 29 (4) (1985) 321–386.
[52] J. Zhou, J. Odqvist, M. Thuvander, P. Hedström, Quantitative evaluation of spinodal decomposition in Fe-Cr by atom probe tomography and radial distribution function analysis, Microsc. Microanal. 19 (3) (2013) 665–675.
[53] T. Kuwajima, Y. Saito, Y. Suwa, Kinetics of phase separation in iron-based ternary alloys. II. Numerical simulation of phase separation in Fe–Cr–X(X=Mo, Cu) ternary alloys, Intermetallics 11 (11–12) (2003) 1279–1285.
[54] Y.S. Yoshihiro Suwa, Kinetics of phase separation in Fe-Cr-Mo ternary alloys, Mater. Trans. A 43 (2) (2002) 271–276.
[55] K.H. Lo, C.H. Shek, J.K.L. Lai, Recent developments in stainless steels, Mater. Sci. Eng.: R: Rep. 65 (4–6) (2009) 39–104.
[56] Y. Matsukawa, et al., The two-step nucleation of G-phase in ferrite, Acta Mater. 116 (2016) 104–113.
[57] F. Vurpillot, A. Bostel, D. Blavette, Trajectory overlaps and local magnification in three-dimensional atom probe, Appl. Phys. Lett. 76 (21) (2000) 3127–3129.
[58] T.R. Leax, S.S. Brenner, J.A. Spitznagel, Atom probe examination of thermally ages CF8M cast stainless steel, Metall. Trans. A 23 (10) (1992) 2725–2736.
[59] T. Yamada, S. Okano, H. Kuwano, Mechanical property and microstructural change by thermal aging of SCS14A cast duplex stainless steel, J. Nucl. Mater. 350 (1) (2006) 47–55.
[60] W. Guo, D.A. Garfinkel, J.D. Tucker, D. Haley, G.A. Young, J.D. Poplawsky, An atom probe perspective on phase separation and precipitation in duplex stainless steels, Nanotechnology 27 (25) (2016) 254004.

Materials Science & Engineering A 680 (2017) 359–367

Contents lists available at ScienceDirect

Materials Science & Engineering A

journal homepage: www.elsevier.com/locate/msea

Characterization of phase properties and deformation in ferritic-austenitic duplex stainless steels by nanoindentation and finite element method

Samuel C. Schwarm[a,*], R. Prakash Kolli[a], Eda Aydogan[b], Sarah Mburu[a], Sreeramamurthy Ankem[a]

[a] Department of Materials Science and Engineering, University of Maryland, College Park, MD 20742, USA
[b] MST-8, Materials Science Division, Los Alamos National Laboratory, Los Alamos, NM 87545, USA

ARTICLE INFO

Keywords:
Steel
Micromechanics
EBSD
Nanoindentation
Finite element method

ABSTRACT

The phase properties and deformation behavior of the δ–ferrite and γ–austenite phases of CF–3 and CF–8 cast duplex stainless steels were characterized by nanoindentation and microstructure-based finite element method (FEM) models. The elastic modulus of each phase was evaluated and the results indicate that the mean elastic modulus of the δ–ferrite phase is greater than that of the γ–austenite phase, and the mean nanoindentation hardness values of each phase are approximately the same. The elastic FEM model results illustrate that greater von Mises stresses are located within the δ–ferrite phase, while greater von Mises strains are located in the γ–austenite phase in response to elastic deformation. The elastic moduli calculated by FEM agree closely with those measured by tensile testing. The plastically deformed specimens exhibit an increase in misorientation, deformed grains, and subgrain structure formation as measured by electron backscatter diffraction (EBSD).

1. Introduction

Cast duplex stainless steels (CDSS), such as CF–3 and CF–8, are commonly used as structural materials in cooling water pipes, valve bodies, pump casings, and elbows of commercial light water nuclear reactors. These systems operate at service temperatures between 280 °C (553 K) and 320 °C (593 K), and it is well known that thermal embrittlement occurs due to phase decomposition of the body-centered cubic (b.c.c.) δ–ferrite phase under these conditions [1–3]. In an effort to evaluate the possibility of extending the service life of these reactors up to 80 years and predict the evolution of the mechanical response of CF–3 and CF–8 CDSS, it is necessary to analyze the deformation behavior and mechanical response in these materials. Studies have been conducted to determine the bulk mechanical properties of CDSS in order to verify their reliability as long-term components. The microhardness, impact toughness, and ultimate tensile strength (UTS) have been evaluated, and the results show that some effects of phase decomposition can be measured by changes in these properties [4–9]. However, decomposition occurs in the ferrite phase, which often constitutes less than 20 vol% of the microstructure [7–9]. Despite the aforementioned studies and the interest in thermal aging embrittlement of CF–3 and CF–8 steels, the differences in mechanical properties of the constituent phases are not well known. Further, stress and strain distributions and partitioning in these steels related to the different properties of the constituent phases have not been investigated.

Finite element method (FEM) modeling based on microstructures observed by optical microscopy or scanning electron microscopy is an increasingly relevant approach to gain insight into deformation behavior, stress and strain distributions, and failure initiation in dual-phase steels and stainless steels [10–14]. Duplex steels can be modeled following a composite material model of mechanical behavior, where the bulk mechanical behavior of the steel is dependent on the morphology and distribution of the phases and their corresponding elastic moduli, E, Poisson's ratios, ν, and volume fractions, f, [15–17]. In general, the literature contains limited results on the constituent phase properties of some duplex stainless steels [18,19], but there are no reported results for the phase properties of the CF–3 and CF–8 steels. With these properties evaluated, it is possible to analyze the micromechanical behavior of the duplex steels by FEM, which can help elucidate structure-property relationships in these steels, as demonstrated recently on TRIP and DP 590 steels [12,20].

Instrumented nanoindentation provides an established technique to measure the elastic properties of metals and alloys by permitting selection of a single-phase grain. The relationship between indentation and elastic properties was initially discussed by Tabor [21]. Oliver and Pharr [22] presented a method (henceforth referred to as the Oliver

* Correspondence to: Department of Materials Science and Engineering, University of Maryland, 2144 Chemical and Nuclear Engineering Building, #090, College Park, MD 20742-2115, USA.
E-mail address: sschwarm@umd.edu (S.C. Schwarm).

http://dx.doi.org/10.1016/j.msea.2016.10.116
Received 13 May 2016; Received in revised form 17 October 2016; Accepted 31 October 2016
Available online 03 November 2016
0921-5093/

and Pharr method) to determine the elastic modulus and hardness of a single-phase grain from the load-displacement curve of a sharp nanoindentation test that has been implemented in ASTM Standard E2546-07 [23]. More recently, nanoindentation has been employed to measure plastic properties, such as the strain-hardening exponent, n, and yield strength, σ_y, of metals and alloys that obey power-law strain-hardening behavior. Dao et al. formulated a reverse analysis method (henceforth referred to as the Dao method) combining a dimensionless analytical approach with experimental nanoindentation data and tested its validity on 6061-T6511 and 7075-T651 aluminum (Al) alloys [24]. Ogasawara et al. applied a modified approach to the Dao method (henceforth referred to as the Ogasawara method) in order to obtain the strain-hardening exponent and yield strength of a wider range of alloys that obey power-law strain-hardening behavior, including brass, gold (Au), copper (Cu), and Al specimens [25]. The extant literature indicates that both the Oliver and Pharr and Dao methods provide reasonably accurate results for the elastic properties of many metals and alloys, including some dual-phase steels and stainless steels [17,19,24,26]. The applicability of using instrumented nanoindentation to determine plastic properties of duplex stainless steels has not, however, been resolved.

This investigation characterizes the properties of the ferrite and austenite phases in the CF–3 and CF–8 CDSS by instrumented nanoindentation and then uses these properties to develop a microstructure-based FEM model. We compare the differences between the Oliver and Pharr and Dao analysis methods to determine the elastic properties by nanoindentation. The limitations of the Dao and Ogasawara methods in determining the plastic properties of these dual-phase steels are discussed. The FEM model is used to analyze the elastic deformation of the constituent phases. We discuss the distribution of stresses and strains in the CDSS microstructures determined by elastic FEM, including evaluating partitioning of the stresses and strains between the two phases and comparing the effects of microstructure morphology and constituent phase properties of the steels. The bulk elastic modulus calculated by FEM is compared with that measured by tensile testing. The misorientation distribution resulting from tensile plastic deformation is measured by electron backscatter diffraction (EBSD) using kernel average misorientation (KAM) and grain orientation spread (GOS) analysis.

2. Experimental procedures

2.1. Materials and metallographic preparation

The steels investigated in this study were obtained from Monett Company, Inc. as 17.8 cm × 3.3 cm × 2.9 cm rectangular keel blocks that were cast to the CF–3 and CF–8 standard specification outlined in ASTM A351-14 [30]. All blocks of each steel type were statically cast from the same melt followed by a solution treatment at 1065 °C (1338 K) for two hours and quenched in water at room temperature in accordance with the ASTM standard. The nominal chemical composition of the two steels as measured by optical emission spectroscopy (OES) is provided in Table 1. Specimens were mechanically cut into blanks for machining and the blanks were further reduced to approximately 10 mm × 10 mm × 3 mm specimens and cold mounted in epoxy for metallography. The specimens were ground and polished to 0.3 μm surface finish and etched with Kalling's reagent No. 1 at room temperature following standard procedures to reveal the dual-phase microstructure.

2.2. Optical microscopy and volume percentage (fraction) calculations

Optical microscopy was performed employing a Buehler® ViewMet Inverted Metallograph. The volume percentage (fraction) of the b.c.c. δ–ferrite and face-centered cubic (f.c.c.) γ–austenite phases in the microstructure were determined employing three different methodologies: (1) manual point counting in accordance with the ASTM E562-11 standard, (2) digital counting of pixels using the Image–J version 1.50b software in accordance with the ASTM E1245-03 standard, and (3) the Schoefer diagram based on composition in accordance with the ASTM A800-14 standard [27–29]. The percentages determined by methods (1) and (2) were measured by utilizing 20 optical micrographs from each steel as specified in the standards.

2.3. Tensile testing

Cylindrical test specimens with a diameter of 6.35 mm (0.25 in.) and a gauge length of 25.4 mm (1.0 in.) were fabricated in accordance with the ASTM E8-13a standard [30]. Tensile tests were performed employing an Instron® 8502 test frame equipped with an 8800 controller in accordance with the ASTM standard procedures. A preload of ~100 N was applied before the start of each test and a calibrated extensometer with 50% elongation capability was used for continuous measurement of strain using strain-rate control rate of 0.00025 s^{-1}. The extensometer was removed at its elongation limit and the tensile specimens were tested to failure using crosshead speed control rate of 0.006125 mm s^{-1}. Determination of the bulk plastic tensile properties was carried out following the procedures outlined in the ASTM E8-13a Standard [30].

2.4. Electron backscatter diffraction (EBSD)

The misorientation distribution resulting from tensile plastic deformation of the γ–austenite and δ–ferrite phases were investigated by the EBSD technique using a FEI Inspect Field Emission Gun (FEG) scanning electron microscope (SEM) instrument equipped with TSL EBSD detector. Specimens taken from the transverse section of the tensile specimen gauge lengths were prepared by standard metallographic techniques followed by jet electropolishing using a solution of 5 vol% perchloric acid in methanol at approximately −30 °C with an applied voltage of 23 V. Experiments were performed on a 70° pre-tilted holder at an accelerating voltage of 20 kV and aperture size of 50 μm. The EBSD scans were performed at two different magnifications. The scanned area was either ~0.25 μm × ~0.5 μm or ~0.75 μm × ~1.5 μm and the step size for data collection was 0.4 μm and 1.2 μm, respectively. Data analyses were performed using TSL OIM software. Kernal average misorientation (KAM) studies were conducted using an exclusion angle of 5° and considering the second nearest neighbors. Grain orientation spread (GOS) analyses were

Table 1
Nominal composition (wt%) of the CF–3 and CF–8 cast duplex stainless steels (CDSS).

		Composition (wt%)						
Steel		**Fe**	**Cr**	**Ni**	**Si_{max}**	**Mn_{max}**	**Mo_{max}**	**C_{max}**
CF–3	**ASTM A351**	Balance	17.0–21.0	8.0–12.0	2.00	1.50	0.50	0.03
	Unaged	69.52	19.69	8.40	0.98	1.07	0.28	0.02
CF–8	**ASTM A351**	Balance	18.0–21.0	8.0–11.0	2.00	1.50	0.50	0.08
	Unaged	69.44	19.85	8.30	0.97	0.99	0.35	0.06

performed using a 5° tolerance angle.

2.5. Nanoindentation

Load-controlled nanoindentation testing was performed employing a calibrated Hysitron 900 Triboindenter with a diamond Berkovich tip to 4000 μN maximum load. The 40 s total indentation time was divided into three segments consisting of 15 s loading time, 10 s holding time, and 15 s unloading time. Testing was performed by creating three 2 × 2 grids of indents spaced 2 μm apart in each phase. Three CF–3 and three CF–8 specimens were indented for a total of 36 indents in both the δ–ferrite and the γ–austenite phases for both steels.

2.6. Finite element method model

A two-dimensional (2-D) FEM model of the unaged CF–3 and CF–8 microstructures was developed in the ANSYS® Mechanical APDL version 16.2 software. The optical micrographs of the dual-phase microstructures were converted to vector format using RasterVect version 21.5 software. The vectorized microstructure images were meshed in the ANSYS® software using a triangular Solid, Plane 183 element. There are six nodes per element and the elemental edge dimension is 0.075 units (equivalent to ~3.2 μm). The elastic material model properties of the ferrite and austenite phases utilized in the FEM model were obtained by instrumented nanoindentation, as discussed below. A uniform tensile displacement was applied in the y–direction along the top row of nodes. The bottom row of nodes was constrained in the y–direction and the center bottom node was constrained in the x–direction in order to simulate a strain-rate controlled tensile test [15,31]. The displacement was applied to the equivalent of 0.1% strain, which is within the elastic deformation region. The deformation conditions were validated with models consisting of a single-phase δ–ferrite crystal, a single-phase γ–austenite crystal, and a rectangular bi-crystal model with one δ–ferrite/γ–austenite heterophase interface and found to produce no extraneous stresses or artifacts in either the x– or y–directions. The mesh size dependency at the defined element size of 0.075 units was evaluated and found to be negligible.

3. Results and discussion

3.1. Microstructural characterization

An optical micrograph of the CF–3 steel, Fig. 1, illustrates an example microstructure consisting of a network of island-shaped δ–ferrite phase (dark color) in the continuous γ–austenite matrix phase (light color). The microstructure of the CF–8 steel has a qualitatively similar appearance to that of the CF–3 steel. This microstructure is consistent with those reported in the literature of a steel with a composition similar to CF–8, with a ferrite content of less than 20% by volume [9,32].

Fig. 1. An optical micrograph of an example CF–3 cast duplex stainless steel (CDSS) microstructure illustrating the face-centered cubic (f.c.c.) γ–austenite (light) matrix phase and a network of body-centered cubic (b.c.c.) δ–ferrite (dark) phase islands.

Table 2
Ferrite volume percentage in the unaged CF–3 and CF–8 cast duplex stainless steels (CDSS) as determined by three different methods.

Steel	Ferrite volume percentage (%)		
	Manual point counting [ASTM E562-11]	Digital counting of pixels [ASTM E1245-03]	Schoefer diagram [ASTM A800-14]
CF–3	11.5 ± 1.1	12.1 ± 1.0	18 ± 6.3
CF–8	9.1 ± 0.9	10.0 ± 0.4	14 ± 4.8

The b.c.c. δ–ferrite phase volume percentage of the CF–3 steel is greater than the CF–8 steel when measured by the three aforementioned methods, Table 2. By the manual point counting method, the CF–3 steel ferrite volume percentage is 11.5 ± 1.1 vol% while that of the CF–8 steel is 9.1 ± 0.9 vol%. The digital counting method results in a ferrite volume percentage of 12.1 ± 1.0 vol% for the CF–3 steel and 10.0 ± 0.4 vol% for the CF–8 steel. The Schoefer method based on the CF–3 and CF–8 nominal compositions predicts ferrite volume percentages of 18 ± 6.3 vol% and 14 ± 4.8 vol%, respectively. The Schoefer diagram is based on Cr equivalency and Ni equivalency values, where the magnitude of each element's contribution to the b.c.c.-forming chromium equivalency term, Cr_{eq}, and f.c.c.-forming nickel equivalency term, Ni_{eq}, affect the formation of either the δ–ferrite or the γ–austenite phase, respectively [33]. The CF–3 steel has a Cr_{eq}/Ni_{eq} ratio of 1.34, whereas the CF–8 steel has a ratio of 1.25, resulting in a larger expected ferrite volume percentage in the former. Since the Schoefer diagram is not specific to the CDSS used in this study and is based on generalized composition and element equivalency data of many duplex stainless steels, the values measured by the manual point counting method and the digital counting of pixels method are likely more accurate. The directly measured values are, however, within the range determined by the Schoefer diagram for both steels.

3.2. Tensile properties and misorientation distribution mapping

Engineering stress-strain curves for the CF–3 and CF–8 stainless steels are presented in Fig. 2. The bulk elastic modulus of the CF–3 steel is approximately 189.1 GPa, whereas it is approximately

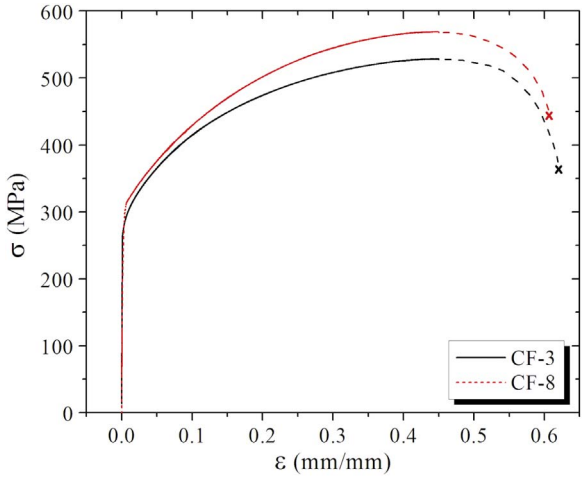

Fig. 2. Engineering stress-strain curves for the CF–3 and CF–8 steels. Both steels reach their ultimate tensile strength (UTS) at approximately 45% elongation. Dashed lines approximate remaining curves to the fracture stress after reaching the elongation limit of the extensometer.

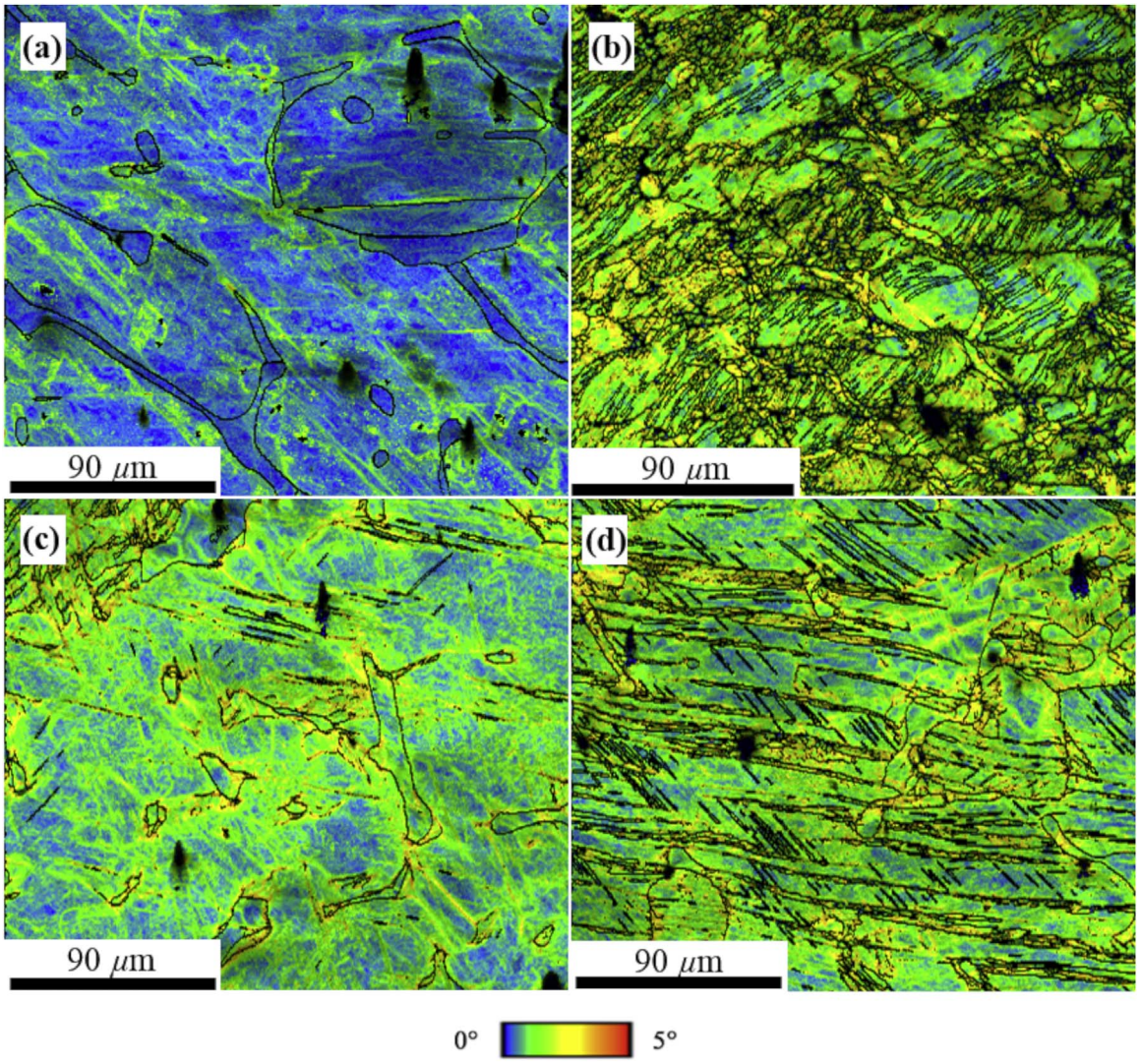

Fig. 3. Kernal average misorientation (KAM) maps superimposed on interface boundary maps having a misorientation angle θ > 5° for CF–3 (a) in undeformed and (b) 45% strained (deformed) specimens; and for CF–8 (c) in undeformed and (d) 45% strained (deformed) specimens. The degree of misorientation is indicated by the color scale. (For interpretation of the references to color in this figure legend, the reader is referred to the web version of this article.)

169.6 GPa in the CF–8 steel. The CF–3 stainless steel exhibits a yield strength of 280 MPa and an ultimate tensile strength (UTS) of 530 MPa. The corresponding values in the CF–8 steel are greater at 286 MPa and 570 MPa, respectively. The CF–3 and CF–8 steels exhibit approximately the same ductility of 60% and 61% total elongation, respectively. While the yield strength and ductility of the two steels are similar, the greater bulk tensile strength of the CF–8 steel can be attributed to the greater C concentration in CF–8 and the presence of $M_{23}C_6$ carbides at the heterophase interfaces [33].

The KAM maps of undeformed and 45% strained CF–3 specimens, Fig. 3(a) and (b), and CF–8 specimens, Fig. 3(c) and (d), respectively, illustrate the misorientation distribution within the microstructures. The undeformed CF–8 exhibits greater misorientation than the undeformed CF–3 steel. One likely contributor to the measured difference between the undeformed steels is the greater nominal concentration of C in the CF–8 and the presence of the aforementioned $M_{23}C_6$-type carbides at the heterophase interfaces. Additionally, both CF–3 and CF–8 exhibit greater misorientation at the δ–ferrite/γ–austenite interfaces than in the interior of the grains in the undeformed condition, which indicates a higher dislocation density at these locations [34].

The KAM maps after plastic deformation, Fig. 3(b) and (d), illustrate that the amount of misorientation has increased in both steels. Furthermore, plastic deformation leads to deformation of the grains, an increase in the quantity of high-angle boundaries, and formation of subgrain structure throughout the microstructure of both steels. As seen from the GOS maps of the 45% deformed tensile specimens, Fig. 4(a) and (b), there is no clear trend regarding the location of high or low misorientation based on the grain or phase structure. Thus, GOS analysis illustrates that the greatest local misorientation can be located in either the ferrite phase or the austenite phase. This suggests that the extent of plastic deformation is similar in both phases.

3.3. Ferrite and austenite elastic properties evaluated by nanoindentation

An example load-displacement curve for the f.c.c. γ–austenite phase in the CF–3 steel, Fig. 5, illustrates the response of the phase during loading, holding, and unloading. The response of the b.c.c. δ–ferrite phase in the CF–3 steel and the same phases in the CF–8 steel have a qualitatively similar appearance but exhibit quantitative differences. The initial linear part of the unloading curve is assumed to be demonstrative of entirely elastic behavior as it measures linear recovery during removal of the Berkovich tip [24]. The stiffness, S, which is used to determine the elastic modulus, E, of each phase in both steels was

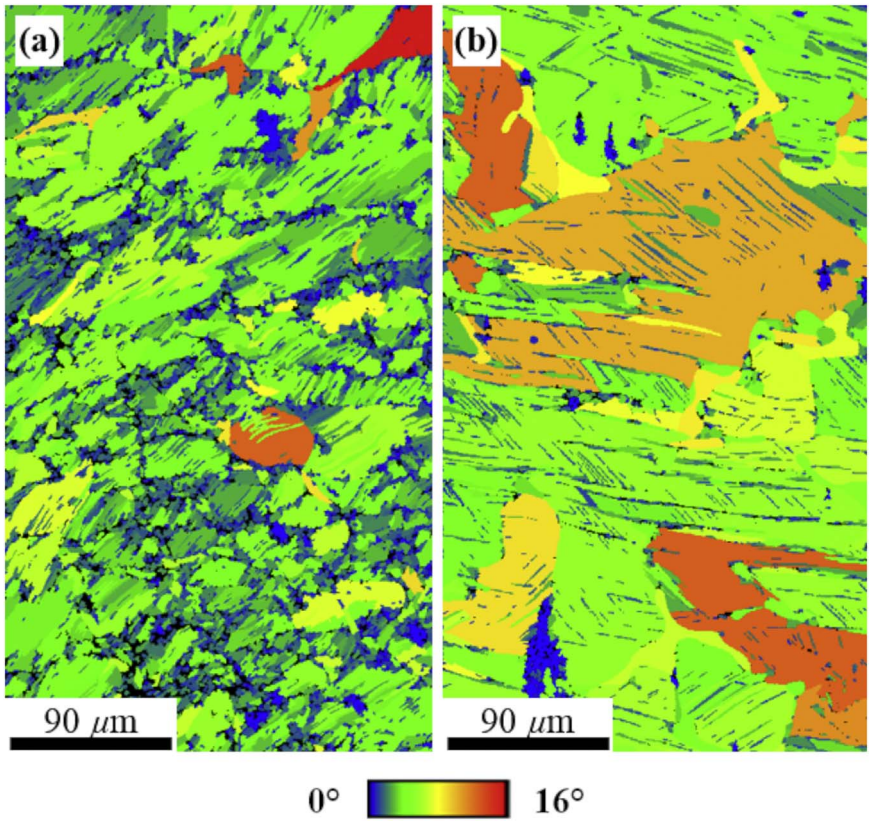

Fig. 4. Grain orientation spread (GOS) maps for 45% strained (deformed) (a) CF–3 and (b) CF–8 specimens. The degree of misorientation with respect to each grain is indicated by the color scale. (For interpretation of the references to color in this figure legend, the reader is referred to the web version of this article.)

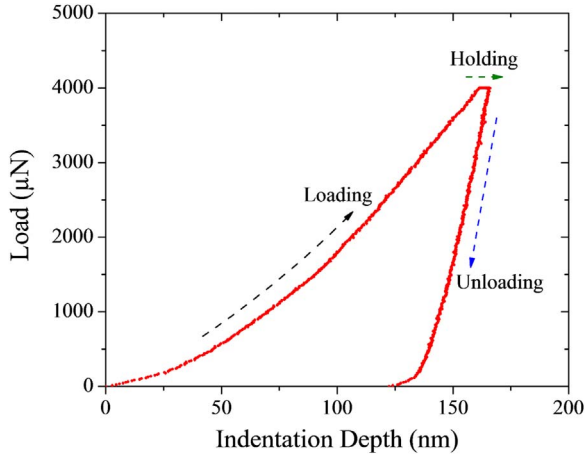

Fig. 5. An example load-displacement curve for the f.c.c. γ–austenite phase in a CF–3 stainless steel specimen exhibiting 15 s loading segment, 10 s holding segment, and 15 s unloading segment when tested by instrumented nanoindentation.

calculated as the slope of the unloading segment of the curve starting from the maximum indentation load, P_{max}, and fitting the first 67% of the curve (i.e. $1.00 \times P_{max}$ to $0.33 \times P_{max}$) by a linear least squares method [35]. The quantity E^* is a function of the elastic modulus and Poisson's ratio of the indenter tip, E_i and ν_i, and the modulus and Poisson's ratio of each phase, E and ν, by the relationship: $E^* = \left[\frac{1-\nu^2}{E} + \frac{1-\nu_i^2}{E_i}\right]^{-1}$, where ν is assumed to be 0.29 for both phases in these CDSS [36]. The quantity E^* is related to the indentation load-displacement curve by a projected area of elastic contact, A, and the quantity S. Although the mean stiffness value of each phase is the same in both the Oliver and Pharr and Dao methods, the quantity A is obtained by different calculations leading to slightly different values of A, shown in Table 3. An estimate of the quantity A is determined directly from the geometry of the Berkovich indenter and the maximum depth, h_{max}, in the Oliver and Pharr method [22], whereas it is determined by simultaneously solving a system of two equations for the quantities A and E^* in the Dao method [24].

Table 3
Mean values of the elastic parameters in the ferrite and austenite phases of the CF–3 and CF–8 CDSS derived from the individual load-displacement curves and the estimated area of contact determined by the Oliver and Pharr (O & P) and Dao methods.

Material		Measured			Calculated	
Stainless steel	Phase	h_{max} (nm)	P_{max} (μN)	S (μN/nm)	$A^{O\&P}$ ($nm^2 \cdot 10^{-5}$)	A^{Dao} ($nm^2 \cdot 10^{-5}$)
CF–3	Ferrite	173.9	3995.5	169.4	7.84	8.14
	Austenite	176.0	3995.5	166.0	8.02	8.50
CF–8	Ferrite	176.6	3994.3	171.1	8.11	8.50
	Austenite	176.0	3994.5	162.5	7.96	9.22

The value of the quantity E for each phase in both the CF–3 and CF–8 CDSS is solved by the above equation and presented in Fig. 6(a) and (b). The Dao method mean elastic modulus agrees to within 12% of the Oliver and Pharr method mean elastic modulus for the γ–austenite phase in both the CF–3 and CF–8 steels, and to within 5% for the δ–ferrite phase. Additionally, the Dao method mean elastic modulus is consistently lower in value than the Oliver and Pharr method by approximately between 8 and 20 GPa, Fig. 6(a) and (b), due to the different estimates of the projected area of contact. In general, the elastic moduli determined by the two methods are in good agreement and the mean elastic modulus of the ferrite phase is greater than that of the austenite phase by approximately 10 GPa in both the CF–3 and CF–8 stainless steels. The elastic modulus values obtained are slightly less than those reported in a study by Gadelrab et al. of a Uranus 50

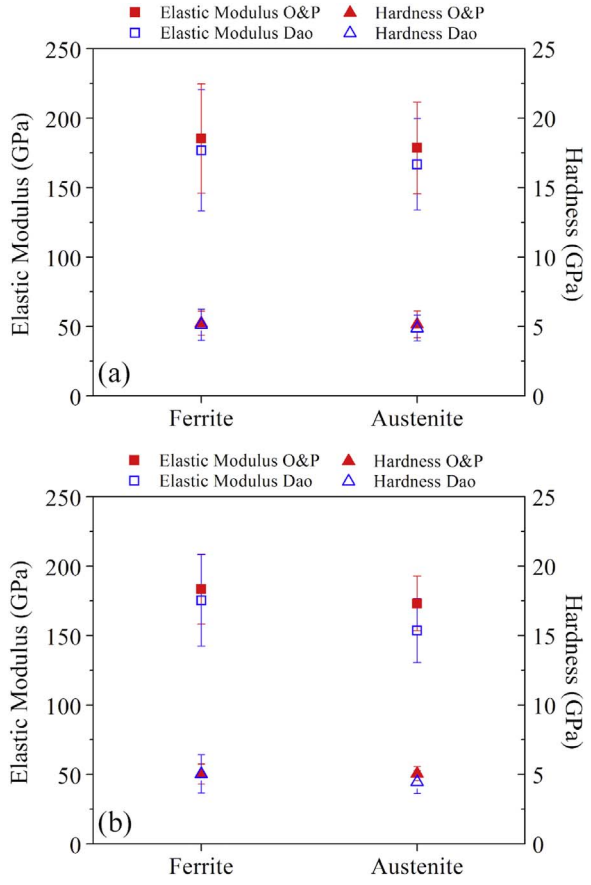

Fig. 6. Comparison of calculated mean elastic modulus, E, and nanoindentation hardness, H, for the b.c.c. δ–ferrite and f.c.c. γ–austenite phases between the Oliver and Pharr and Dao methods for the (a) CF–3 and (b) CF–8 stainless steels. The mean values of both quantities are slightly greater in the ferrite phase of both steels.

duplex stainless steel, when employing the Oliver and Pharr method [19]. Guo et al. reported greater values for the elastic moduli of the constituent phases in a Z3CN20-09M duplex stainless steel, although their methodology was not specified [18]. In each study, the ferrite phase is reported to possess a greater elastic modulus than the austenite phase.

The Oliver and Pharr and Dao methods are also utilized to determine the nanoindentation hardness, H, of the two phases in both the CF–3 and CF–8 CDSS. In both methods, the nanoindentation hardness is calculated directly from the quantity P_{max} and the quantities $A^{O\&P}$ and A^{Dao}, Table 3. The calculated mean nanoindentation hardness values of each phase in both stainless steels are slightly greater than 5 GPa when using the Oliver and Pharr method. The Dao method calculations show that the mean nanoindentation hardness values of the b.c.c. δ–ferrite phase for both steels agree closely with those from the Oliver and Pharr method. The mean nanoindentation hardness values of the f.c.c. γ–austenite phase are, however, approximately between 5% and 10% lower than those from the Oliver and Pharr method, Fig. 6(a) and (b). The ferrite phase mean nanoindentation hardness is slightly harder than that of the austenite phase. Furthermore, the Dao method shows a greater difference in the quantity H between the two phases of the steels when compared to the Oliver and Pharr method. This could be demonstrative of a real physical difference in nanoindentation hardness between phases, indicating that the Dao method is better suited toward elucidating this difference due to the use of experimentally measured data in developing the dimensionless equations [24]. Alternatively, the difference could be caused by a better fit of the nanoindentation data to the dimensionless equations for the b.c.c. δ–ferrite than the f.c.c. γ–austenite phase. In contradistinction, the Oliver and Pharr method does not rely on calibration to experimentally measured data [22].

3.4. Ferrite and austenite plastic properties evaluated by nanoindentation

The Dao and Ogasawara methods each provide an approach to determining the plastic behavior of each phase – in terms of the representative stress, σ_r, at a specified value of the plastic strain, r, and the quantity n – based on dimensionless equations derived from the parabolic loading portion of the nanoindentation curve, Fig. 5. The quantity σ_y can be determined from the calculation of n and σ_r by utilizing a power-law relationship. However, values of σ_r determined for the ferrite and austenite phases in the CF–3 and CF–8 steels in this investigation were found to be an order of magnitude higher than the experimentally determined bulk yield stress. In a majority of cases, the equations failed to return a value for the quantity n between 0 and 1, and the values that could be determined for the quantity n varied widely. Because the calculation of yield stress is a function of both the representative stress and strain-hardening exponent, the yield stress could not be calculated when the quantity n was indeterminate. The σ_y values that could be calculated were unreasonably high following the trend for the quantity σ_r.

These results suggest that there are limitations in applying these methods to determine the plastic properties of some stainless steels. Guelorget et al. [37] were also unable to return a solution for the quantity σ_y when using the Ogasawara method in a 316L austenitic stainless steel. The limitations could be caused by deviation from the region of applicability of the Dao method ($n \leq 0.3$ or $0.3 < n \leq 0.5$ and $\frac{\sigma_y}{E^*} < 0.03$) and the Ogasawara method ($0 \leq n \leq 0.5$ and $3 \leq \frac{\overline{E}}{\sigma_r} \leq 3300$; where $\overline{E} = \frac{E}{1-\nu^2}$). Solutions outside of these parameter ranges are subject to greater variation and there exists the possibility of a non-unique solution. Furthermore, it is possible that the δ–ferrite and the γ–austenite phases in the CF–3 and CF–8 CDSS do not strictly follow power-law strain-hardening behavior, as is the case for some duplex steels [38,39].

3.5. Elastic deformation analysis by finite element method

We consider here the elastic properties determined by nanoindentation using the Oliver and Pharr method, Fig. 6(a) and (b), where the results indicate that the b.c.c. δ–ferrite phase is elastically stiffer than the f.c.c. γ–austenite phase for both steels. The elastic modulus values were utilized in the material models of the 2-D FEM microstructure-based models of the CF–3, Fig. 7, and CF–8 steels. The Poisson's ratio is assumed to be 0.29 for both phases and applicability of the von Mises yield criterion is assumed.

The FEM results for the example CF–3 and CF–8 microstructures in Fig. 8(a)–(d) illustrate the effects of applied elastic deformation on the δ–ferrite and γ–austenite phases. Contour plots of the von Mises stresses determined by FEM, Fig. 8(a) and (b), demonstrate higher δ–ferrite phase stresses (yellow, orange, and red contours) and the lower γ–austenite phase stresses (blue and green contours). The highest stresses (red contours) occur in the narrowest regions of the ferrite phase. Similarly, the von Mises strains, Fig. 8(c) and (d), exhibit significant heterogeneity in both steels' microstructures. In general, the strains are greater in the γ–austenite phase (green, yellow, orange, and red contours) than in the δ–ferrite phase (blue contours). The maximum stress determined by FEM for this applied deformation condition is 188 MPa for CF–3, Fig. 8(a), whereas it is 187 MPa for CF–8, Fig. 8(b). In both cases, the stresses determined from the FEM model are about 100 MPa less than the bulk yield stress. The maximum von Mises strain is calculated as 0.1028% in the CF–3 steel, Fig. 8(c), and 0.1043% in the CF–8 steel, Fig. 8(d). The bulk elastic modulus calculated from the FEM model by using the stress in the y–direction

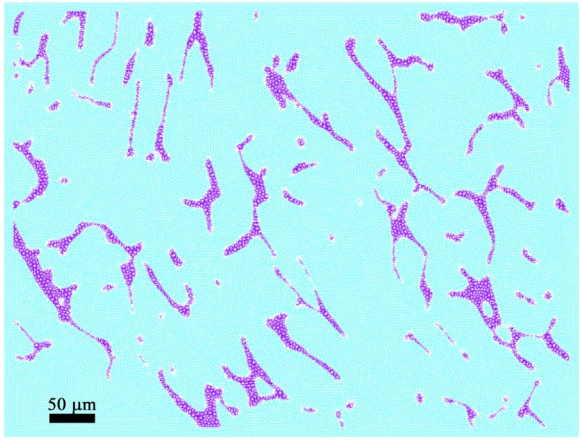

Fig. 7. Microstructure-based finite element method (FEM) model mesh of the CF–3 microstructure in Fig. 1. The cyan regions are areas defined by γ–austenite elastic properties and the purple islands are areas defined by δ–ferrite elastic properties. (For interpretation of the references to color in this figure legend, the reader is referred to the web version of this article.)

and the applied strain are 179.3 GPa and 174.1 GPa for CF–3 and CF–8, respectively, which are within 6% of the experimentally measured bulk values.

Since the von Mises elastic stresses and strains exhibit significant heterogeneity in the microstructure of both steels, the average stresses and strains in each phase were calculated in order to quantify the visual results by determining partitioning ratios of the form $\sigma_\gamma/\sigma_\delta$ and $\varepsilon_\gamma/\varepsilon_\delta$, which permit direct comparison of the ferrite and austenite response. The partitioning ratios of the von Mises stresses ($\sigma_\gamma/\sigma_\delta$) for CF–3 and CF–8 are 0.984 and 0.978, respectively, which indicates that the stresses are higher in the ferrite phase. The partitioning ratios of the von Mises strains ($\varepsilon_\gamma/\varepsilon_\delta$) indicates that the strains are higher in the austenite phase, where the ratios are 1.022 and 1.038 for CF–3 and CF–8, respectively. Furthermore, the stress and strain distributions are influenced by differences in morphology of the microstructures in the steels. The CF–3 exhibits greater stress and strain homogeneity in the matrix phase away from the heterophase interfaces when compared to CF–8. Larger areas of uniform coloration in the relatively unconstrained regions of the austenite matrix phase away from the heterophase interfaces can be observed in Fig. 8(a) and (c) when compared to Fig. 8(b) and (d).

The heterogeneity of the stress and strain distributions can be explained by the difference in elastic modulus of the phases. The δ–ferrite phase will resist elastic deformation more than the γ–austenite phase. Thus, stress is transferred from the γ–austenite matrix to the δ–ferrite islands in order to maintain compatibility at the interfaces. The stresses are highest in ferrite islands that are elongated in a direction parallel to the direction of applied deformation. Choi et al., attributed this phenomenon in TRIP steel to a state of elevated stress triaxiality, where the constraints placed on the microstructure result in higher stresses perpendicular to the applied deformation direction [12]. A larger value of the hydrostatic component of stress is expected in these locations as a result, which suggests that these are regions of interest for void initiation during the onset of ductile failure [40].

In these steels, both phases are considered to be ductile [41] and thus both phases are expected to deform plastically. The regions exhibiting the highest von Mises stresses and strains are the most likely locations for the onset of yielding. Since the yield stress values for the constituent phases could not be determined in the present study by nanoindentation due to limitations of the extant models, the plastic stress and strain distributions were not investigated by FEM in this study. Analysis of the misorientation distributions related to the plastic strain after deformation of the CF–3 and CF–8 steels suggests that the strengths of the constituent phases are similar. Since the elastic

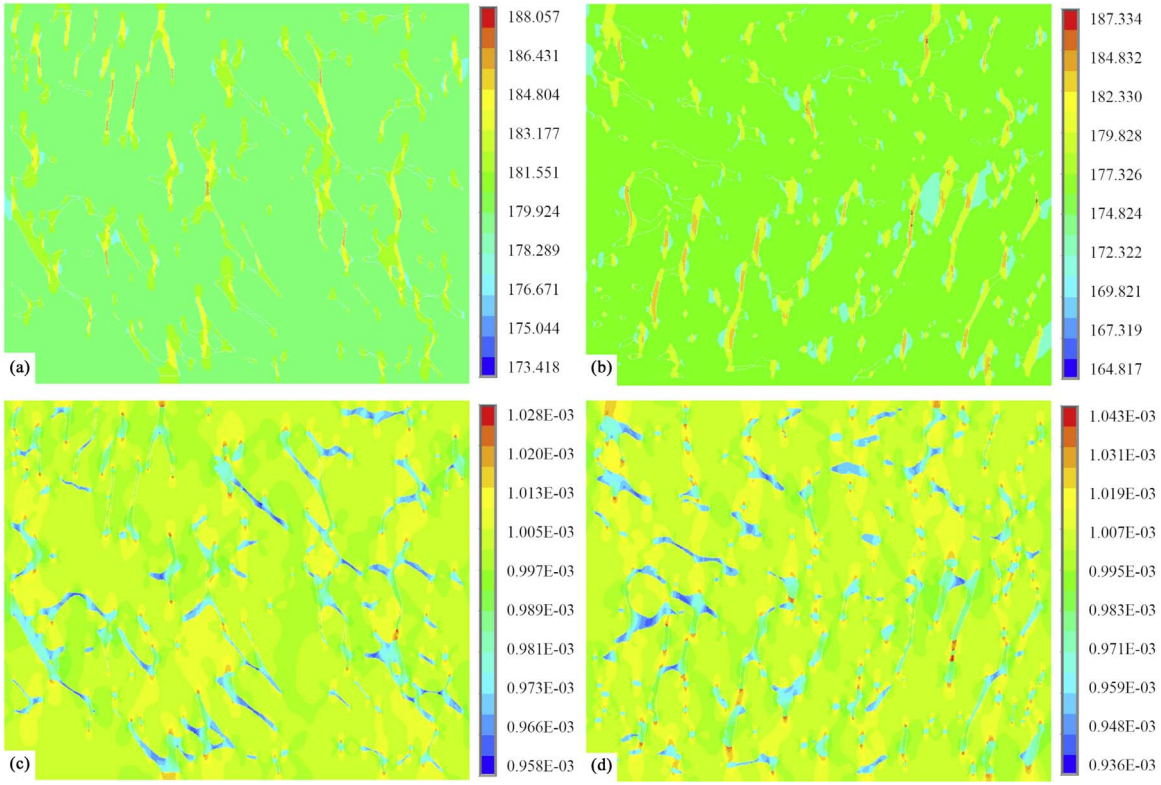

Fig. 8. Contour plots of the FEM results for (a) von Mises elastic stresses in CF–3, (b) von Mises elastic stresses in CF–8, (c) von Mises elastic strains in CF–3, and (d) von Mises elastic strains in CF–8. Higher stresses and strains are represented by warm coloration (red, orange, yellow) and lower stresses and strains are represented by cool coloration (green, blue, indigo). Legends are in units of MPa for stress maps and μm/μm for strain maps. (For interpretation of the references to color in this figure legend, the reader is referred to the web version of this article.)

deformation stresses are found to be higher in the δ–ferrite phase than in the γ–austenite phase, and assuming equal values for the yield stress, the ferrite phase would plastically deform prior to the austenite phase. However, the actual location for the onset of yielding will depend on the exact magnitude of the yield stresses relative to the stress and strain distributions in the microstructure.

4. Conclusions

The elastic modulus and nanoindentation hardness have been determined by instrumented nanoindentation for the b.c.c. δ–ferrite and f.c.c. γ–austenite phases in CF–3 and CF–8 CDSS. The elastic moduli were utilized in a microstructure-based FEM model of example CDSS microstructures, which reveal the stress and strain distributions and partitioning during elastic deformation. The misorientation distribution after plastic deformation of the tensile specimens was evaluated by EBSD. The following conclusions have been made from this investigation:

(1) The ferrite volume percentages in the CF–3 and CF–8 CDSS were calculated by the manual point counting method, as 11.5 ± 1.1 vol% and 9.1 ± 0.9 vol%, respectively. These values are consistent with those determined via digital pixel counting method, which determine the ferrite volume percentages as 12.1 ± 1.0 vol% and 10.0 ± 0.4 vol% for CF–3 and CF–8, respectively.
(2) The CF–3 steel is has a bulk yield strength of 280 MPa and a tensile strength of 530 MPa. The CF–8 has higher yield and tensile strengths, which were measured as 286 MPa and 570 MPa, respectively. Electron backscatter diffraction (EBSD) mapping of the deformed tensile specimens reveals that plastic deformation leads to deformation of the grains and formation of subgrain structure. The CF–8 is shown to possess greater misorientation than CF–3 in the undeformed condition and both steels have their greatest misorientation at the grain boundaries and δ–ferrite/γ–austenite heterophase interfaces. Plastic deformation results in increased misorientation in both steels.
(3) Two methods, those formulated by Oliver and Pharr and by Dao et al., were utilized to determine the elastic modulus and nanoindentation hardness of δ–ferrite and γ–austenite in CF–3 and CF–8. The measured values for the elastic modulus, E, by the Oliver and Pharr method are E^{δ}_{CF-3}=185.3 ± 39.6 GPa, E^{γ}_{CF-3}=178.6 ± 33.0 GPa, E^{δ}_{CF-8}=183.4 ± 25.2 GPa, and E^{γ}_{CF-8}=173.1 ± 19.6 GPa. The Dao method results for elastic modulus are E^{δ}_{CF-3}=176.6 ± 43.5 GPa, E^{γ}_{CF-3}=166.7 ± 32.9 GPa, E^{δ}_{CF-8}=175.3 ± 33.0 GPa, and E^{γ}_{CF-8}=153.6 ± 22.9 GPa.
(4) Calculation of the elastic modulus by FEM results in E=179.3 GPa and E=174.1 GPa for CF–3 and CF–8, respectively, which agree to within 6% of the values measured by bulk tensile testing.
(5) The FEM results illustrate that the b.c.c. δ–ferrite phase exhibits greater elastic stresses than the f.c.c. γ–austenite phase, while the austenite phase exhibits greater elastic strains. The corresponding partitioning ratios based on the average stresses and strains in each phase were calculated as $\frac{\sigma_\gamma}{\sigma_\delta}$=0.984and $\frac{\varepsilon_\gamma}{\varepsilon_\delta}$=1.022 for CF–3 and $\frac{\sigma_\gamma}{\sigma_\delta}$=0.978 and $\frac{\varepsilon_\gamma}{\varepsilon_\delta}$=1.038 for CF–8.

Acknowledgements

This work is funded by the U.S. Department of Energy Nuclear Energy University Program (DOE-NEUP); technical monitor Dr. Jeremy T. Busby, Oak Ridge National Laboratory; contract number DOE-NE0000724. Mr. Schwarm would like to acknowledge the Department of Energy: Office of Nuclear Energy (DOE-NE) Integrated University Program (IUP) fellowship program for support. Ms. Sarah Mburu is partially supported by the National Science Foundation (NSF) Louis Stokes Alliances for Minority Participation (LSAMP) under Grant No. 0833018. The authors would like to thank Dr. Daniel E. Perea at Pacific Northwest National Laboratory (PNNL) and Dr. Stuart A. Maloy at Los Alamos National Laboratory (LANL) for assistance and discussions. We would also like to thank Dr. Robert Bonenberger and Dr. Aldo Ponce of the Modern Engineering Materials Instructional Laboratory (MEMIL) at the University of Maryland for access and assistance with the nanoindenter instrument and sample preparation equipment.

References

[1] H.M. Chung, O.K. Chopra, Microstructures of cast-duplex stainless steel after long-term aging, in: Proceedings of the Second International Symposium on Environmental Degradation of Materials in Nuclear Power Systems – Water Reactors, Monterey, CA, 1985, pp. 287–292
[2] K.H. Lo, C.H. Shek, J.K.L. Lai, Recent developments in stainless steels, Mater. Sci. Eng. R 65 (2009) 39–104.
[3] T.S. Byun, Y. Yang, N.R. Overman, J.T. Busby, Thermal aging phenomena in cast duplex stainless steels, JOM 68 (2) (2016) 507–516.
[4] O.K. Chopra, W.J. Shack, Mechanical properties of thermally aged cast stainless steels from shippingport reactor components, U.S. Nuclear Regulatory Commission, Argonne National Laboratory, NUREG/CR-6275, 1995
[5] P.H. Pumphrey, K.N. Akhurst, Aging kinetics of CF3 cast stainless steel in temperature range 300–400 °C, Mater. Sci. Technol. 6 (1990) 211–219.
[6] S. Bonnet, J. Bourgoin, J. Champredonde, D. Guttmann, M. Guttmann, Relationship between evolution of mechanical properties of various cast duplex stainless steels and metallurgical and aging parameters: outline of current EDF programmes, Mater. Sci. Technol. 6 (1990) 221–229.
[7] H.M. Chung, Aging and life prediction of cast duplex stainless steel components, Int. J. Press. Vessel. Pip. 50 (1992) 179–213.
[8] O.K. Chopra, A. Sather, Initial assessment of the mechanisms and significance of low-temperature embrittlement of cast stainless steels in LWR systems, U.S. Nuclear Regulatory Commission, Argonne National Laboratory, NUREG/CR-5385, ANL-89/17, 1990
[9] S.L. Li, et al., Microstructure evolution and impact fracture behaviors of Z3CN20-09M stainless steels after long-term thermal aging, J. Nucl. Mater. 433 (1–3) (2013) 41–49.
[10] X. Sun, K.S. Choi, A. Soulami, W.N. Liu, M.A. Khaleel, On key factors influencing ductile fractures of dual phase (DP) steels, Mater. Sci. Eng. A 526 (1–2) (2009) 140–149.
[11] X. Sun, K.S. Choi, W.N. Liu, M.A. Khaleel, Predicting failure modes and ductility of dual phase steels using plastic strain localization, Int. J. Plast. 25 (10) (2009) 1888–1909.
[12] K.S. Choi, W.N. Liu, X. Sun, M.A. Khaleel, Microstructure-based constitutive modeling of TRIP steel: prediction of ductility and failure modes under different loading conditions, Acta Mater. 57 (8) (2009) 2592–2604.
[13] C.U. Jeong, Y.-U. Heo, J.Y. Choi, W. Woo, S.-H. Choi, A study on the micro-mechanical behaviors of duplex stainless steel under uniaxial tension using ex-situ experimentation and the crystal plasticity finite element method, Int. J. Plast. 75 (2015) 22–38.
[14] S.K. Paul, Micromechanics based modeling of dual phase steels: prediction of ductility and failure modes, Comput. Mater. Sci. 56 (2012) 34–42.
[15] S. Ankem, H. Margolin, C.A. Greene, B.W. Neuberger, P.G. Oberson, Mechanical properties of alloys consisting of two ductile phases, Prog. Mater. Sci. 51 (2006) 632–709.
[16] K.S. Choi, A. Soulami, W.N. Liu, X. Sun, M.A. Khaleel, Influence of various material design parameters on deformation behaviors of TRIP steels, Comput. Mater. Sci. 50 (2) (2010) 720–730.
[17] E.-Y. Guo, S.S. Singh, H. Xie, J.J. Williams, T. Jing, N. Chawla, Microstructure-based modeling of deformation in steels based on constitutive relationships from micropillar compression, Steel Res. Int. 85 (6) (2014) 946–953.
[18] E.-Y. Guo, H.-X. Xie, S.S. Singh, A. Kirubanandham, T. Jing, N. Chawla, Mechanical characterization of microconstituents in a cast duples stainless steel by micropillar compression, Mater. Sci. Eng. A 598 (2014) 98–105.
[19] K.R. Gadelrab, G. Li, M. Chiesa, T. Souier, Local characterization of austenite and ferrite phases in duplex stainless steel using MFM and nanoindentation, J. Mater. Res. 27 (12) (2012) 1573–1579.
[20] S.K. Paul, Real microstructure based micromechanical model to simulate micro-structural level deformation behavior and failure initiation in DP 590 steel, Mater. Des. 44 (2013) 397–406.
[21] D. Tabor, The physical meaning of indentation and scratch hardness, Br. J. Appl. Phys. 7 (1956) 159–166.
[22] W.C. Oliver, G.M. Pharr, An improved technique for determining hardness and elastic modulus using load and displacement sensing indentation experiments, J. Mater. Res. 7 (6) (1992) 1564–1583.
[23] ASTM Standard E2546-07, Standard Practice for Instrumented Indentation Testing, ASTM International, West Conshohocken, PA, 2007.
[24] M. Dao, N. Chollacoop, K.J. Van Vliet, T.A. Venkatesh, S. Suresh, Computational modeling of the forward and reverse problems in instrumented sharp indentation, Acta Mater. 49 (2001) 3899–3918.
[25] N. Ogasawara, N. Chiba, X. Chen, Measuring the plastic properties of bulk materials by single indentation test, Scr. Mater. 54 (2006) 65–70.

[26] E. Harvey, L. Ladani, M. Weaver, Complete mechanical characterization of nanocrystalline Al-Mg alloy using nanoindentation, Mech. Mater. 52 (2012) 1–11.
[27] ASTM Standard E562-11, Standard Test Method for Determining Volume Fraction by Systematic Manual Point Count, ASTM International, West Conshohocken, PA, 2011.
[28] ASTM Standard E1245-03, Standard Practice for Determining the Inclusion or Second-Phase Constituent Content of Metals by Automatic Image Analysis, ASTM International, West Conshohocken, PA, 2008.
[29] ASTM Standard A800/A800M-14, Standard Practice for Steel Casting, Austenitic Alloy, Estimating Ferrite Content Thereof, ASTM International, West Conshohocken, PA, 2014.
[30] ASTM Standard E8/E8M-13a, Standard Test Methods for Tension Testing of Metallic Materials, ASTM International, West Conshohocken, PA, 2013.
[31] C.A. Greene, S. Ankem, Modelling of elastic interaction stresses in two-phase materials by FEM, Mater. Sci. Eng. A 202 (1–2) (1995) 103–111.
[32] Y.H. Yao, J.F. Wei, Z.P. Wang, Effect of long-term thermal aging on the mechanical properties of casting duplex stainless steels, Mater. Sci. Eng. A 551 (2012) 116–121.
[33] S. Mburu, R.P. Kolli, D.E. Perea, S.C. Schwarm, A. Eaton, J. Liu, S. Patel, J. Bartrand, S. Ankem, Atom probe tomography analysis of the local chemical environment at the austenite/ferrite interfaces of cast duplex stainless steels, in: Proceedings of the 14th LACCEI International Multi-Conference for Engineering, Education, and Technology: Engineering Innovations for Global Sustainability, San Jose, Costa Rica, 2016
[34] M. Calcagnotto, D. Ponge, E. Demir, D. Raabe, Orientation gradients and geometrically necessary dislocations in ultrafine grained dual-phase steels studied by 2D and 3D EBSD, Mater. Sci. Eng. A 527 (10–11) (2010) 2738–2746.
[35] J.H. Lee, T. Kim, H. Lee, A study on robust indentation techniques to evaluate elastic-plastic properties of metals, Int. J. Solids Struct. 47 (2010) 647–664.
[36] H.M. Ledbetter, Stainless steel elastic constants at low temperatures, J. Appl. Phys. 52 (1981) 1587–1589.
[37] B. Guelorget, M. Francois, Extracting the plastic properties of metal materials from microindentation tests: experimental comparison of recently published methods, J. Mater. Res. 22 (6) (2007) 1512–1518.
[38] M.R. Akbarpour, A. Ekrami, Effect of ferrite volume fraction on work hardening behavior of high bainite dual phase (DP) steels, Mater. Sci. Eng. A 477 (1–2) (2008) 306–310.
[39] L.F. Ramos, D.K. Matlock, G. Krauss, On the deformation behavior of dual-phase steels, Metall. Trans. A 10 (2) (1979) 259–261.
[40] G.E. Dieter, Mechanical metallurgy, SI Metric, McGraw-Hill, Singapore, 1988
[41] Y. Tomota, K. Kuroki, T. Mori, I. Tamura, Tensile deformation of two-ductile-phase alloys: flow curves of α-γ Fe-Cr-Ni alloys, Mater. Sci. Eng. 24 (1) (1976) 85–94.